



Friedrich-Schiller-Universität
Jena



Young star V1331 Cygni takes centre stage

Dissertation

*zur Erlangung des akademischen Grades
doctor rerum naturalium (Dr. rer. nat.)*

vorgelegt dem Rat der

Physikalisch-Astronomische Fakultät
Friedrich-Schiller-Universität Jena
Thüringer Landessternwarte Tautenburg

von Dipl.-Phys. Arpita Choudhary

geboren am 02. Oktober 1986

in

Lucknow, India

Gutachter

1.
2.
3.

Tag der Disputation:

Declaration of Authorship

I, Arpita CHOUDHARY, declare that this thesis titled, '**Young star V1331 Cygni takes centre stage**' and the work presented in it are my own. I confirm that:

- This work was done wholly or mainly while in candidature for a research degree at this University.
- Where any part of this thesis has previously been submitted for a degree or any other qualification at this University or any other institution, this has been clearly stated.
- Where I have consulted the published work of others, this is always clearly attributed.
- Where I have quoted from the work of others, the source is always given. With the exception of such quotations, this thesis is entirely my own work.
- I have acknowledged all main sources of help.
- Where the thesis is based on work done by myself jointly with others, I have made clear exactly what was done by others and what I have contributed myself.
- The thesis is written making use of **Linux** operating system and the typesetting software \LaTeX , both open source. The thesis title is inspired from **Hubble picture of the day** title for V1331 Cyg, released on March 2, 2015.

Signed:

Date:

“Astronomy compels the soul to look upwards and leads us from this world to another.”

Plato

Abstract

Young star V1331 Cygni takes centre stage

by Arpita CHOUDHARY

With first epoch observations of HST-WFPC2 already available for V1331 Cyg from year 2000, second epoch data was observed in 2009. I study the time evolution of circumstellar nebula by analysing and comparing the two epochs of HST observations. Radial colour analysis of outer dust arc is done as well to check whether the radial grain size distribution was modified by a previous FUor wind. HST images are cleaned using IRAF and PSF subtraction is done using model PSF generated from Tiny Tim software. IDL scripts and routines are used to do proper motion analysis. The outer dust arc is found to be expanding at $\approx 14.8 \pm 3.6$ km s⁻¹ on average. The expansion velocity of inner ring is less consistent, between 0.8 km s⁻¹ and 3.4 km s⁻¹. Radial colour profiles do not hint on particle separation. The results support the view that V1331 Cyg underwent an FU Orionis outburst a few thousand years ago.

Additional data from other instruments - TLS, UKIDSS, SPITZER, HERSCHEL, SUBARU, PdBI and SMA is also incorporated. I use it to improve the understanding of the young star in terms of environment, viewing angle, bipolar outflow length and missing ring section. The gap between the outer and inner dust arcs is found to be real. HST planetary camera image reveals a knot like feature at 220 au from the central source. Subaru image shows scattered light in the same direction as that of the knot. Preliminary results from the latest PdBI continuum map also hint on the knot being a real feature. It is evident from the knot photometry that it is not a binary stellar companion. The starlight scattered from the dust is seen in HST images. Missing ring section could be a result of shadowing due to presence of the knot. By viewing V1331 Cyg almost pole-on, the length of the bipolar outflow is updated to be 10 parsec or even more.

Acknowledgements

Since the very outset to the accomplishment of my research during PhD, I pay my sincere gratitude to **Dr. Bringfried Stecklum**, my supervisor, who has introduced me to the marvelous world of star formation. His vast experience and knowledge has helped me immensely in learning the subject. Being a part of an international collaborative project during my PhD, I have seen various crucial dimensions of research. For this I wish to convey my sincere gratitude to **Dr. Karl Stapelfeldt**, Chief, Exoplanets and Stellar Astrophysics Laboratory, NASA-GSFC, USA. I thank both of them for taking the observations (HST general observer program-11976, based in part on observations made with the NASA/ESA Hubble Space Telescope) and patiently guiding me through my Thesis work.

I also thank **Prof. Dr. Artie P. Hatzes** Director, Thüringer Landessternwarte Tautenburg, Germany, for dealing with all the official paperwork and providing necessary facilities to carry out my research.

I like to acknowledge the kind hospitality and financial funds provided by **Thüringer Landessternwarte Tautenburg (TLS)** and **German Aerospace Center (DLR)**.

I thank my fellow research students at TLS for all their help and co-operation and also the rest of the faculty and staff at TLS for being very amiable and helpful in all respect.

Not to forget the unconditional support of my parents who showed me the way to believe in my dreams. My husband Ankit, who has been with me through all the tough times, thanks to him. And thanks to all those friends and family who showed trust in me and helped me make my way through the ups and downs in life.

Contents

Declaration of Authorship	iii
Abstract	v
Acknowledgements	vi
Contents	vii
List of Figures	xi
List of Tables	xiii
Abbreviations	xv
1 Introduction	1
1.1 Molecular Clouds	1
1.2 Collapse of molecular core	2
1.3 Star formation : Protostar	3
1.3.1 SEDs of Protostars	4
1.3.2 Evolution on the Hertzsprung Russell (HR) diagram	5
1.4 T Tauri Stars	7
1.4.1 Mass loss and variability	8
1.4.2 Observational properties	8
1.4.3 The prototype : T Tauri	8
1.5 Circumstellar disks	9
1.5.1 SEDs of disks	9
1.6 Bipolar outflows and HHO	10
1.6.1 The objects of Herbig and Haro	11
1.7 FUor phenomenon	12
1.7.1 Triggering mechanisms	12
1.7.2 The prototype: FU Ori	13
1.7.3 Properties of FUors	13

1.8	Disk evolution : Planet formation	14
1.9	Cosmic Dust properties	16
1.9.1	Scattering and absorption	16
1.9.2	Forward scattering	16
1.9.3	Types of scattering	17
1.9.4	Interstellar absorption	18
1.9.5	Extinction and reddening	19
1.9.6	Interstellar scattering	21
1.9.7	Dust re-emission	22
1.9.8	Light polarization	22
2	Literature Survey	25
2.1	V1331 Cyg, The special one	25
2.2	Research motivation	28
3	Telescopes and Observations	31
3.1	The Hubble Space Telescope	31
3.1.1	Observations with HST	32
3.2	Data from UKIDSS	33
3.3	Alfred Jensch Telescope-TLS	34
3.3.1	TLS observations for bipolar outflow and HHO	34
3.4	Spitzer data	35
3.5	Subaru archival data	35
3.6	Herschel/PACS observations	36
3.7	Plateau de Bure Interferometer (PdBI) observations	37
3.8	Submillimeter array (SMA) data	38
4	Data reduction and analysis	39
4.1	HST image cleaning	39
4.1.1	Cosmic Rays and bad pixels	39
4.2	WF3 background correction	42
4.3	PSF subtraction for V1331 Cyg	42
4.4	Dust arcs analysis	44
4.4.1	Outer arc	44
4.4.2	Inner arc	49
4.5	HST F606W images direct subtraction	50
4.6	Particle separation hypothesis	52
4.7	Photometry of V1331 Cyg	53
4.8	Photometry of outer dust arc	56
4.9	Outer dust arc reddening analysis	57
4.10	Outer dust arc colour-brightness relation	59
4.11	UKIDSS reddening analysis	60
4.11.1	Photometry on UKIDSS data	60
4.12	HERSCHEL/PACS results	66
4.13	V1331 Cyg Bipolar Outflow	67

4.13.1	HHO spectroscopy	69
4.14	South west ridge extension	70
4.15	V1331 Cyg SED	71
4.16	New scattering knot close to the star	72
4.16.1	Subaru-CIAO coronagraphic imaging	72
4.16.2	Self subtracted HST knot photometry	74
4.17	PdBI data	75
4.18	SMA observations	77
5	Results and Discussion	79
5.1	Origin and radial expansion of outer and inner arc	79
5.1.1	Possibility one: Ambient cloud material	80
5.1.2	Possibility two: FUor outburst remnants	80
5.2	Reason behind outer arc brightness and colour behaviour	81
5.2.1	Spiral shaped outer arc	81
5.2.2	Elliptical shaped torus	82
5.3	Southwest ridge and possible elliptical arc extension	83
5.4	Missing ring section	83
5.4.1	Role of dark cloud	83
5.4.2	Inner knot discovered	84
5.5	Bipolar outflow and HH objects	85
5.6	V1331 Cyg SED	85
6	Conclusions and future work suggestions	87
6.1	Conclusions	87
6.2	Outlook to the future	88
A	Additional content	89
A.1	P Cygni profile	89
B	IDL scripts	91
B.1	WF3 Camera background correction script	91
B.2	Script to calculate transformation parameters using SVD algorithm	92
B.3	Script to remap second epoch image to match first epoch	95
B.4	Script to calculate expansion in dust arcs between two epochs	96
C	V1331 Cyg SED	99
	Bibliography	103
	Curriculum Vitae	119

List of publications and talks

121

List of Figures

1.1	Molecular cloud collapse sketch	4
1.2	SEDs of protostars	6
1.3	HR diagram	7
1.4	SED of Disk	10
1.5	Herbig Haro Objects	12
1.6	FUor object sketch	13
1.7	Types of scattering	17
1.8	Extinction and reddening	20
2.1	V1331 Cyg photographic plate image	26
3.1	WFPC2 instrument layout	32
4.1	Cosmics and bad pixel effected image	40
4.2	IRAF Cosmicrays window	41
4.3	Tiny Tim model PSF	43
4.4	PSF subtracted image	44
4.5	Astrometry using 11 stars	46
4.6	Astrometry on WF3 frames	49
4.7	Radial plots for dust arcs	51
4.8	HST direct difference image	52
4.9	Radial colour profiles	54
4.10	colour profiles for separate arc sections	55
4.11	Apertures used to calculate reddening	57
4.12	Azimuthal median profile	58
4.13	F814W flux weighted image	60
4.14	Brightness colour plot	61
4.15	UKIDSS JHK composite image	62
4.16	2MASS vs. UKIDSS magnitudes	63
4.17	JHK colour-colour plot	64
4.18	Smoothed UKIDSS image	65
4.19	Herschel colour composite image	66
4.20	Bipolar outflow and HHOs	68
4.21	HHO spectra	69
4.22	Newly found arc	70
4.23	SED fit for V1331 Cyg	71

4.24 Inner knot in HST vs. Subaru	73
4.25 HST self subtracted image	74
4.26 PdBI UV field coverage	75
4.27 PdBI continuum map	76
4.28 PdBI CO (2-1) line	76
4.29 SMA continuum map	77
A.1 P Cygni profile	90

List of Tables

1.1	Accretion disk properties	9
1.2	List of known FUors	14
3.1	HST WFPC2 camera specifications	31
3.2	V1331 Cyg observations with HST	33
3.3	V1331 Cyg data from UKIDSS	33
3.4	TLS Schmidt configuration	34
4.1	V1331 Cyg spectrum input to Tiny Tim	42
4.2	Stellar coordinates of first epoch stars	45
4.3	Stellar coordinates of second epoch stars	47
4.4	Transformation parameters for outer dust arc	47
4.5	Stellar coordinates of first epoch WF3 frame stars	50
4.6	Stellar coordinates of second epoch WF3 frame stars	50
4.7	Transformation parameters for inner arc	50
4.8	V1331 Cyg photometry	56
4.9	Outer dust arc photometry	56
4.10	Outer arc colour indices	58
C.1	V1331 Cyg Input fluxes to SED fitter	99
C.2	Stellar parameters from SED fitter	101

Abbreviations

2MASS	2 Micron All Sky Survey
AU	Astronomical Unit
CCD	Charge Coupled Device
CIAO	Coronagraphic Imager with Adaptive Optics
DSS	Digital Sky Survey
ESA	European Space Agency
FUor	FU Orionis
HHO	Herbig Haro Object
HLA	Hubble Legacy Archive
HR diagram	Hertzsprung Russell diagram
HST	Hubble Space Telescope
IDL	Interactive Data Language
IRAC	InfraRed Array Camera
IRAF	Image Reduction and Analysis Facility
IRAM	Institut de Radioastronomie Millimetrique
IRS	InfraRed Spectrograph
IRSA	InfraRed Science Archive
ISM	InterStellar Medium
MAST	Mikulski Archive for Space Telescopes
MSX	Midcourse Space Experiment
NASA	National Aeronautics and Space Administration
NOEMA	NORthern Extended Millimeter Array
PACS	Photoconductor Array Camera and Spectrometer
PdBI	Plateau de Bure Interferometer

PSF	P oint S pread F unction
SCUBA	S ubmillimetre C ommon U ser B olometer A rray
SED	S pectral E nergy D istribution
SMA	S ub M illimeter A rray
SMOKA	S ubaru M itaka O kayama K iso A rchive
SPIRE	S pectral and P hotometric I maging R Eceiver
STScI	S pace T elescope S cience I nstitute
TLS	T hüringer L andes S ternwarte
TTS	T T auri S tars
UKIDSS	U K I RT I nfrared D eep S ky S urvey
UKIRT	U K I nfra R ed T elescope
WFCAM	W ide F ield I nfrared C A M era
WFPC	W ide F ield P lanetary C amera
WISE	W ide F ield I nfrared S urvey E xplorer
YSO	Y oung S tellar O bject
ZAMS	Z ero A ge M ain S equen S e

To my Family

Chapter 1

Introduction

1.1 Molecular Clouds

A molecular cloud is an accumulation of interstellar gas and dust. With temperatures ranging between 10 and 30 Kelvin, the main component of a molecular cloud is molecular hydrogen (H_2). Out of all the hydrogen in interstellar medium (ISM), less than one percent of it in Milky Way is bound in molecular clouds. Rest of it is in the form of atomic hydrogen, but holds the possibility of becoming a molecular cloud in the future. Molecular clouds can have varying sizes, between a few light years to few hundreds of light years. Their total mass can be as large as few million solar masses. A cloud with a size of 15 light years or more is termed as Giant Molecular Cloud (GMC). Such massive and dense molecular clouds are the major sites of star formation, with stars forming at a rate of about $3 M_{\odot}$ per year throughout the Milky Way [1], using gas in these clouds. Some nearby molecular clouds are seen as dark clouds against the bright Milky Way background because dust in such clouds absorbs starlight from the more distant stars. Though the amount of dust present in molecular clouds is only one percent to that of gas, it still plays a vital role in making of molecular clouds, as it absorbs ultraviolet radiation further leading to dissociation of molecules.

Larson [2] estimated the average density of a whole GMC to be of the order of 20 H_2 molecules per cm^3 , with larger clumps inside having densities of the order of 10^3 H_2 molecules per cm^3 . The smallest gravitational bound units are often termed as cores. During the process towards star formation, cores may have 10^5 H_2 per cm^3 density or even more. High densities and low temperatures are the characteristic

properties of GMCs, with self gravity dominating over thermal pressure. If thermal pressure was the only stabilizing force against gravity, molecular clouds would quickly collapse to form stars. In reality, these clouds are not so efficient in forming many stars, typically shifting only a few percent of their mass into stars, with the rest being dispersed later. The inefficiency of molecular clouds in transferring their mass into stars led to the conclusion that, the molecular clouds are stabilized against self gravitational collapse by magnetic fields and magneto-hydro-dynamic (MHD) turbulence [3].

1.2 Collapse of molecular core

The concept which predicts as to how the collapse of a molecular cloud core might be initiated [2] is the following:

Gravitational instability The stability analyses and fragmentation simulations suggest that the collapse begins when gravity starts dominating over thermal pressure in an unstable clump of gas. The molecular cloud clump would be considered stable for sufficiently small mass, but once this mass exceeds certain critical value called as **Jeans mass**, it leads to a runaway collapse [4].

Jeans criterion developed by Jeans [5] suggests that perturbations with short wavelength are pressure dominated and propagate as sound waves, while others with wavelength above the critical 'Jeans length' are gravity dominated. For an isothermal medium with uniform density (ρ) and constant temperature T, Jeans length λ_J can be expressed as:

$$\lambda_J = \sqrt{\frac{\pi}{G\rho}}c \quad (1.1)$$

where, $c = \sqrt{\frac{kT}{m}}$ is the isothermal sound speed and m is the average particle mass.

Spitzer [6] estimated corresponding 'Jeans mass' as:

$$M_J = \frac{5.57c^3}{G^{3/2}\rho^{1/2}} \quad (1.2)$$

Additional effect playing a role towards cloud collapse is **Magnetic field effect**. It assumes that the cloud cores initially have magnetic field, which gradually

condenses by ambipolar diffusion and the gas starts contracting slowly across the field lines [7].

However, the above mentioned concept does not offer a perfect solution to the collapse problem, rather provides a useful reference model. More realistic solution to the problem exists through fragmentation and mass outflow in a molecular cloud by using magneto-hydrodynamic (MHD) simulations [8].

1.3 Star formation : Protostar

Most of the prestellar cloud cores are found to be slowly rotating. The slow rotation can be attributed to loss of angular momentum by magnetic braking [9]. The protostellar magnetic field captures material along the field lines. During early stages of cloud evolution, this material after reaching certain critical radius, escapes the field lines, taking away the excess angular momentum along with it. The core starts to collapse, and during the later stages of collapse, magnetic fields are predicted to decouple from the gas by ambipolar diffusion [7, 10, 11]. The angular momentum is then expected to be almost conserved on scales smaller than a few hundredths of a parsec [12, 13].

The angular momentum (rotation) cannot prevent collapse, it rather affects the structure of the collapsing core which is characterized by regions [14] as shown in Fig. 1.1.

The rotating cloud produces a structure, with :

- An accreting core in the centre, having radius R_*
- An accretion disk with $R_* < R < R_c$; where R_c is the centrifugal radius
- A roughly spherical envelope in free-fall, i.e. $R_c < R < R_{inf}$; where R_{inf} is the infall radius
- Static isothermal shell, $R_{inf} < R < R_{out}$; where R_{out} is the outer radius of the bound structure
- $R > R_{out}$, the ambient cloud

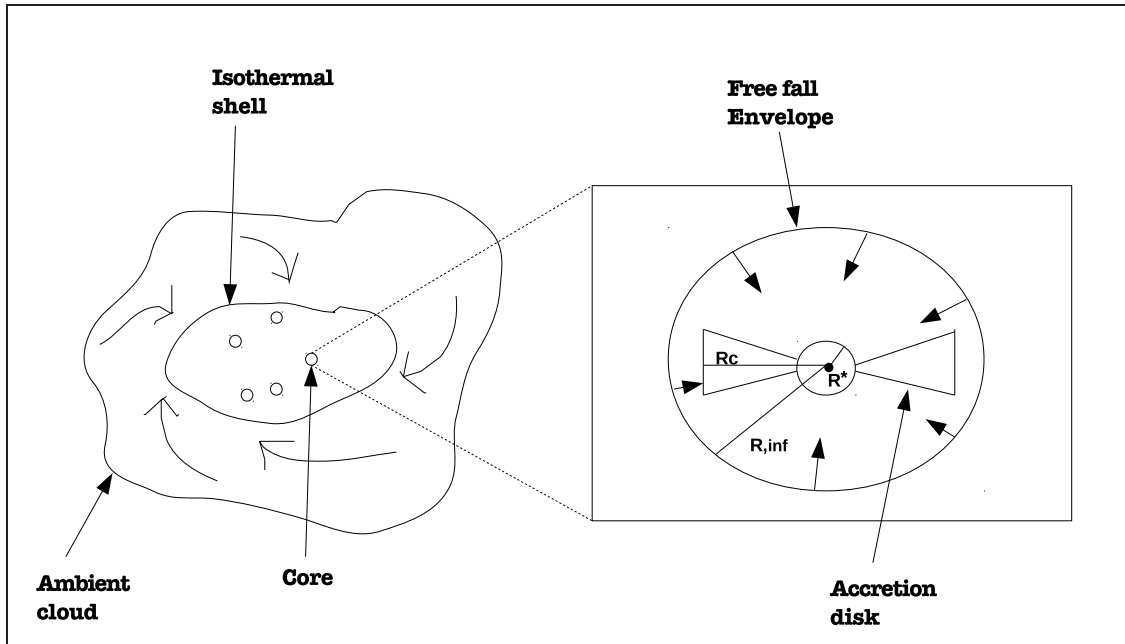


FIGURE 1.1: Schematic diagram showing the structure of a collapsing core

Mass of the collapsing core increases from a low value at the beginning of collapse to stellar masses as :

$$M_* = \dot{M}_{acc} \times t$$

where, \dot{M}_{acc} is the gas+dust accretion rate.

1.3.1 SEDs of Protostars

The protostellar population can be divided into sub classes based on their spectral energy distribution (SED), which tells us something about their evolutionary stage. Class I to III were defined by the SED of a protostar as discussed in Lada [15]. Class I sources have spectra broader than a blackbody and show a peak near 100 micron. These objects are found to have envelope masses comparable to the mass of the collapsing core. Envelopes also have bipolar cavities generated by outflows. They have well developed accretion disks, whose emission can sometimes be detected in mid-infrared [16]. Class II stars show excess infrared emission than what is expected from a stellar photosphere. They are the classical T Tauri stars (TTS) with SED emission peak in the near infrared and excess IR emission hints on the presence of an accretion disk around the source. Class III stars exhibit

SEDs dominated by stellar photosphere. The peak of the SED shifts to shorter wavelengths suggesting that the central source is now less embedded than before. The star reaches zero age main sequence (ZAMS) after this stage ends. Andre et al. [17] found one of the youngest protostellar source, VLA 1623, to be still embedded in the infalling envelope, surrounded by massive circumstellar structure. The SEDs of such objects do not fit into the classes (I-III) defined earlier. Hence, a new class 0 was coined to indicate the star's extremely young age by Andre et al. [17], who also found that class 0 SEDs resemble blackbodies with $T \leq 30$ K. Interestingly, these sources, in such an early stage of collapse, already host powerful bipolar outflows. The SEDs of all four classes are shown in Fig. 1.2.

1.3.2 Evolution on the Hertzsprung Russell (HR) diagram

Chushiro Hayashi in 1962 found that the contracting protostar of any given mass lies on an essentially vertical line on the HR diagram. This line called as Hayashi line is the locus of fully convective protostars of given parameters (mass and temperature) in the HR diagram. For each set of parameters, there is a separate Hayashi track (one such track shown in Fig. 1.3 in red). These tracks are obeyed by pre-main-sequence stars with mass less than $3M_{\odot}$. These very steep and mostly vertical tracks are located at the right most part of the HR diagram, at about 3000 to 5000 K. The region to the further right of Hayashi track is called **forbidden zone**. The complete pre-main-sequence evolutionary track from initial molecular cloud with low luminosity and surface temperature to luminosity higher than main sequence, does pass through the forbidden zone.

By the time dense infalling envelope is dissipated, and the star becomes visible in optical wavelengths, the protostellar phase comes to an end. This is marked by decrease in accretion rate to very low values ($\leq 10^{-7}M_{\odot} \text{ yr}^{-1}$). The star is by now in hydrostatic equilibrium and by slow contraction, it evolves on the Kelvin Helmholtz timescale, towards the ZAMS [19]. Different evolutionary stages of a star life are governed by different triggering mechanisms responsible for its luminosity. Observationally it is not so straightforward to predict the evolutionary stage of a star. But in theory, the stages are well characterized by the different means of dominant stabilizing forces. Accretion is solely responsible for luminosity in protostellar phase, contraction in the pre-main-sequence phase and nuclear fusion of hydrogen, once the star reaches ZAMS.

On the HR diagram, pre-main-sequence stars sit to the right of ZAMS [20] (refer to Fig. 1.3). The age and mass of any pre-main-sequence star can be determined by comparing its position to the evolutionary tracks on the HR diagram. Ages of these young objects lie in the range from approximately 10^5 to 10^7 years.

Depending on their mass, pre-main-sequence stars can be divided in two categories. Low mass TTS with $M_* \leq 2M_\odot$ and intermediate mass Herbig Ae/Be stars with $2 \leq M_* \leq 8M_\odot$. Interestingly enough, the higher mass stars do not have

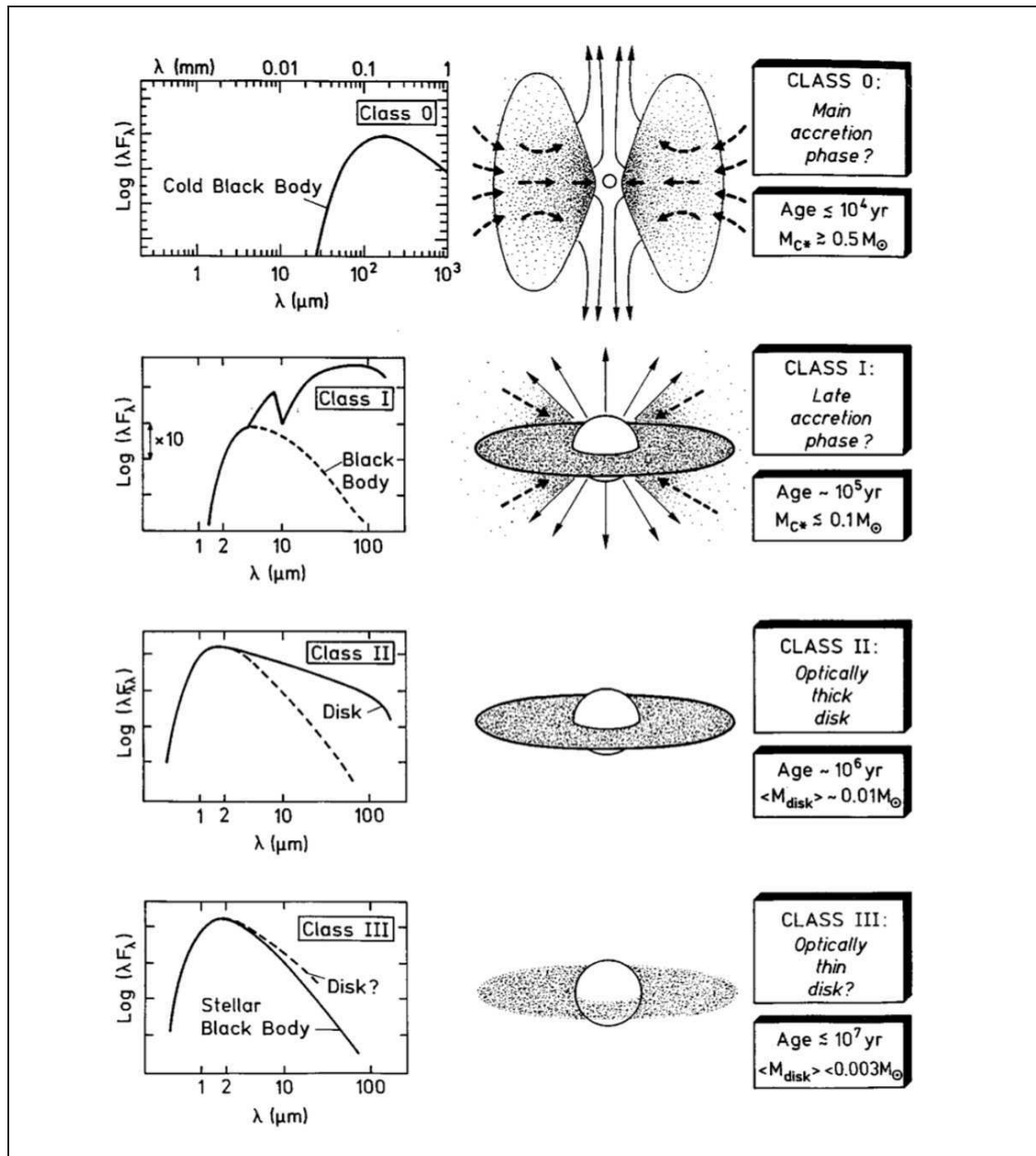


FIGURE 1.2: SEDs of all four class of protostars shown alongside with the evolutionary phase. SED images are adapted from Bachiller [18] and Lada [15].

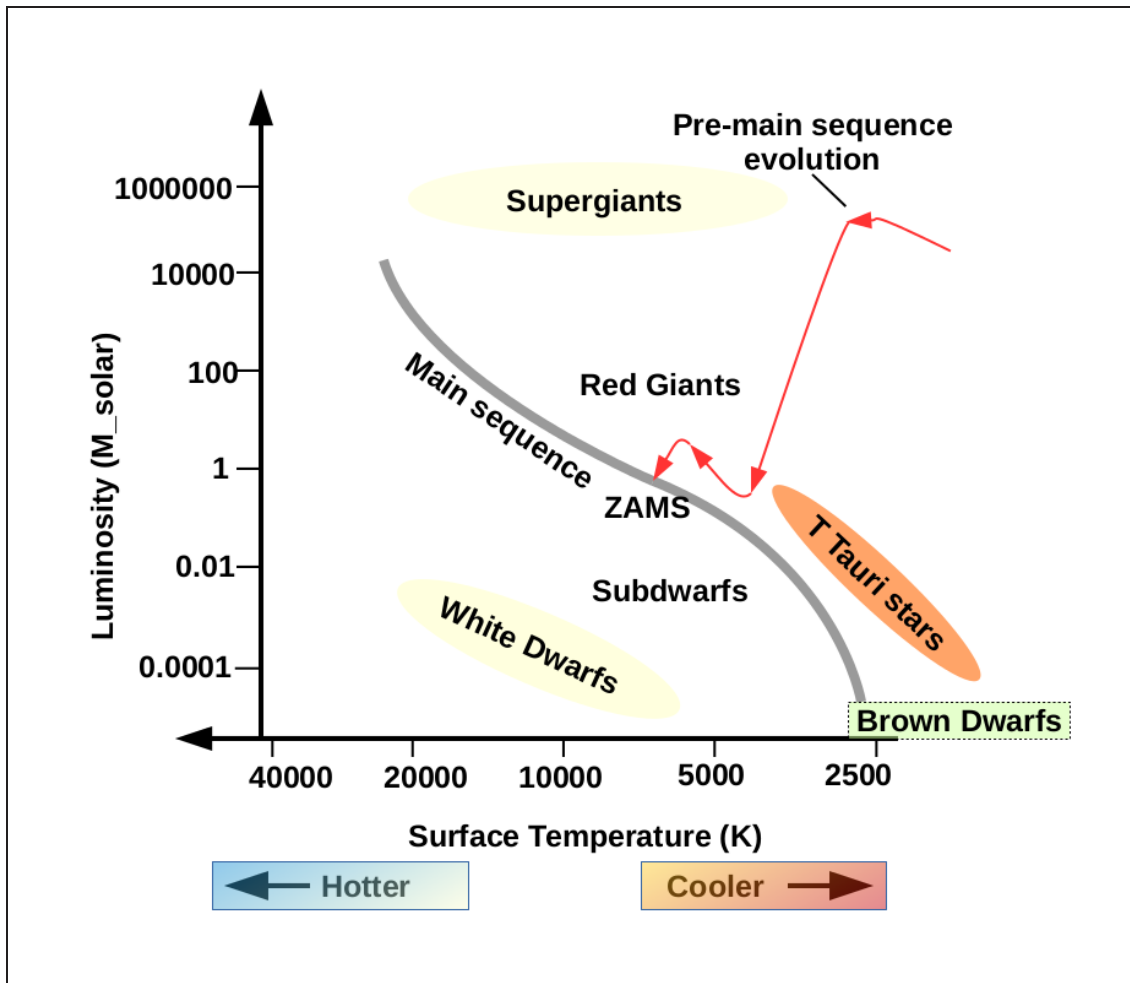


FIGURE 1.3: Schematic diagram showing the location of TTS on the HR diagram.

a pre-main-sequence phase as they directly reach the ZAMS while still accreting mass.

1.4 T Tauri Stars

TTS [21] are the class of low mass, young pre-main-sequence stars still in the process of gravitational contraction (Ambartsumian [22]). TTS start up their lives as slightly cool stars. Heating up with time, they get bluer and slightly fainter. TTS are almost always found embedded in a dark cloud of gas, which is their birth place as well.

1.4.1 Mass loss and variability

TTS are highly variable class of stars. They are mostly surrounded by hot and dense envelopes. Enhanced accretion from thick accretion disk leads to mass loss in variability episodes (discussed in detail in later sections of the chapter) via stellar winds with velocities of about 100 km s^{-1} . An infant star going through its T Tauri phase can lose some fraction of its mass while still a pre-main-sequence star.

1.4.2 Observational properties

TTS spectral type can range from A through M with (B-V) colour ranging from about 0.47 (RU Lup [23]) to 1.33 (V410 Tau [24]). Herbig [25] suggested that to put a star in TTS class, it should display following spectroscopic properties :

- Strong emission lines from H alpha (Balmer series), Ca II at 3933 \AA , and 3968 \AA .
- Fluorescent Fe I emission lines at 4063 and 4132 \AA (these are only found in TTS).
- Absorption lines of Li I at 6707 \AA .
- Forbidden lines of [O I] and [S II] are also characteristic.

1.4.3 The prototype : T Tauri

Although considered to be the prototype of low mass pre-main-sequence stars, T Tauri itself was known for very peculiar characteristics. It was surrounded by Burnham's reflection nebula [26], which extended to several arcseconds south of the star. At optical wavelength coronagraphic images of T Tauri [27], an arc like reflection nebulosity was seen, extending from north of the star to the north west. Hubble Space Telescope (HST) images also revealed a similar feature with a bright tail pointing towards the south west. Stapelfeldt et al. [28] interpreted the feature as produced by a limb darkening cavity. Regarding the viewing angle, there was controversy in the model depictions of viewing the star at 45° from the outflow axis vs. the observations made by Herbst et al. [29], suggesting the star to be

seen almost pole-on. Later on, it was found that T Tauri is not a special case. Observations show that most, if not all stars form in binary/multiple systems [30] and are surrounded by reflection nebulae. However, the reflection nebulae only show up at the later stages of pre-main-sequence, since earlier on, YSOs are more deeply embedded.

1.5 Circumstellar disks

Rotating core collapse gives rise to the circumstellar disk, which is an essential component in the process of star and planet formation. Protostars are known to have disks, and a bigger section of pre-main-sequence stars also possess disks. The disk is heated both by viscous dissipation and radiation from the central star. Strong magnetic field of the star disrupts inner part of the accretion disk [31]. One fraction of disk material falling onto the star follows closed magnetic field lines, whereas, a minor fraction (few percent) gets ejected out of the system in the form of jets and outflows, discussed in detail in Hartmann [32]. The typical disk properties associated with pre-main-sequence stars are listed in Table 1.1.

TABLE 1.1: Accretion disk properties

Parameter	Value
Mass (M_{\odot})	0.003 to 0.3
Mass accretion rate (\dot{M})	10^{-8} to $10^{-6} M_{\odot} \text{ yr}^{-1}$
Inner radius	1 to few R_{*}
Outer radius	~ 100 au

1.5.1 SEDs of disks

The majority of circumstellar disks emit at infrared, sub-millimeter and millimeter wavelengths. Disk is cooled at infrared wavelengths by thermal emission from dust grains. The thermal emission observed for a dusty disk model is comprised of three wavelength regions as shown in Fig. 1.4. The near-infrared peak originates from the inner most puffed-up region of the disk. The dust in this region sublimates [33] with temperatures exceeding 1500 K. The puffed up inner rim may shadow the dust in outer regions from direct starlight, thus, influencing the structure of outer disk regions. Infrared dust features on the SED come from warm surface layers.

For typical TTS, main portion of the energy is radiated away in the wavelength range between 1 and 100 micron, known as “energetic domain of SED” [34].

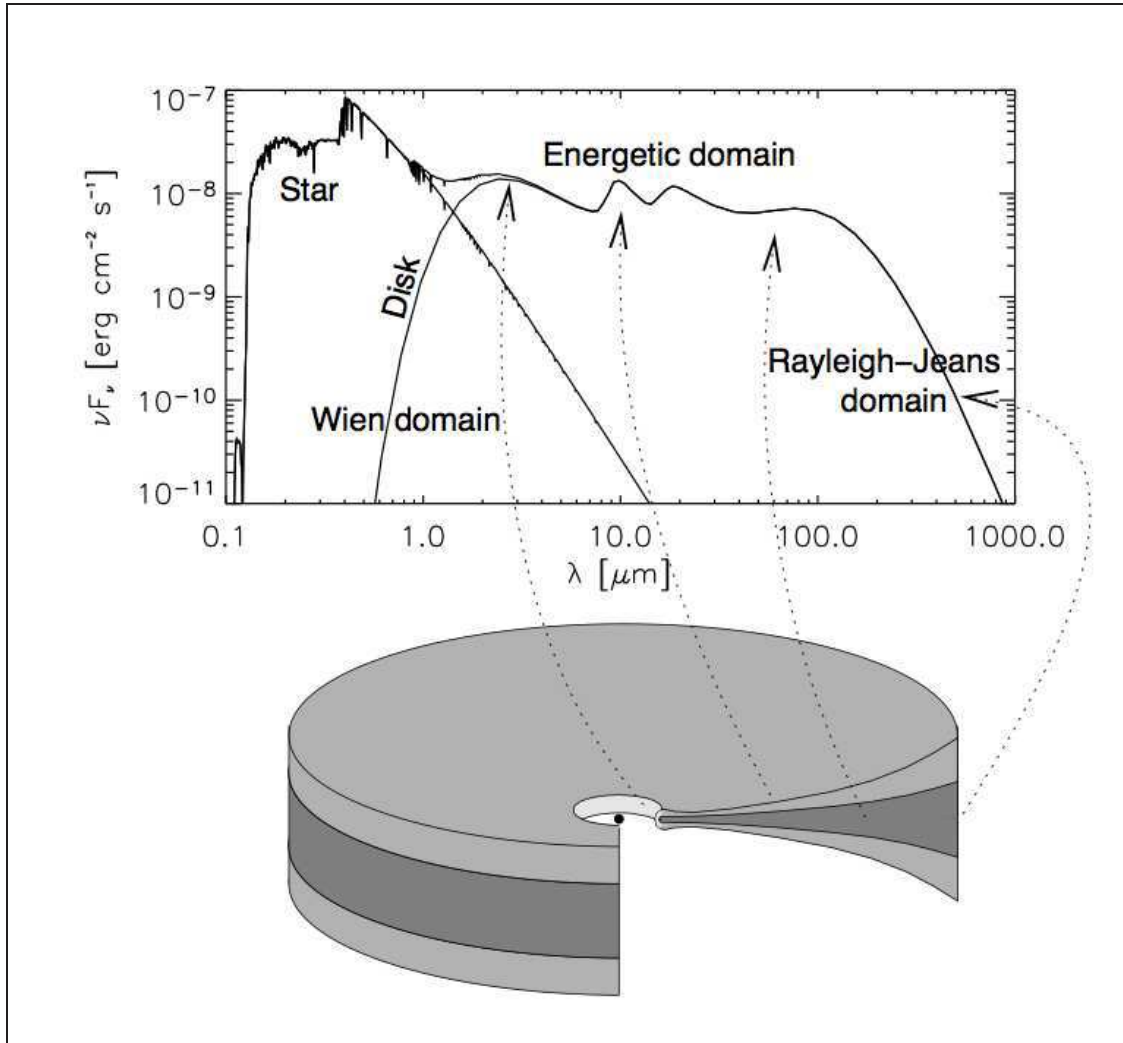


FIGURE 1.4: Build-up of the SED of a flaring protoplanetary disk and the origin of various components, adapted from Dullemond et al. [34].

1.6 Bipolar outflows and HHO

The accretion disk material needs to get rid of excess angular momentum before it falls onto the star. Viscosity helps in transporting the net momentum outwards in a disk, allowing material to spiral inwards [35]. But for a Keplerian disk, the angular momentum of the material approaching the star is still higher than what the star can absorb. Since most stars form not in isolation, but in binary or multiple systems, the companion can play a major role in redistributing the angular

momentum. Even then, the leftover momentum from the star can be removed in the form of energetic bipolar outflows, discovered by mm-wave molecular line observations by Snell et al. [36] and Lada [37].

The energetic flow of cold molecular gas is “bipolar” in the sense that it travels in two diametrically opposite directions, moving away from the protostellar core at hypersonic velocities. The primary wind generated at the core is released by the highly collimated circumstellar jet. The outflows are ejecta from the embedded star, which, by friction, cause the ambient matter to entrain the flow and thus also consist of swept up accretion disk material. Such “accretion driven” outflow holds the power to change the way, the protostar evolves.

Bipolar outflows from young stellar objects (YSOs) consist of ionized, atomic and molecular gas present at different levels of excitation. Discovery of high velocity molecular gas producing broad CO lines at mm-wavelengths, towards the Orion A molecular cloud was done by (Kwan and Scoville [38] and Zuckerman et al. [39]).

1.6.1 The objects of Herbig and Haro

Fast moving jets travel at a speed of about 150 km s^{-1} away from a young star. Their collision with the ISM gives rise to small-scale shock regions known as Herbig Haro objects (HHO) (see Fig. 1.5). These objects appear as small patches of nebulosity and are often seen aligned to the parent stars rotational axis.

They were first observed by the astronomers Herbig [26, 40] and Haro [41, 42] and thus the name. Known to be strong sources in infrared (due to shock excited H_2), most of the HHOs lie within the dark clouds. Characteristic emission from HHOs in optical spectra is credited to formation of thin shock front in the ISM. The shock front contains heated and ionized gas, followed by an extended “cooling zone” (Ostriker and McKee [43]). Gas in the cooling zone emits forbidden lines of metals and recombination lines of hydrogen. The neutral hydrogen atoms from the preshock material while entering the shock, get excited by collisions, giving rise to strong Balmer line emission from the shock front (Chevalier and Raymond [44], Heathcote et al. [45]).

Typical HHOs have temperatures of around 10000 K, with densities ranging from few thousand to a few hundred thousand particles cm^{-3} and can have masses

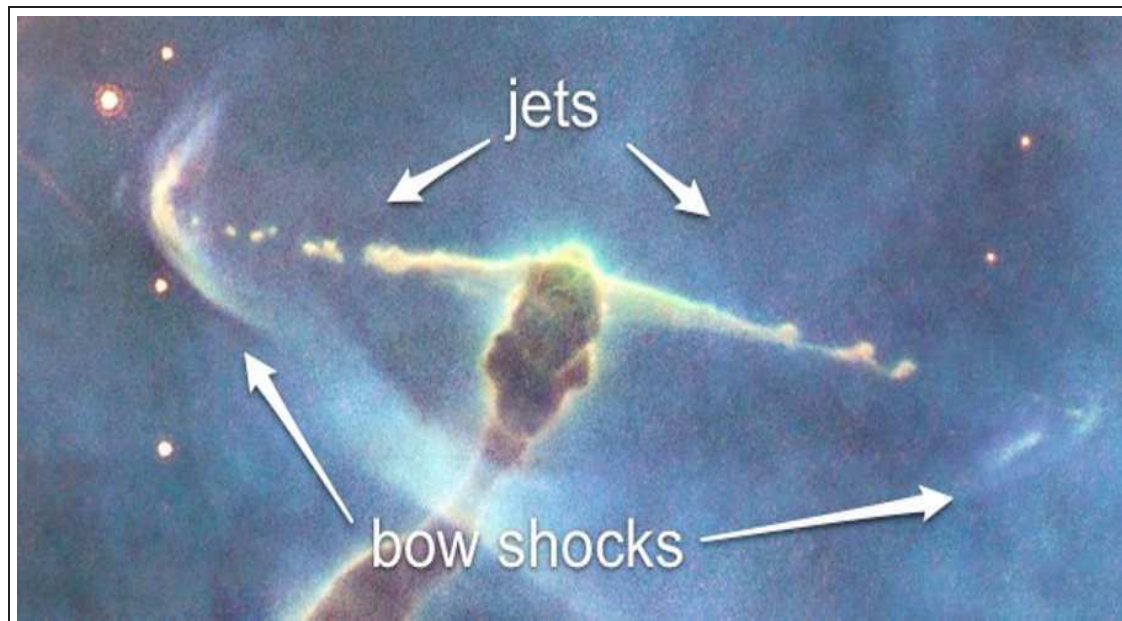


FIGURE 1.5: The large-scale structure of the bipolar jet HH901 observed in the Carina Nebula. Image credit : NASA, ESA, and M. Livio and the Hubble 20th Anniversary Team.

up to 20 Earth masses. HHOs can emit X-rays as well, and some jets can also be seen in the radio continuum.

1.7 FUor phenomenon

During accretion phase, when mass accretion rate from the circumstellar disk onto the young star increases by orders of magnitude, it gives rise to FU Ori (FUor) outbursts [46]. In this process, the disk outshines the central source by a factor of 100 to 1000 in optical. A strong wind emerges, which can affect the surrounding interstellar medium considerably.

1.7.1 Triggering mechanisms

There is no certain proof or reasoning behind FUor outbursts, instead there are a few accepted hypothesis:

- Thermal instability of the circumstellar disk can lead to a short period of strongly enhanced accretion

- A close companion can trigger density perturbations in a disk
- Gravitational disk instability might be a possibility as well

1.7.2 The prototype: FU Ori

The prototype FU Orionis is a faint red variable star in the dark cloud B35 in the λ Ori region. In 1936, it showed a rise in brightness by 6 magnitudes, within a very short period of about four months. The detailed discussion can be found in Wachmann [47, 48] and Herbig [49, 50].

1.7.3 Properties of FUors

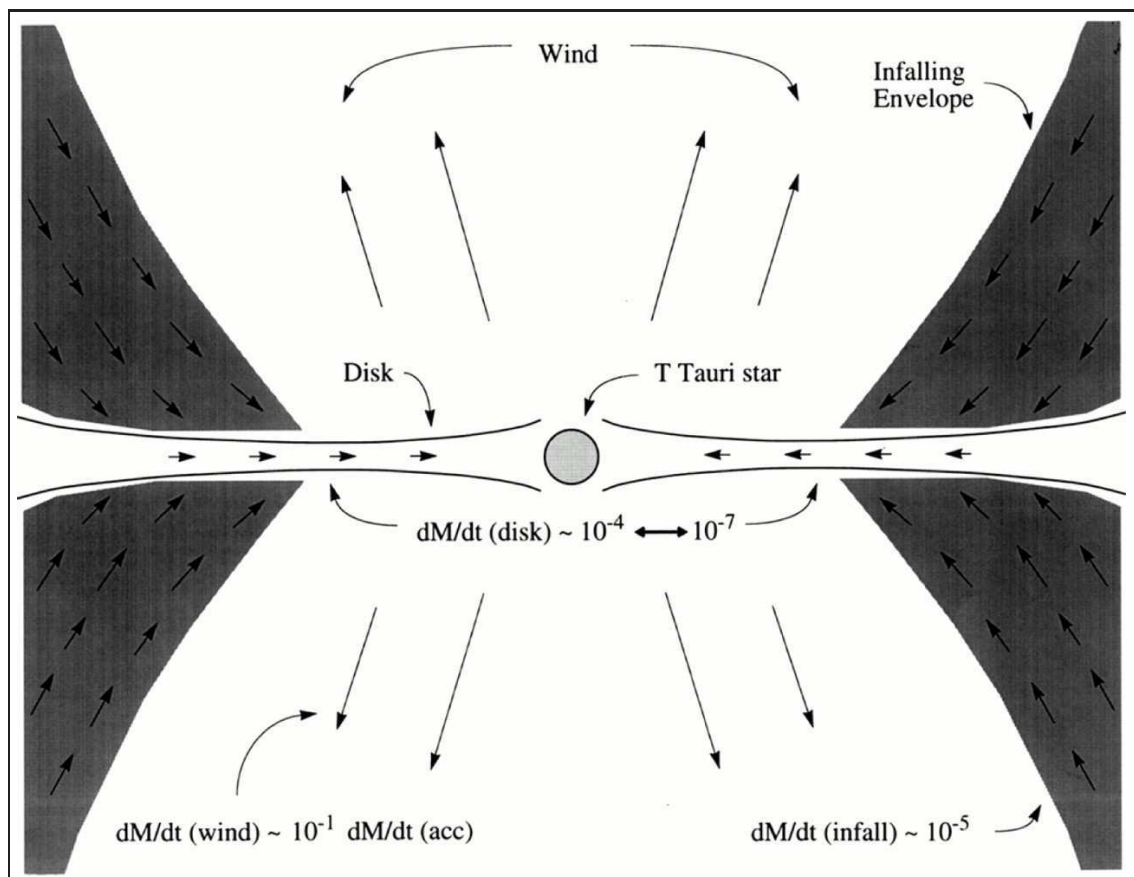


FIGURE 1.6: Schematic picture of FU Ori objects. Figure adapted from Hartmann and Kenyon [46].

FUors in general have considerably high luminosities, indicating that the source of excess light is the disk itself. Accretion rates of around $10^{-4} M_{\odot} \text{ yr}^{-1}$ or even more are required to achieve a high FU Ori state. The hot disk then radiates most of its energy in optical wavelengths. Though all young stars do not compulsorily go through the FUor stage, but those which do, gain at least 10% of their total final mass during the outburst, which on average, could last for a century. Figure 1.6 shows a sketch of FUor objects, and a list of observed FUors is given in Table 1.2.

TABLE 1.2: FUors which have already been observed in the past

Source	R.A.	Dec.	Eruption year	Reference
V883 Ori	05: 38: 18.1	-07: 02: 26	< 1888	Strom and Strom [51]
FU Ori	05: 45: 22.4	+09: 04: 12	1936	Herbig [50]
V1515 Cyg	20: 23: 48.0	+42: 12: 26	~ 1950	Herbig [50]
HH381 IRS	20: 58: 21.4	+52: 29: 27	1952–1989	Reipurth and Aspin [52]
V1735 Cyg	21: 47: 20.7	+47: 32: 04	1952–1965	Elias [53]
V733 Cep	22: 53: 33.3	+62: 32: 24	1953–1984	Reipurth et al. [54]
V1057 Cyg	20: 58: 53.7	+44: 15: 29	1969	Herbig [50]
V346 Nor	16: 32: 32.1	-44: 55: 31	~ 1980	Graham and Frogel [55]
HH629 IRS	21: 00: 25.4	+52: 30: 16	1999	Movsessian et al. [56]
V1647 Ori	05: 46: 13.1	-00: 06: 05	2003	Reipurth and Aspin [57]

Very broad, deep P Cygni absorption (refer to Appendix A for details) seen in Balmer lines of FUors suggest that they have strong winds (Bastian and Mundt [58]). Mass loss rate from FU Ori wind is about $10^{-5} M_{\odot} \text{ yr}^{-1}$ (Croswell et al. [59], Calvet et al. [60]), whereas, mass loss rate for a TTS wind is $\leq 10^{-8} M_{\odot} \text{ yr}^{-1}$ (Edwards et al. [61], Hartigan et al. [62]). Such a huge difference in mass loss rate suggests that mass accretion and ejection are directly related to each other. Also, the strong FUor winds show spectroscopic signatures of mass loss that are not detected in T Tauri winds.

1.8 Disk evolution : Planet formation

During the first 10^5 years of an accretion disk, it undergoes accretion with extremely high mass accretion rates and witnesses some of the most violent outflow activities. Rapid, gravitationally driven disk fragmentation, in distant disk regions [63] leads to the formation of giant gas planets. Also, over million year timescales,

rocky planetary cores form by accreting massive gaseous envelopes [64]. In any case, disk mass plays the most important role for both star and planet formation. The star gets most of its mass from the disk through accretion. At the same time, to form planets, they must get their share of gas from the same disk reservoir.

Massive circumstellar disks having about one-tenth part of stellar mass can generate strong spiral waves, which in turn would drive rapid accretion onto the central star. When closely coupled gas and dust grains in the disk start to grow by mutual collisions, they settle down in the disk midplane. They first form bigger grains and then planetesimals (about 1 km size objects). Such planetesimals get decoupled from the gas and start orbiting the central source in Keplerian orbit. A planetesimal keeps growing by inelastic collisions until all the matter in its “accretion” zone is swept up, resulting in a large rocky body. A pre-main-sequence disk may give birth to many such isolated rocky bodies in a time span of about 10^6 years. Longer times of about 10^8 years are required to form terrestrial planets and cores of giant planets. Whether the central star disposes its disk by radiation wind to planet formation versus disk destruction, is actually a race against time.

Detecting planetesimals is not possible yet. To search for grain growth and planet formation, one should look for disappearing emission from the disk. Since the grain growth occurs in the disk midplane, observations at long wavelengths (specifically millimeter regime), where pre-main-sequence disks are optically thin, can provide an opportunity to detect planet formation signatures. However, there have been instances, when comets falling into the pre-main-sequence stars have been observed owing to redshifted absorption lines, for example Beta Pictoris [65].

In the rough environment around a young star, comets and planetesimals frequently collide and generate fragments that release dust, icy grains and stored gases and make it favourable for planet formation. However, due to violent collisions, there is both growth and destruction of larger bodies at the same time. This is why, such disks are called as Debris disks (refer to Krivov [66] & Wyatt [67]).

1.9 Cosmic Dust properties

Interstellar dust comes in dust clouds and is also spread diffusely throughout space. Dust grains play a vital role in the astrophysics of the interstellar medium, from the thermodynamics and chemistry of the gas to the dynamics of star formation. The interstellar dust grains absorb, redden and scatter light. The detailed observational analysis of interstellar dust properties can be found in Draine [68], the subject is also thoroughly described in Krügel [69].

1.9.1 Scattering and absorption

Scattering of an electromagnetic wave by any system is related to the heterogeneity of that system on molecular scale or on the scale of aggregations of many molecules. Regardless of the type of heterogeneity, underlying physics of scattering is the same for all systems.

The obstacle matter is composed of protons and electrons. When such an obstacle (atom, molecule, solid, liquid) is illuminated by an em wave, electric charges in the obstacle are set into oscillatory motion by the electric field of the incident wave. The accelerated charges then radiate em energy in all directions as secondary radiation **scattered** by obstacle. The propagation and interaction of electromagnetic fields when encountered by objects or obstacles is described using **Maxwell's equations**. In addition to scattering, the excited charges may transform some part of incident em energy into other forms (thermal etc.), a process called **absorption**.

These processes are not mutually independent. The amount and angular distribution of the light scattered by the particle and the amount absorbed depends on shape, size and the type of material of the particle.

1.9.2 Forward scattering

Forward scattering characteristics are very different than light scattered in any other direction. Firstly, it is not possible to separate the incident beam from the light scattered in forward direction. Secondly, for a collection of identical particles near the forward direction, there is a random distribution of phase differences

for light scattered by randomly separated identical particles in a large collection. On aligning to forward direction, this phase difference approaches zero regardless of particle separation. So, scattering in forward direction is coherent except for particles that are non-identical.

1.9.3 Types of scattering

Scattering of em waves can be classified into following categories as shown in Fig. 1.7. In elastic scattering process, the total kinetic energy of the system is conserved, but its direction of propagation gets modified as a result of interaction with other particles. Contrary to elastic scattering, the kinetic energy of incident light is not conserved in inelastic scattering. In this process, some of the energy of incident light gets lost or increased in output.

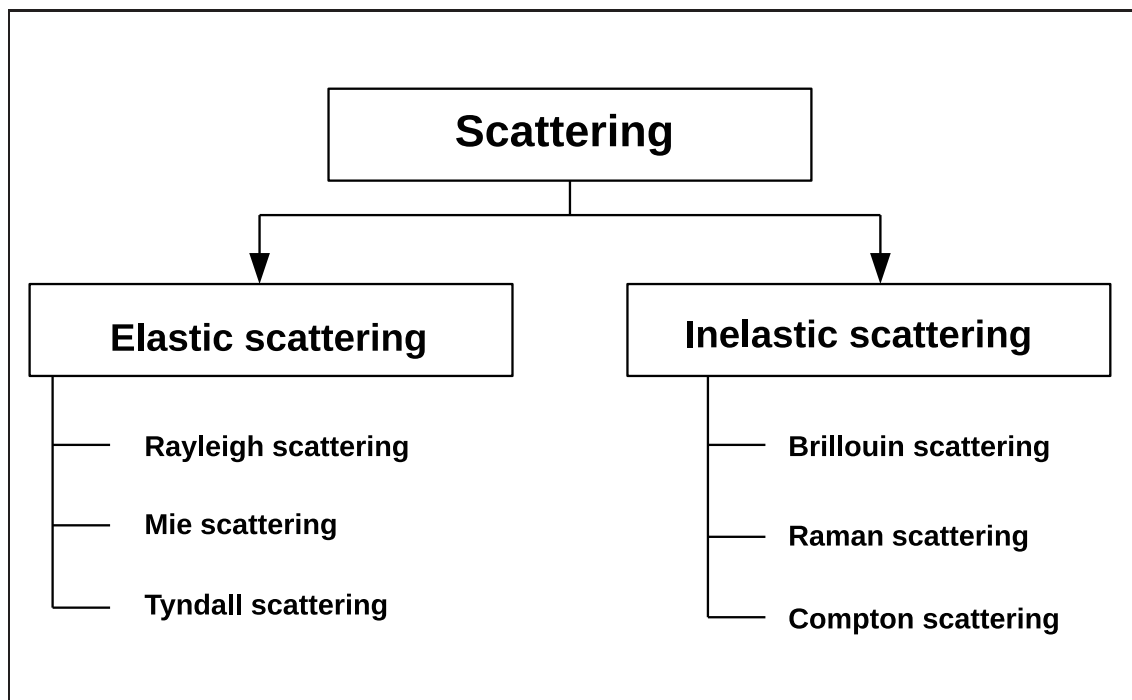


FIGURE 1.7: Sketch showing types of scattering

- **Rayleigh scattering** Light scattering by molecules/particles having size much smaller than the wavelength of incident light. Rayleigh scattering is responsible for blue colour of the sky. The size parameter of the scattering particle is given by:

$$x = \frac{2\pi r}{\lambda}$$

where r is the characteristic length (radius) of the scattering particle and λ is the wavelength of the incident light.

- **Mie scattering** Light scattering by particles of about the same size as the incident light wavelength. In the Mie regime, the shape of the scattering center becomes much more significant and the theory only applies well to spheres.
- **Tyndall scattering** This process is similar to Mie scattering, but the particle shape is not restricted to a sphere. This works best for colloidal mixtures and suspensions.
- **Brillouin scattering** Light scattered by interaction with acoustic phonons in solids and with elastic waves in liquids. Contrary to Rayleigh scattering, in Brillouin inelastic scattering, the energy is shifted from the Rayleigh line frequency by the amount corresponding to the energy of the elastic wave or phonon, occurring on higher and lower energy side of the Rayleigh line, which might be associated with the creation and annihilation of a phonon [70].
- **Raman scattering** Another inelastic form of light scattering, where light scatters by interaction with optical phonons. This type of scattering is used to determine chemical composition and molecular structure [71].
- **Compton scattering** This type of scattering occurs when light is scattered by a charged particle, usually an electron, leading to a decrease in energy of the incident photon. Remaining part of the energy is transferred to the recoiling electron.

1.9.4 Interstellar absorption

The dust in interstellar space absorbs light from stars and other background objects. Along with continuous absorption, there are also diffuse interstellar bands and atomic absorption lines like H and K lines of Calcium and D lines of Sodium.

Interstellar absorption is a component of interstellar extinction, also including the effects of scattering from dust grains.

So, if we have dust grains with cross-section ' σ ' spread over a length 'L', then the intensity of light after passing this region would be:

$$I_{out} = I_{in}e^{-N\sigma L}$$

where, I_{in} is the incidence light intensity and N is the number density of dust grains.

Converting this to magnitudes, one would get,

$$A = m_{out} - m_{in} = 1.086N\sigma L$$

where, m_{out} and m_{in} are the before and after absorption magnitudes respectively. And, the interstellar extinction is denoted by A, the difference of magnitudes.

1.9.5 Extinction and reddening

If one or more particles are placed in a beam of em radiation, then the rate at which em energy is received by detector D downstream from the particles is denoted by U. If, however, particles are removed, the power received is U_0 , where $U_0 > U$.

Extinction depends on chemical composition of particles, their size, shape, orientation, surrounding medium, number of particles and polarization state and frequency of incident beam. So, the presence of particles in the path results in **extinction** of the incident beam. If the medium in which particles are embedded is non-absorbing in itself, the difference ($U_0 - U$) is accounted for by absorption in the particles and scattering by the particles.

Dust grains in the interstellar medium have approximately power law size distribution. Light coming from distant objects is strongly absorbed and scattered by the dust, essentially removing it from the light reaching us and making the objects appear redder than they really are (see Fig. 1.8). This is known as **interstellar reddening** and is inversely proportional to the wavelength of optical

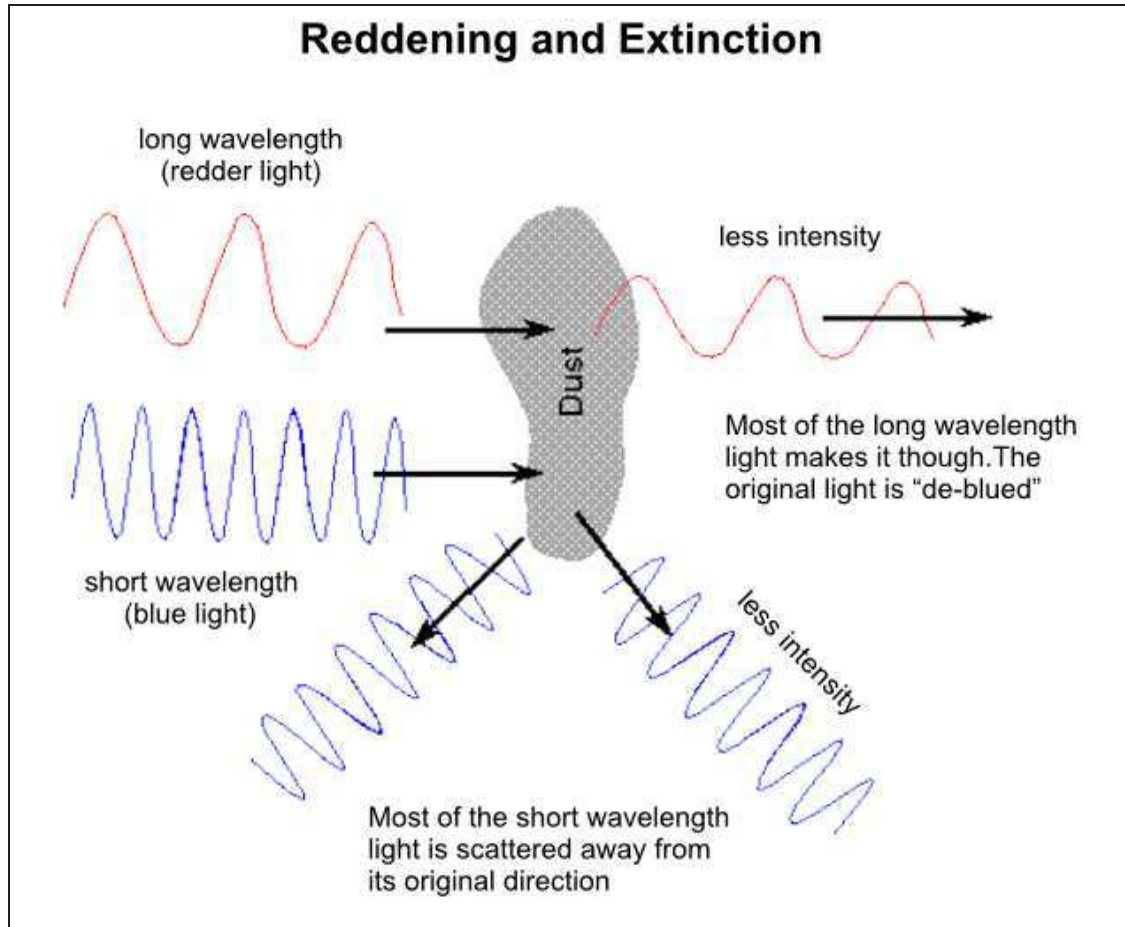


FIGURE 1.8: Diagram showing effect of reddening and extinction

light. So shorter wavelengths (blue) are more heavily reddened than longer (red) wavelengths. Reddening is measured as the difference between colour index $(B-V)$ and true colour index $(B-V)_0$ of the object through the equation:

$$E(B - V) = (B - V) - (B - V)_0$$

Interstellar dust extinction was first inferred from obscuration or extinction of star light [72]. Extinction is wavelength dependent quantity, often referred to as reddening, since it is found to be greater in blue than in red. The wavelength dependence further constrains the grain size distribution and spectral features reveal the chemical composition. Since both interstellar reddening and extinction are linked to interaction of starlight with dust grains, it is expected that the more dust along the line of sight, the more pronounced the reddening and the higher the extinction. Thus, visual extinction (A_V) can be related to reddening $(E(B-V))$ by the equation:

$$A_V = 3.2E(B - V)$$

Extinction of starlight can be related to the hydrogen column density in the line of sight, assuming a certain value for gas to dust mass ratio. The ratio is taken as 100 : 1 for Milky Way galaxy. Such ratio gives an indication towards the high optical depth and thus high optical extinction of light coming from a young star. Thus the birth of stars in dense molecular clouds can only be observed at infrared to far-infrared wavelengths.

1.9.6 Interstellar scattering

Extinction and reddening are not due to absorption alone. Dust grains absorb and scatter light. The scattering of light by dust depends on the size, shape and chemical composition of the dust and the direction at which the light is scattered. Scattering can be observed in three general situations:

- The “diffuse galactic light” (DGL), i.e. scattering by the diffuse dust of the general incident interstellar radiation field which is strongly concentrated to the galactic plane, since the dust has a relatively small scale height;
- Reflection nebulae, with a known source of illumination (usually an B or A star, because of their favorable luminosities);
- Scattering of the general interstellar radiation field by a dark cloud, seen at high enough latitudes so that it contrasts with a relatively dark sky background.

If the illuminating star is in front of the dust cloud, the scattering angle would be large, or if, the star is embedded in the cloud, the forward scattering by the dust grains between us and the star would dominate.

1.9.7 Dust re-emission

The rise of infrared, far-infrared and sub-millimeter wavelength astronomy has given a great deal of insight into the nature of thermal emission from dust grains. It is important to note that dust grains are not blackbodies. They rather radiate as modified blackbodies with a strongly wavelength dependent emissivity. Some of the incident photons are absorbed by the grain and cause it to heat up. The hot grain re-radiates this energy as thermal continuum radiation at far-IR wavelengths.

A grain hit by a photon can leave that grain in an excited state, with a probability of $\sim 10^7$ per second for spontaneous re-emission. Complex molecules making up grains have many excited states, and can quickly (10^{-12} sec) redistribute that energy into internal vibrational states, heating the grain. Since the product of the spontaneous emission probability and vibrational redistribution timescale is 10^{-5} , it is expected that most photon absorptions will efficiently heat the grain. Once heated, grains can cool down in a number of ways:

- Emit a thermal photon
- Collide with cold atoms or molecules
- Ejection (sublimation) of atoms or molecules from the surface of the grain

Under most ISM conditions, radiative cooling is expected to dominate and setup equilibrium. However, the case is slightly different for very small grains, where the absorption of a single photon can lead to a temperature spike. Therefore, it is not easy to maintain thermal equilibrium in such very small grains, further making their treatment difficult.

1.9.8 Light polarization

In case of scattering by single particle or a collection of identical particles (identical in size, shape, composition and orientation relative to incident beam), the scattered light is completely polarized if the incident light is 100 percent polarized. This implies that scattering by single or collection of identical particles does not decrease the degree of polarization of a 100 percent polarized beam, but the nature of polarization will be changed, i.e. linearly polarized light will be changed

to elliptically polarized light upon scattering. In case of non-identical particles, the scattered light will be depolarized, in other words, polarization will be reduced by some factor.

Light reaching us from the reddened stars is often linearly polarized because the extinction depends on the polarization mode. The degree of polarization as a function of wavelength can be approximated by the Serkowski law, a three parameter empirical fitting function given by Serkowski [73]:

$$p(\lambda) = p_{max} \times \exp[-K(\ln(\lambda/\lambda_{max}))^2]$$

where, λ_{max} is approx. 5500 Å, and $K=1$ on typical sightlines through diffuse clouds.

Differential extinction by aligned dust grains gives rise to polarization. These aligned dust grains also produce linearly polarized infrared emission. Hildebrand et al. [74] have discussed the wavelength dependence of the measured polarization for the dense cloud cores and envelopes. The data suggest that the grain alignment is larger in warmer regions.

Chapter 2

Literature Survey

2.1 V1331 Cyg, The special one

V1331 Cyg (RA=21:01:09.210, Dec=+50:21:44.77(J2000)), located at the border of dark cloud LDN 981, has been mentioned in SIMBAD [75]. The first identification of the object as an H α emitting source was done by González and González [76] using a photographic plate (Fig. 2.1, a), whereas the object was first discussed in literature by Herbig [25]. Based on the nomenclature given for the Lick H α survey objects, the source was known as **LkH α 120** at that time. Herbig found the object to be a T Tauri star and also stated that LkH α 120 exhibits bright nebulosity. The first direct imaging of LkH α 120 and the shell of nebulosity around it was shown in Kuhl [77]. He found that the spectrum of the star was of advanced T Tauri type and it also exhibited P-Cygni profiles.

Mendoza V. [78, 79] discovered that LkH α 120 shows an infrared excess and in the same year, Zaitseva [80] also found that the star shows variation in its brightness, thus, giving it a variable star name **V1331 Cygni**. Based on the P-cygni type absorption features and resemblance of the stellar spectrum to that of the pre-outburst spectra of FUor V1057 Cygni, V1331 Cyg was declared as a pre-outburst FUor star by Welin [81].

Penston and Keavey [82] studied the stellar spectra for V1331 Cyg and the circumstellar envelope. They found the central source to be cool (between 4000 to 7500 K), with a hot chromosphere (10000 K), through which the star is losing mass, producing P-Cygni emission profiles of Balmer and Calcium [H & K]. A distance

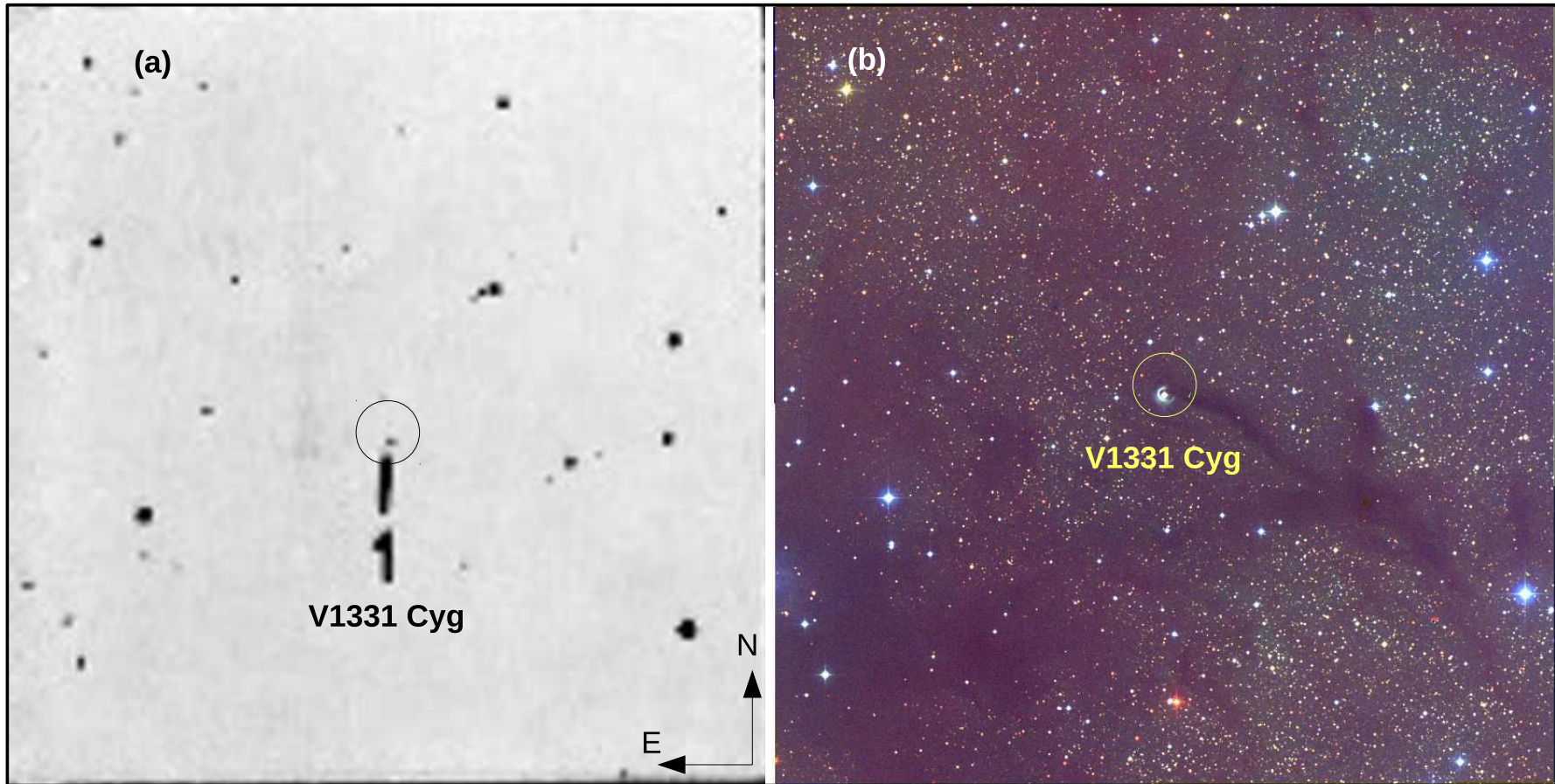


FIGURE 2.1: (a) Photographic plate image of V1331 Cyg, (b) DSS2 colour image of the object shown for comparison.

of about 700 pc to V1331 Cyg was suggested by Chavarria [83]. He also explained V1331 Cyg properties by assigning the following values to its parameters:

Visual extinction: $A_V \simeq 2.4$

Temperature: $T_* \simeq 7350$ K

Mass: $M_* \simeq 3 M_\odot$

Luminosity: $L_* \simeq 86 L_\odot$

Radius: $R_* \simeq 5 R_\odot$

Mass accretion rate: $7e^{-8} \leq \dot{M} \leq 3e^{-6} M_\odot \text{ yr}^{-1}$

Circumstellar extinction (Balmer continuum excess in magnitude): $\Delta D_B \simeq 0.2$

UBV photometry of V1331 Cyg was done by Kolotilov [84]. Schulte-Ladbeck [85] did a polarization study of the star and concluded that V1331 Cyg is not a likely candidate for detection of orbiting protoplanetary material. Levreault [86] performed a detailed study of outflows of young stars and found V1331 Cyg to be one of the outflow sources in the survey. He also estimated the mass loss rate of the outflow to be about $1.0 \times 10^{-7} M_\odot \text{ yr}^{-1}$. The distance to V1331 Cyg was later updated to 550 parsec by Shevchenko et al. [87].

Cao and Zhang [88] examined V1331 Cyg spectra and estimated Raman scattering cross-section and the line intensities. CO synthesis maps of McMudroch et al. [89] provided evidence on the presence of a massive $0.5 M_\odot$ disk surrounded by a flattened gaseous envelope, around the star. The detected ambient CO emission was modelled by a radially expanding gas ring, with a velocity of about 22 ± 4 km s⁻¹. This CO ring became the underlying basis for the proposed hypotheses on dust arcs expansion and particle separation (detailed in Section 2.2). Mundt and Eisloffel [90] found the star to be associated with HH objects and jet. They suggested a total spatial extent of approximately one parsec for the bipolar outflow. Hojaev [91] suggested a fountain shape for the reflection nebula surrounding V1331 Cyg and claimed the nebula to be originating from the star itself.

Based on HST imaging, Quanz et al. [92] showed that the star has two nested rings of 9000 and 3300 au radii, respectively. They also claimed that the incomplete outer dust ring section to the northwest is caused by the dark cloud LDN 981 sitting in the foreground. An additional dust arc was also seen in the southwest direction. K band spectroscopy of V1331 Cyg was done by Najita et al. [93]. They detected strong emission from CO and hot water vapor and suggested the emission to be originating in the circumstellar disk. Kitamura et al. [94] observed V1331

Cyg in the H band with CIAO instrument on the Subaru telescope with an aim of direct detection of disk. They found an arc much closer to the central source than the already known inner ring. They claimed this arc to be the direct evidence for the scattered light from the still unresolved disk and suggested an inclination angle of about 30° of the disk.

Based on high resolution infrared spectroscopy of OH and H₂O, Doppmann et al. [95] suggested an almost pole-on view to V1331 Cyg. Kóspál [96] through millimeter interferometric observations, detected strong ¹³CO(1-0) emission from a compact circumstellar envelope surrounding V1331 Cyg.

Using Herschel imaging and spectroscopy, Green et al. [97] produced Spectral Energy Distribution (SED) of V1331 Cyg. Petrov and Babina [98], using photospheric lines of the star, estimated the radial velocity of V1331 Cyg to be $-15 \pm 0.3 \text{ km s}^{-1}$. They also calculated the maximum velocity of the stellar wind around 400 km s^{-1} . This was a rare case when such lines were seen from a YSO. In another work, Petrov et al. [99] showed that V1331 Cyg has high velocity absorption lines of metals (Fe II 5018, Mg I 5183, K I 7699), which form in post-shock gas in the jet, again suggesting that the star is seen through its jet. The probability of detecting an almost pole-on YSO with an inclination less than or equal to 5° is less than 1%. This means, on an average, **only one** among a hundred YSOs detected, has such an inclination. Furthermore, in case of inclination less than 2° , the probability further reduces, with only one among a thousand stars having such small inclination. This makes V1331 Cyg indeed special.

2.2 Research motivation

The current knowledge about V1331 Cyg so far does not provide a clear picture on the origin of dust arcs as they are seen today. They could be a result of ejections from a FUor outburst in the past, or instead, as a result of pole-on view, we might be seeing scattered light from the remnants of the outflow cavity. In any case, we only see the projection of a three-dimensional structure as an arc. For any of the two scenarios to be valid, just like the expanding CO ring, the dust arcs should expand as well, as they move away from the central star.

Since I had two epochs of V1331 Cyg HST observations, one goal was to measure the inner and outer arcs radial expansion by comparing the two epochs of

data. Since the dust scattering wavelength depends on grain size, a radial gradient in particle size would imprint itself as a colour index gradient. As the expanding CO ring lies farther outwards than the outer dust arc, the particle separation hypothesis implies that CO molecules will reach terminal velocity earlier than the dust grains. This would mean that the dust arc is devoid of molecular gas and CO ring is devoid of dust. Another research goal was thus to do outer dust arc colour analysis in order to check the plausibility of particle separation hypothesis.

In addition, I used UKIDSS, SPITZER, TLS, SUBARU and HERSCHEL data along with recent observations conducted with PdBI and SMA for V1331 Cyg, to investigate the circumstellar environment of the source.

Chapter 3

Telescopes and Observations

3.1 The Hubble Space Telescope

The first large aperture non-military telescope to be placed in space was HST. The concept behind this space telescope was to overcome distortions caused by Earth's atmosphere and provide unprecedented spatial resolution with a large mirror. Hubble's primary mirror has a size of 2.4 meter in diameter. It is a Cassegrain reflector telescope orbiting earth at a speed of around 8 km s^{-1} . Light falls on to the primary mirror from where it is reflected to the secondary mirror. Secondary focuses the light through a hole in the center of primary, leading it to telescope's science instruments. Currently there are six instruments aboard HST, each of which studies the universe in a different way.

One of the instruments which was previously aboard HST, from 1993 to 2009 is Wide Field Planetary Camera-2 (WFPC2). The instrument layout is shown in Fig. 3.1, with the technical details listed in Table 3.1.

TABLE 3.1: HST WFPC2 camera specifications

Camera	Pixel & CCD format	FOV	Pixel scale	F/ratio
Wide Field	$800 \times 800 \times 3$ CCDs	$2.5' \times 2.5'$ (L shaped)	0.1"	12.9
Planetary	$800 \times 800 \times 1$ CCD	$35'' \times 35''$	0.046"	28.3

Handbook on WFPC2 by Heyer and Biretta [100] describes the instrument specifications further in detail.

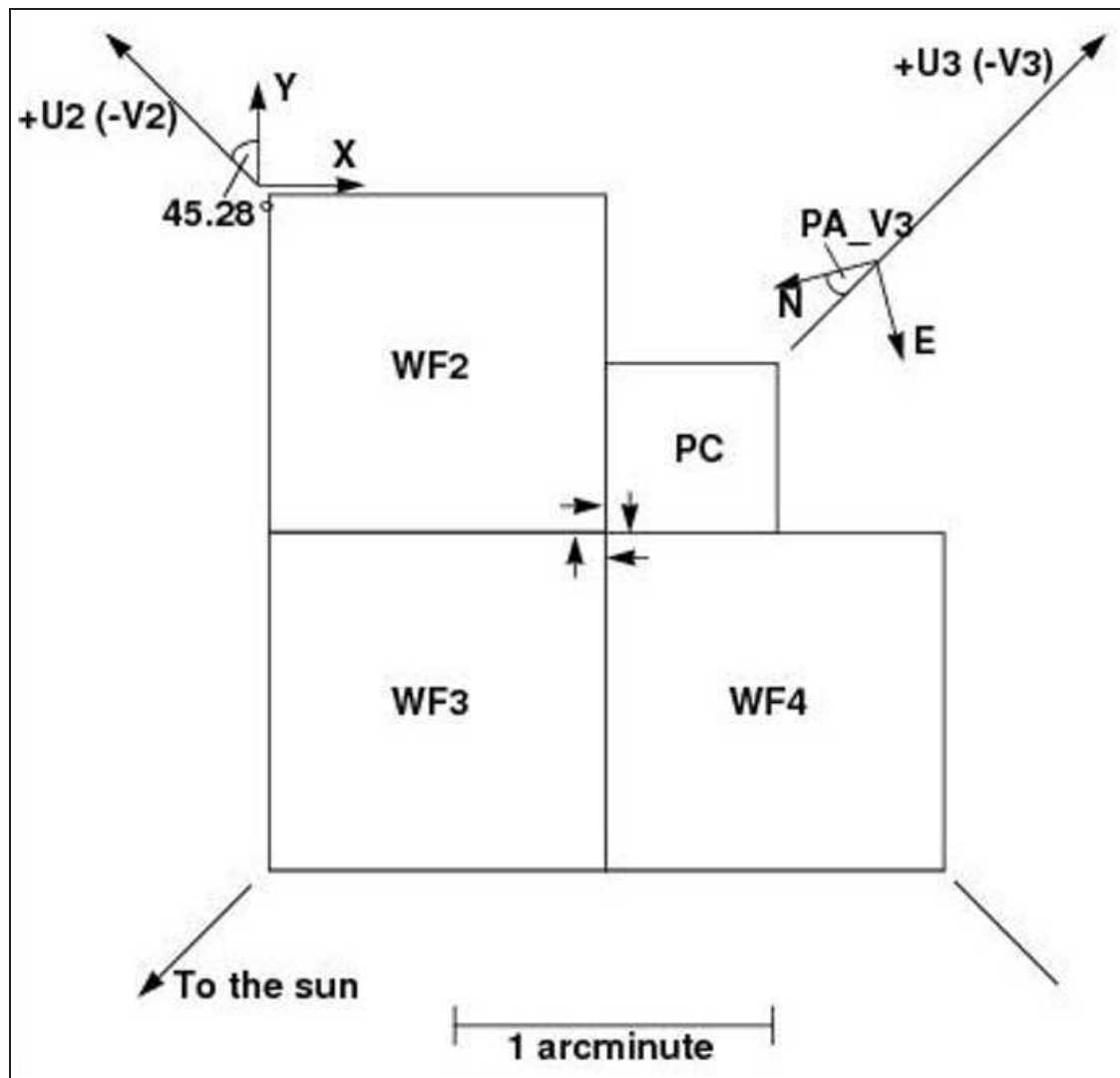


FIGURE 3.1: WFPC2 field of view projected on the sky. The U2, U3 axes (same as the -V2, -V3 axes) are defined by the nominal Optical Telescope Assembly (OTA) axis, which was near the center of the WFPC2 Field of view.

3.1.1 Observations with HST

With a time gap of almost 10 years, V1331 Cyg was observed twice with the WFPC2 camera of the HST. The first epoch data was taken by Dr. Stapelfeldt in 2000, while the second epoch was observed by Dr. Stecklum in 2009. Details of the observations done are summarized in Table 3.2.

I downloaded the HST pipeline products from MAST archive. Frames from both epochs were already bias, drizzle and flatfield corrected.

TABLE 3.2: V1331 Cyg observations with HST-WFPC2

Data Set	Filter	Exposures	Instrument
1st epoch(2000)	F606W	3 exposures for 10,230,230 s each	PC,WF3
	F814W	2 exposures for 10, 100 s each	PC
2nd epoch(2009)	F450W	4 exposures for 7,7,2300,2300 s each	WF3
	F606W	3 exposures for 3,1100,1100 s each	WF3
	F814W	3 exposures for 3,1100,1100 s each	WF3

The HST planetary camera (PC) image of F814W filter from first epoch was cleaned and provided by Dr. Stapelfeldt. For this purpose, he searched the HST archive for F814W images of stars which match V1331 Cyg in both brightness and colour. Using an appropriate tweaking factor, the images were subtracted so as to get the best possible PSF subtraction for V1331 Cyg.

3.2 Data from UKIDSS

United Kingdom Infrared Telescope (UKIRT) is the largest infrared telescope in the northern hemisphere. The 3.8 meter telescope is located on Hawaii's Mauna Kea. Infrared, JHK band images of V1331 Cyg were retrieved from the UKIDSS (UKIRT Infrared Deep Sky Survey) performed at UKIRT. The UKIDSS project is defined in Lawrence et al. [101]. UKIDSS uses the UKIRT Wide Field Camera (WFCAM) [102]. The photometric system is described in Hewett et al. [103], and the calibration is described in Hodgkin et al. [104]. The pipeline processing and science archive are described in Hambly et al. [105]. The survey instrument WFCAM has four 2048×2048 Rockwell devices at 94% spacing. Pixel scale of $0.''4$ gives an exposed solid angle of 0.21 sq.degrees, but after applying microstepping, the pixel scale reduces to $0.''2$ only. Observation details are given in Table 3.3.

TABLE 3.3: V1331 Cyg observations with UKIDSS in 2010

Broadband filter	Mean $\lambda(\mu\text{m})$	Exposure time(s)	Field of view	Instrument
J	1.25	10	$\sim 27' \times 27'$	WFCAM
H	1.63	10	$\sim 27' \times 27'$	WFCAM
K	2.2	5	$\sim 27' \times 27'$	WFCAM

3.3 Alfred Jensch Telescope-TLS

Thüringer Landessternwarte Tautenburg (TLS) has a 2 meter Zeiss telescope that can be run in three different configurations :

- Schmidt telescope
- Quasi-Cassegrain telescope
- Coudé telescope

The TLS Schmidt telescope is the largest of its kind in the world. The description of the instrument is given in Table 3.4.

TABLE 3.4: Properties of the Schmidt telescope at TLS

Property	Value
Diameter of the primary	2 meter
Diameter of corrector plate	1.34 meter
Focal length	4 meter
Field of view	3.3×3.3 sq. degrees
Scale	51.4 arcsec mm^{-1}

3.3.1 TLS observations for bipolar outflow and HHO

Optical imaging of V1331 Cyg was done in April 2003 and November 2011, by Dr. Stecklum. It was done using the 2-m Tautenburg telescope in its Schmidt configuration, offering a free aperture of 1.34-m. Both times, I, H α , and [SII] filters were used. Using customized IDL¹ routines, the images were corrected for flat field variations and bad pixels. Then, the data was astrometrically calibrated using astrometry.net code [106]. For all three filters, the images were registered and stacked by Dr. Stecklum, resulting in final images with integration times of 12, 80 and 100 minutes respectively. The final images were provided to me.

Herbig Haro objects spectroscopy was done with Nasmyth spectrograph at the TLS. The southern and northern HHOs spectra were obtained with a total integration time of 9600 and 6000 seconds, respectively. Data were collected for

¹IDL is a trademark of Exelis VIS.

two nights in July, 2013 by Dr. Stecklum and me. Accounting for the change of the projected Earth velocity towards the target, the two observations were added together, and data processing was done similarly on both northern and southern HHO. Wavelength calibration was done using spectral lines originating from airglow in the upper atmosphere. A dispersion relation was established to convert pixel coordinates into wavelength. An initial estimate of the sky lines was taken, which was improved in order to fit to the actual lines by a least-square minimization. Applying optimal extraction technique provided the spectrum.

3.4 Spitzer data

The Spitzer space telescope has three focal plane instruments. One of the three instruments is IRAC (Infrared array camera). IRAC is a four channel (3.6, 4.5, 5.8, 8 microns) camera and provides simultaneous 5.12×5.12 arcmin images at all four wavelengths. Pixel size is 1.2 arcsec in all bands. Each detector array is 256×256 pixels in size. The two short wavelength channels use InSb detectors, whereas, the two longer wavelength channels use detectors specially treated with GaAs. The instrument description is detailed in Fazio et al. [107].

For V1331 Cyg, observations with AORKEY 27067904 (principal investigator Tim Spuck) were performed on July 18, 2008, with each individual frame having an exposure time of 10.4 seconds. A total time of about 200 seconds per filter per mosaic image was further invested. I downloaded Spitzer IRAC images in all four bands from infrared science archive (IRSA).

3.5 Subaru archival data

V1331 Cyg observations were done at the SUBARU telescope's CIAO (Coronagraphic Imager with Adaptive Optics) instrument [108] in November 2005, in the H band using coronagraphic mask of 0."8 diameter. Kitamura et al. [94] originally discovered the inner arc like feature (farther inwards than the previously known inner dust ring), but could not reveal any further details much closer to the star. To re-process the CIAO images, the data (courtesy M. Tamura) and the images for PSF reference star SAO 33066 were retrieved from the SMOKA archive [109].

The total on-target integration time is 600 seconds and the pixel scale is $0.''0217$. Small dithering shift of $1.''5$ between the two sets of target images precluded a proper sky subtraction because of image superposition. The coronagraphic mask has a transmission of 2% which permits to track the position of the image peak.

By correlating the images within the mask, shifts were derived at the sub-pixel level, and applied to register the individual frames of both target and reference before stacking them. Applying shift-and-add technique, Strehl ratio increased by about 3%. The shifts were also propagated to generate corresponding overall coronagraphic masks which were eventually combined, yielding a final mask of $0.''9$ diameter. Before establishing the final image, the PSF image was rotated by 6 degrees to match the spider orientation of the target image. Both images were then registered and subtracted, taking the measured flux ratio into account. This ratio was slightly tweaked, leading to a weak over-subtraction, to make sure that only features with real flux-excess remain. Flux calibration is based on the total flux of the target, taking attenuation of the stellar core by the coronagraphic mask into account, and the 2MASS H magnitude of 9.2.

3.6 Herschel/PACS observations

V1331 Cyg was observed with the HERSCHEL spacecraft [110] within the open-time project OT1_JGREEN02_2 (refer to Green et al. [97]). The observations took place on July 22, 2011 (operational day 800) using the bolometer cameras of PACS (Photoconductor Array Camera and Spectrometer) [111] under the observational IDs 1342225252-55. The PACS prime mode was employed with a nominal scanning velocity of $20''$ per second. Images were taken in all three filters (70, 100 and 160 micron) in the mini-map mode and resulted in maps with roughly 3.5 arcmin useful field-of-view. For the 160 micron data, in the middle of the combined map, roughly 160 seconds of dwell time were accumulated per pixel map. For the other two filters, it was half of that. The HERSCHEL archive (HSA) downloaded data was re-calibrated and provided by Dr. Hendrik Linz (MPIA). These were retrieved from the presently running bulk processing with the SPG (Scientific Product Generation) 13.0 software version. The pointing products of this new edition of the data include the newly developed data reduction step CALCAT-TITUDE: a correction of the frames pointing product based on the HERSCHEL

gyroscope house-keeping (refer to Sánchez-Portal et al. [112]). It improves the absolute pointing accuracy and also mitigates the pointing jitter effect on individual frames. Using the gyro corrected frames, destripping and removal of $1/f$ noise using JSCANAM within HIPE (HERSCHEL Interactive Processing Environment) version 13.0 b5130 was done. For individual detector pixel distortion correction and the final mapping, the implementation of the Drizzle algorithm [113] within HIPE called PHOTPROJECT was utilized which allows to experiment with different pixel fractions.

Reference point spread functions (PSFs) were taken from the PSF tarball provided by the PACS instrument team². For further analysis, these were rotated by $\approx 13.8^\circ$ counterclockwise in order to agree with the orientation of the PACS PSF during the V1331 Cyg observations.

3.7 Plateau de Bure Interferometer (PdBI) observations

At an altitude of 2560 m, the IRAM-Plateau de Bure Interferometer (PdBI) is located in the south of the French Alps. It consists of six antennas, each of which is a Cassegrain telescope having a diameter of 15 m each. The antennas can be moved along a 'T' shaped track, the length of which is 368 m in north-south direction and 760 m in the east-west direction. Detailed description of the interferometer is given in Winters and Neri [114].

The PdBI observations for V1331 Cyg were conducted between January and March, 2014 under the program ID X06E. In order to achieve high angular resolution and sensitivity, broadband continuum emission at 1.3 mm and $^{12}\text{CO}(2-1)$ emission were observed simultaneously in a very extended (A+B) configuration. One spectral unit of the narrow band correlator in each polarization was tuned to $^{12}\text{CO}(2-1)$ line at 230.538 GHz. Line measurements were done using total bandwidth of 40 MHz with individual channel spacings of 78 KHz. The remaining frequency windows of the correlator were combined to observe the continuum emission with a total bandwidth of 1.92 GHz between 229.5 GHz and 231.5 GHz. Wide-band correlator WideX were used in parallel to increase the sensitivity of the continuum measurements.

²ftp://ftp.sciops.esa.int/pub/hsc-calibration/PACS/PSF/PACSPSF_PICC-ME-TN-033_v2.0.tar.gz

3.8 Submillimeter array (SMA) data

The submillimeter array (SMA) is a radio interferometer performing high spatial and spectral resolution imaging on Mauna Kea in Hawaii. Comprised of eight 6 meter antennas, SMA operates at frequencies from 180 GHz to 700 GHz. The eight antennas can be adjusted into different configurations and can have baselines as long as 509 m. Current usage of SMA is done in studying protoplanetary disks, evolved star envelopes, star forming regions, among others. Detailed description of the instrument is given in Ho et al. [115].

SMA observations were carried out on May 21, 2014 in service mode under the experiment code 2013B-H003. The observations were conducted after a first track, at frequency of 230 GHz. The antennas were arranged in a compact array and shared the passband calibrator 3c279. Along with V1331 Cyg, additional objects observed were 3c418 and mwc349a as phase calibrators, Titan as flux calibrator and 3c454.3 as bandpass calibrator. Because of time sharing, the correlator setup used 128 channels for all chunks in the bandpass, thus, providing moderate spectral resolution.

Chapter 4

Data reduction and analysis

With the primary aim to analyse the HST data on V1331 Cyg, the research project was funded by the German Aerospace Center (DLR). I was then entitled to use the results obtained in the project, for my PhD. However, I have tried to incorporate archival and new data to achieve an understanding and description of V1331 Cyg as complete as possible.

The chapter gives the description of tools and techniques used in data reduction and image processing. V1331 Cyg observations from various different telescopes and instruments were used to study the young star and its surroundings in detail. The different methods of data processing for various telescope instruments and their respective data sets have been elaborated for reasons of transparency and reproducibility of my study.

4.1 HST image cleaning

Bias subtraction, dark current removal and flat fielding corrections are already done in the pipeline of HST WFPC2 data archive. So the only thing left to be done was to remove the cosmic rays and bad pixels.

4.1.1 Cosmic Rays and bad pixels

Cosmic rays (CR) are extremely high energy protons and atomic nuclei. They originate mainly outside the solar system. CRs are a very common type of noise

in HST images. The low brightness CR features look like faint stars. Getting rid of these false stars is necessary before analyzing the data. Since the CRs can hit the CCD at any random pixel, these are sharp features whose position varies in different exposures of the same field. Bad pixels are the pixels showing false signal over a certain stretch. The effect looks like a streak of light going through the CCD, which is not real. It could result from a very bright CR event which stretches over a number of adjacent pixels. Figure 4.1(a) shows the V1331 Cyg image having these two effects.

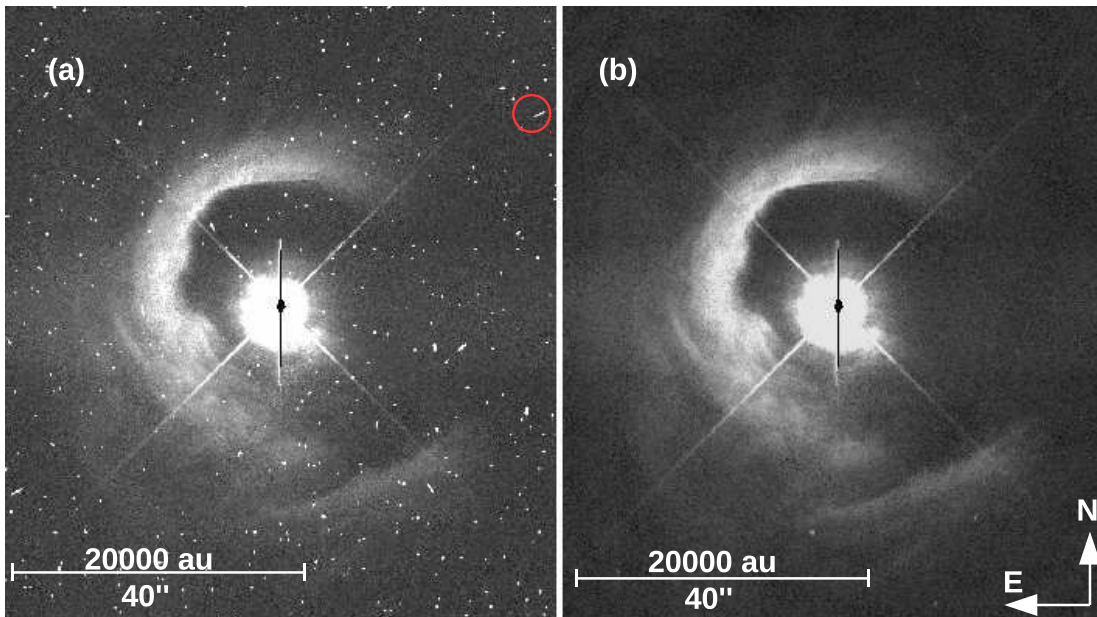


FIGURE 4.1: (a) First epoch F606W filter image effected by many cosmic rays (seen as sharp single pixel entities), bad pixel circled in red. (b) Cleaned image.

The IRAF (Image Reduction and Analysis Facility) software package was used to clean images of bad pixels and cosmic rays defects. Firstly, I roughly cleaned the cosmic rays from each individual frame in both epochs using **cosmicrays** task. It can be found in *noao.imred.crutil* package of IRAF. The task searches for cosmicrays using selection criteria given by parameters *threshold* and *fluxratio*. The value of threshold was set to five or more times the standard deviation of the background to identify the deviant pixels. The task when executed opened an interactive session (see Fig. 4.2), which helped to distinguish between real and fake stars. The CRs were then replaced by taking mean of four neighboring pixels (excluding the brightest neighbour, after background subtraction). For details on cleaning images using IRAF, refer to Wells and Bell [116] manual.

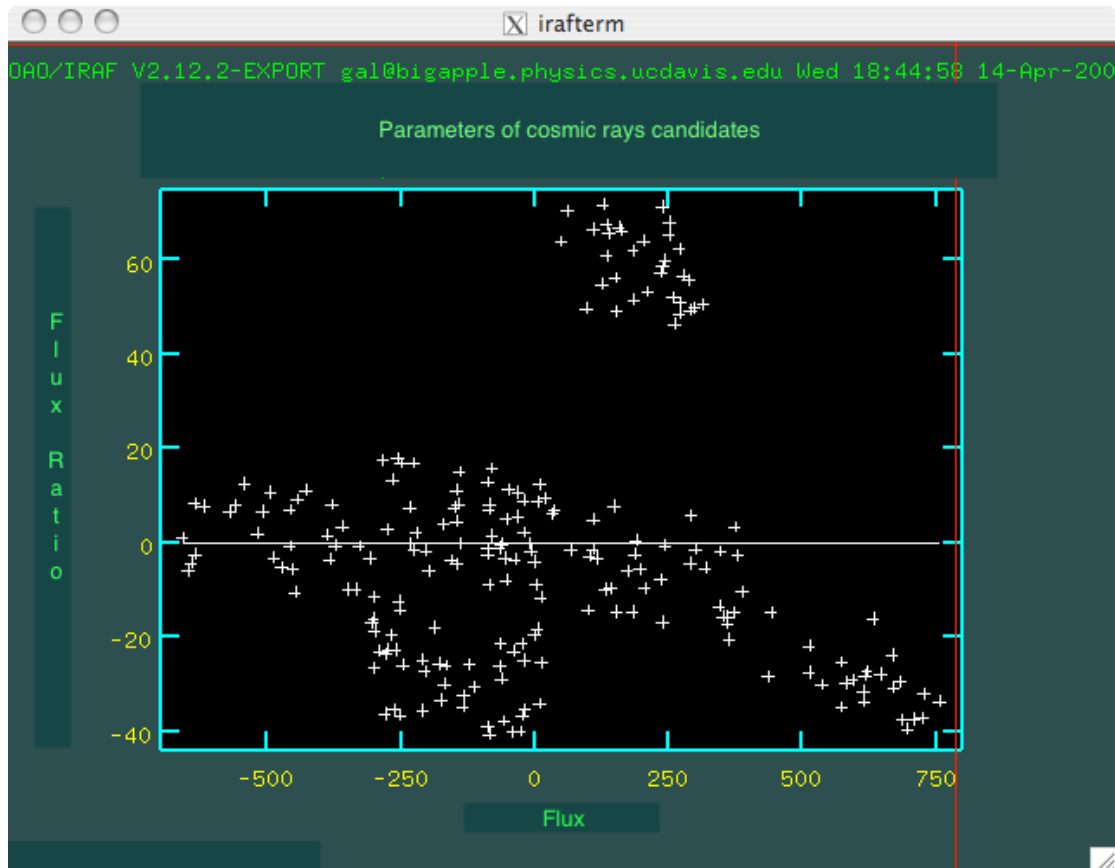


FIGURE 4.2: An example interactive window showing the stars along with the cosmic rays plotted. The white horizontal line gives the demarcation between the good and bad pixels.

Secondly, choosing two frames from the 1st epoch of F606W filter having same exposure time, I combined them using IRAF `imcombine` task. By setting the `reject` parameter to `crreject` in the `imcombine` task, I could set the readnoise level to 0.71 for the gain value of 7 (as given in the image header). Another parameter `Hsigma` was set as the ratio of standard deviation to five times the background noise. Executing this task resulted in a combined image free of both the bad pixels and CR defects, as shown in Fig. 4.1(b). The principle behind this is, since the position of these defects in two different frames is not the same, they can easily be neglected when two frames are compared and combined. The same approach was implemented with F450W and F814W filter images in both epochs and defects removed.

4.2 WF3 background correction

The background light values were found varying differently on Wide field camera detectors 3 and 4. To correct this effect, I wrote an IDL script (refer to Appendix B, section B.1), in which the azimuthal median values were calculated from the boundary between third and fourth quadrant. Difference of these values was smoothed and multiplied by a tweaking factor of 0.75 (for best visual appearance) and then added to the original third quadrant values. Keeping in mind the saturated central star, the zero value pixels were restored.

4.3 PSF subtraction for V1331 Cyg

Subtracting the Point Spread Function (PSF) accurately was a necessity to study the circumstellar nebulosity around otherwise saturated V1331 Cyg. Also this step helped in studying faint features very close to the star. For this task, I used Tiny Tim standalone application [117]. This application generates model PSF suitable to the source spectrum provided. The input spectrum of V1331 Cyg to Tiny Tim was obtained from Vizier photometry viewer [118]. Input fluxes converted to Jansky are listed in Table 4.1.

TABLE 4.1: V1331 Cyg spectrum input to Tiny Tim

Wavelength (Angstrom)	Flux (Jansky)
3650	0.008507
4450	0.027675
5510	0.063083
6580	0.115205
8060	0.181836

I executed Tiny Tim and used the following parameters. The values input are written side by side and the output model PSF is shown in Figure 4.3.

Camera : WFPC-2

Chip : 3

Pixel location (x,y) : 365,380 (1st epoch) ; 363,373 (2nd epoch)

Filter : F606W

Spectrum of choice : 5 (input spectrum of V1331 Cyg)

Diameter of PSF : 12"

Oversampling : factor of 5 ; this generated a [600,600] pixel image PSF

Focus : 0.0

Visual extinction : 2.4

Jitter (mas) : 40

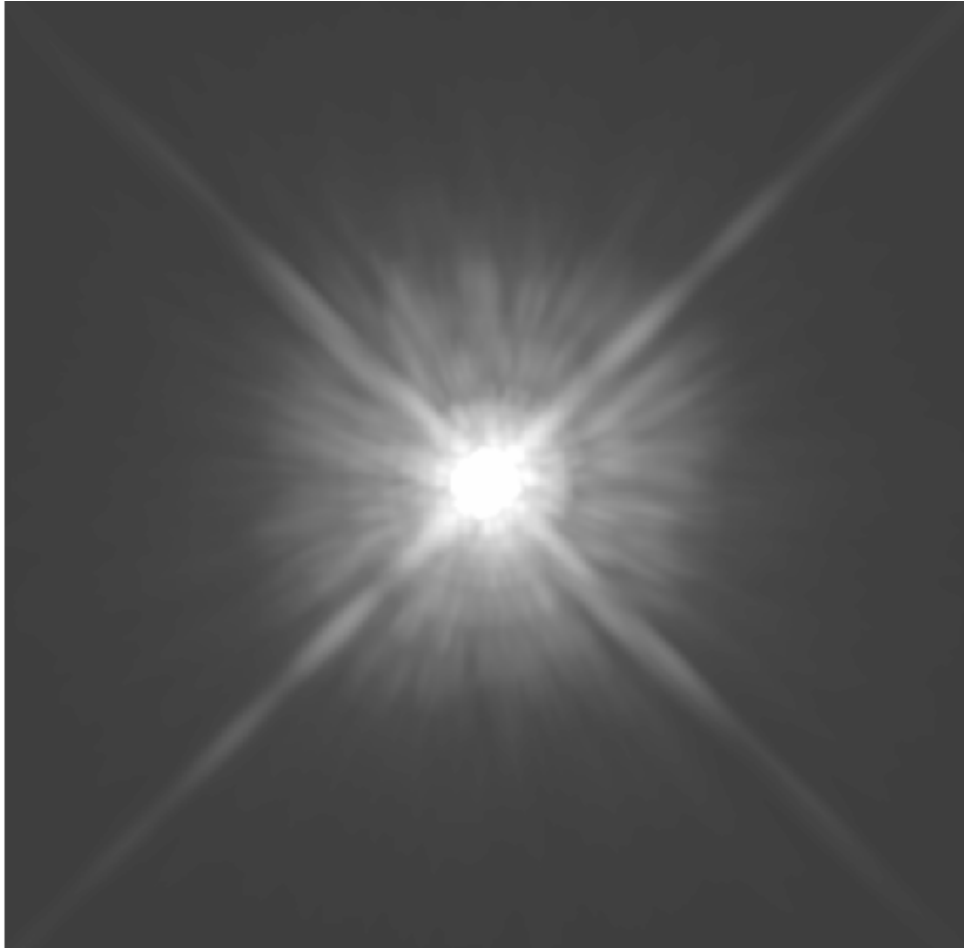


FIGURE 4.3: Model PSF generated for 1st epoch image. The PSF is [600,600] array in size.

Since the model PSFs obtained for both epochs were oversampled, I had to run the IDL routine **rebin** using nearest neighbour sampling to resample them into normally sampled images. The rebinned images were then convolved with the kernel accounting for the telescope jitter, provided in Tiny Tim manual, using IDL. I cropped a section of original images which contained saturated pixels in the stellar center. The same pixels were reflected in the convolved 1st and 2nd epoch images as well. I then subtracted the saturated model PSFs from original frames with an appropriate tweaking factor of 0.92 for 1st epoch and 0.6 for 2nd epoch.

Figure 4.4 shows the before(a) and after(b) PSF subtracted 1st epoch F606W filter images. PSF subtraction on F450W and F814W filter images was done on the same lines as for F606W filter images.

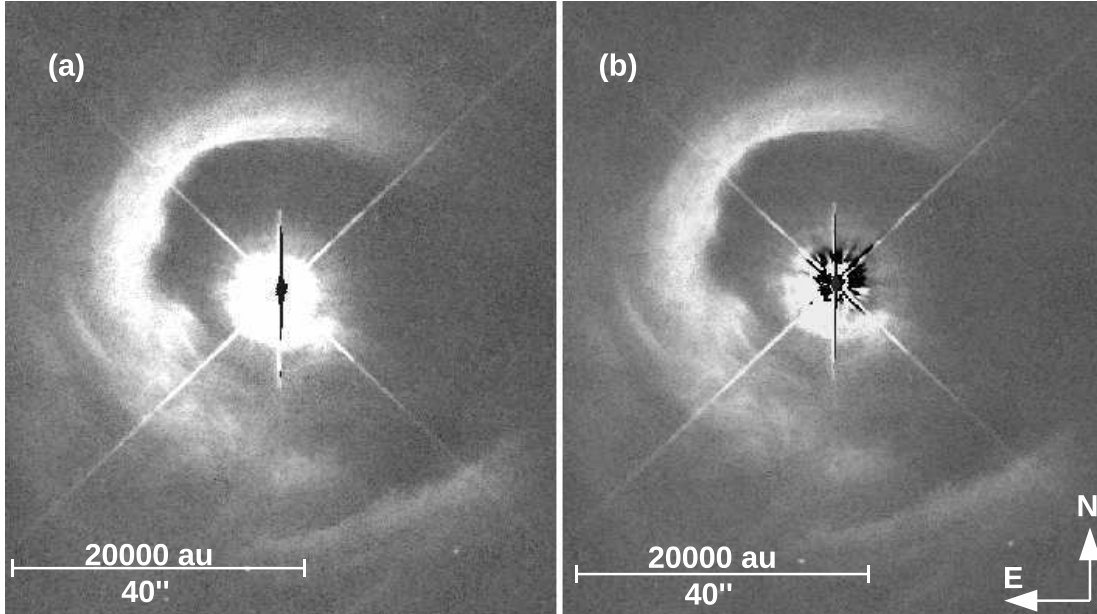


FIGURE 4.4: Before (a) and after (b) PSF subtracted first epoch F606W filter images.

4.4 Dust arcs analysis

In order to study the outer and inner arc expansion, I assumed the simplest model of radial only expansion. Since the HST images carry two dimensional information, i.e, the x and y pixel coordinates give a 2D impression of the actual three dimensional structure in the sky, I transformed the images from cartesian (x,y) to polar (r, θ) coordinates such that the 2D circular arcs take a vertical shape. The radial shift was then measured as the displacement of 'r' coordinate of the polar profiles between the two epochs. The procedures to calculate the shifts and the results obtained are detailed in the following section.

4.4.1 Outer arc

To study the outer dust arc radial profile in both epochs, F606W filter images were used because they were the **only** long exposure WF3 frames available in

both epochs. Since the frames had different sizes, I cropped them to form square arrays of the same size. Depending on the need to keep sunlight shining on the solar arrays all the time, HST thermal design allows U1 optical axis of the telescope to roll such that the sunlight always falls on same side of the telescope. For this reason, HST observations for the same target, done at different times, have different roll angles. Hence, images of V1331 Cyg from the two epochs have different orientation in CCD detector. To correct for this, I performed astrometry on 11 faint stars in the background of V1331 Cyg (see Fig. 4.5). The stars were chosen such that they were visible in both epochs. Correct (x,y) positioning of the stars in both epochs was calculated using IRAF task **center**, refer to tables 4.2 and 4.3 for details. The values were then input to an IDL script (refer to Appendix B, section B.2) which used Singular Value Decomposition (SVD) algorithm to calculate the transformation parameters to match 2nd epoch data to 1st epoch. This was done iteratively to avoid the influence of stars with substantial proper motion. In the end, 10 out of 11 initial stars (excluded star no. 3, refer to Fig. 4.5) were used to calculate the final transformation parameters. Table 4.4 lists the parameters calculated to match the two epochs.

TABLE 4.2: The table lists the (x,y) pixel positions of the stars in first epoch F606W full frame. The errors are also in pixels.

Number	x	y	error (x)	error (y)
1	738.720	1340.639	1.420	1.408
2	636.778	1153.589	2.375	2.627
3	885.457	1063.187	1.962	1.951
4	1076.045	922.141	1.779	2.129
5	1062.768	802.495	2.058	1.766
6	1094.992	711.419	1.067	1.018
7	1078.100	264.401	2.587	2.157
8	528.446	127.976	2.693	2.192
9	481.493	27.274	2.795	4.744
10	335.127	111.113	2.279	1.955
11	259.787	81.498	2.838	2.854

Second epoch image was remapped to match the first epoch pixel coordinate system by using the transformation parameters fed into an IDL script (refer to Appendix B, section B.3). The full frame images had array sizes of [1515, 1495] and [1516, 1495] for first and second epoch respectively. To save processing time taken by large image files, and also to make the images of same size, both images were cropped to smaller dimensions of [1010, 1010] array size. On comparing the

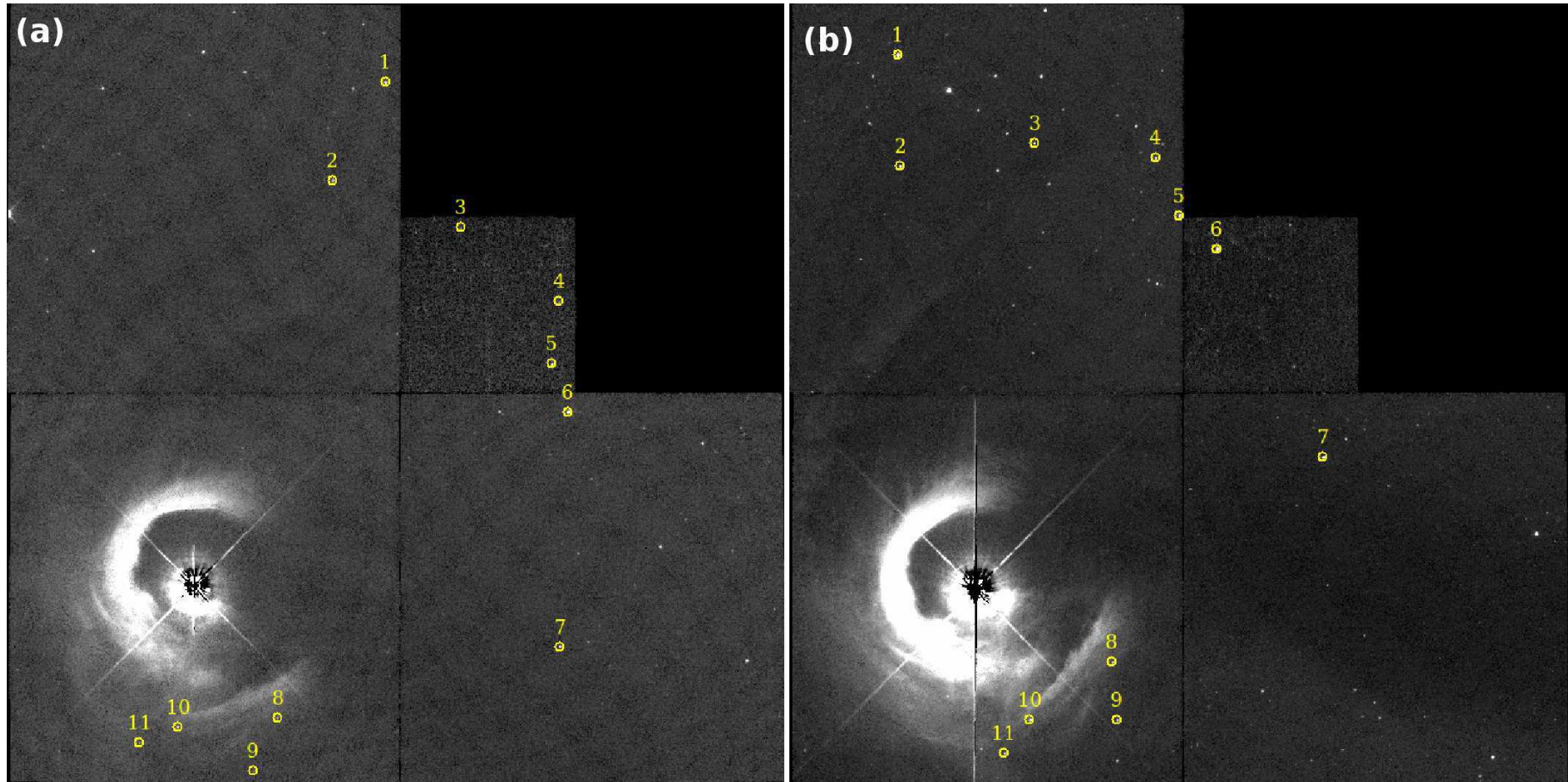


FIGURE 4.5: First epoch (a) and second epoch (b) F606W filter full frames with stars used in astrometry marked on them.

TABLE 4.3: The table lists the (x,y) pixel positions of the stars in second epoch F606W full frame. The errors are also in pixels.

Number	x	y	error (x)	error (y)
1	213.045	1393.140	1.569	1.621
2	217.193	1180.344	2.277	2.227
3	478.739	1223.717	2.458	2.982
4	713.861	1196.179	2.545	3.033
5	760.745	1086.040	1.711	2.388
6	833.557	1022.186	1.544	1.428
7	1040.589	625.556	2.120	2.000
8	630.184	235.082	3.078	2.664
9	639.424	124.546	3.010	4.238
10	470.557	124.561	2.682	2.716
11	419.905	61.777	3.807	3.365

TABLE 4.4: List of parameter values used in the remapping procedure for the outer dust arc, to map 2nd epoch image w.r.t 1st epoch image.

Parameter	Transformation value
Xshift \pm error	-135.5907 ± 0.1431
Yshift \pm error	235.4284 ± 0.1431
Rotation \pm error	0.51745 ± 0.0031
Stretch \pm error	1.00006 ± 0.0045
Reduced χ^2	0.055171

number of zero pixels between the two images, I found that the images had different number and different positioning of zero value pixels. I had to construct a zero pixel map as a combination of zero pixels at indices from both images. This map was then applied to both images such that the number and indices of zero pixels remains same in both the images. From here on, all the procedures were done exactly the same way on both epoch images. Stellar center was found as intersection of diffraction spikes. The pixel (x,y) co-ordinates for the stellar center were found to be (510.386,510.242). The images were converted from cartesian to polar co ordinates with center of star as the origin point. Since the star light was influencing the dust arc brightness, I had to subtract it from the frames. For this, I calculated the azimuthal median from the polar profiles over all radial values, starting from the center of star. These profiles had dust arc radial profiles with stellar background sitting on top of them. So, I had to remove the stellar background contribution. I did background fitting for the profiles using IDL routine **curvefit**. Obtained fitted profiles were converted back from polar to cartesian

form using stellar center. I subtracted these background fitted cartesian images from the original images. Now, the dust arcs were almost free from any contribution from V1331 Cyg but, there was still some starlight present in the center of images. I blocked the center completely using a mask with aperture size ≤ 90 . The outer dust arc is not exactly circular in shape. Also, the arc has some section missing to the northwest (NW). Hence, the outer dust arc center was approximated using shift estimate based on narrowest profile using Powell minimization [119]. The outer dust arc center was found to be $(x, y) = (507.201, 539.466)$. Again the images were converted from cartesian to polar co-ordinates, but with dust arc center as the origin. With similar approach as done with stellar background radial profiles, radial median profiles for dust arcs were calculated for both epochs. Since the NW section of the arc is missing, the median was not calculated over whole azimuthal range. The range of y values was chosen only for the part being spanned by the dust arc in the polar image, ranging from $5^\circ \dots 220^\circ$ in position angle (PA). Figure 4.7 (a) shows the dust arcs from both epochs over plotted for comparison.

Not much could be depicted just by looking at the radial plots. In order to detect amount of expansion in outer arc over a period of ten years, I had to calculate any measurable shift between radial profiles from two epochs. At first, I calculated the cross-correlation lag which indicated that the second epoch profile is 0.64 pixel further away from the arc centre. Since the method does not require any zeroing of the outer profile regions, the result turned out to be very robust against levels of oversampling, ranging from 20 to 100. The pixel shift corresponded to an average expansion velocity of 16.6 km s^{-1} . Secondly, I applied the deconvolution approach to both radial profiles. An IDL script (refer to Appendix B, section B.4) was written to oversample the profiles by a factor of 100 which used first epoch profile as the deconvolution kernel. Shift was calculated using IDL routine **maxlikelihood**. The initial application to the full profiles yielded a large shift because deconvolution is sensitive against differences in the outer regions of the profiles. For this reason, I only considered the profile cores and discarded the plateau range from 12000 au outwards (see Fig. 4.7(a)). I obtained a shift of 0.50 pixel between the two dust arcs corresponding to expansion velocity of approximately 13 km s^{-1} . I had to make sure that this result is not an effect of left over noise in the radial profiles. So, I created smoothed second epoch profile by convolving solution with point spread profile. I ran Monte-Carlo simulations on it for 10000 times, after adding flat (white) noise with a tweak factor of 3.5 applied to the standard deviation. However, given the systematics induced by the

choice of the outer profile cut-off, I refrain from considering this noise estimate as representative. Thus, in the absence of a rigorous error treatment, I adopted the difference between the two results as a measure of the uncertainty, i.e. 0.14 pixel or 3.6 km s^{-1} , and used their average of 0.57 pixel or 14.8 km s^{-1} as estimate for the overall outer arc tangential expansion velocity.

4.4.2 Inner arc

Study of inner arc radial profile was more challenging than outer arc. The inner arc is much more closer to the central star and also fainter than the outer arc. Due to this, images that were used to analyze outer dust arc could not be used to study inner arc properly. I obtained the F606W Wide Field 3 frames for both epochs, courtesy Dr. Stapelfeldt. The star was already PSF subtracted by him. I could only mark four faint background stars which were common in both frames (fig 4.6). By doing astrometry (tables 4.5 and 4.6) in the same way as for outer arc analysis, the transformation parameters calculated are listed in Table 4.7.

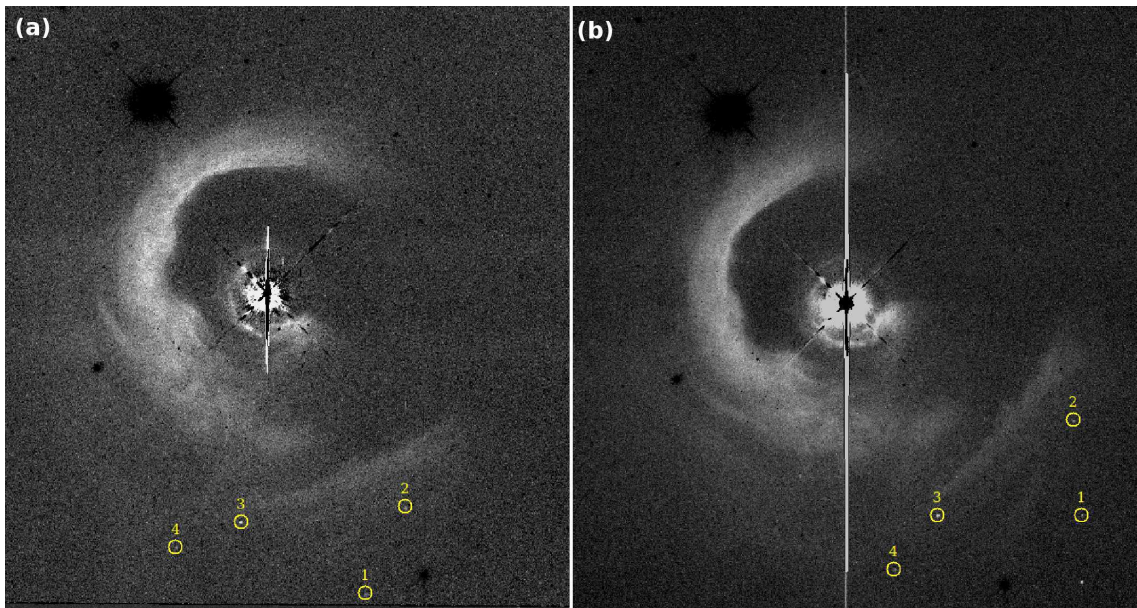


FIGURE 4.6: First epoch (a) and second epoch (b) F606W filter WF3 frames with stars used in astrometry marked on them.

Following the same steps as done with outer arcs, I obtained the inner arc radial profiles for both epochs (shown in Fig. 4.7 (b)). As discussed above, the inner arc profiles are not very well constrained because of their proximity to V1331 Cyg and residuals after PSF subtraction. Using deconvolution method and running

TABLE 4.5: The table lists the (x,y) pixel positions of the stars in first epoch F606W WF3 frame. The errors are also in pixels.

Number	x	y	error (x)	error (y)
1	316.755	774.159	0.396	0.279
2	271.296	672.065	0.276	0.239
3	465.736	689.643	0.152	0.143
4	541.869	720.107	0.331	0.349

TABLE 4.6: The table lists the (x,y) pixel positions of the stars in second epoch F606W WF3 frame. The errors are also in pixels.

Number	x	y	error (x)	error (y)
1	69.816	681.409	0.265	0.327
2	80.045	569.937	0.299	0.235
3	240.372	681.745	0.204	0.192
4	291.072	745.413	0.333	0.327

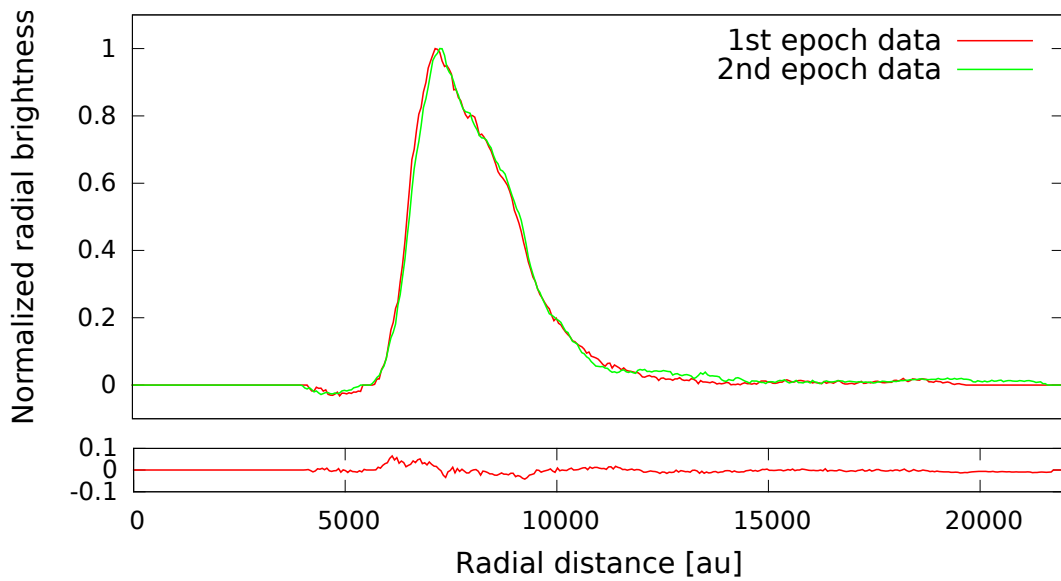
TABLE 4.7: List of parameter values used in the remapping procedure for the inner dust arc, to map 2nd epoch Wide Field frame w.r.t 1st epoch WF frame.

Parameter	Transformation value
Xshift \pm error	-81.4429 ± 0.7883
Yshift \pm error	215.1916 ± 0.7891
Rotation \pm error	0.51748 ± 0.00469
Stretch \pm error	0.99777 ± 0.03511
Reduced χ^2	0.067695

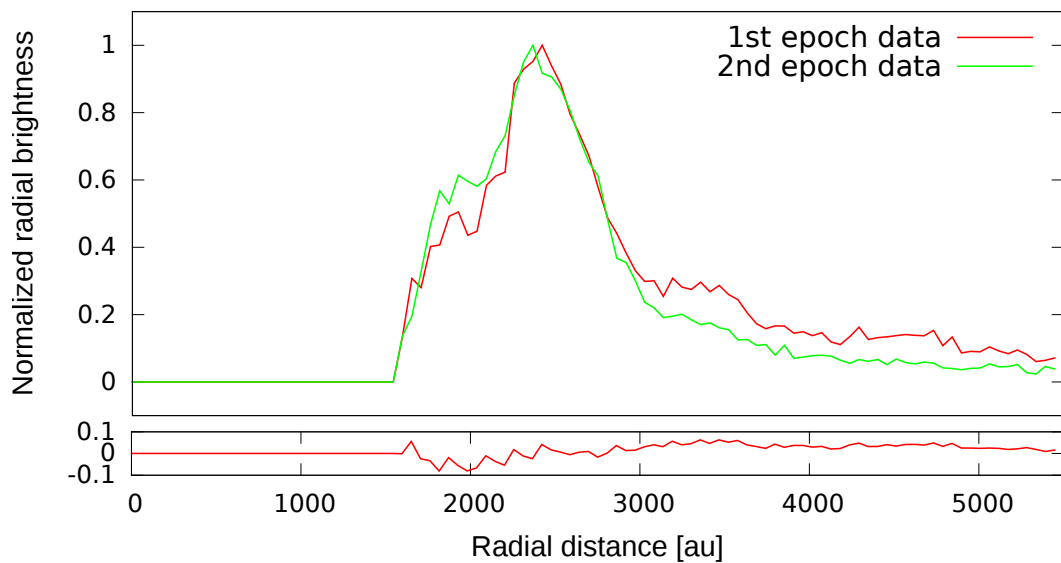
Monte-Carlo simulations again, I calculated a shift of 0.03 and 0.13 pixel between the radial profiles from two epochs, corresponding to expansion velocity of about 0.8 km s^{-1} and 3.4 km s^{-1} respectively.

4.5 HST F606W images direct subtraction

We straight away subtracted the first epoch F606W filter image from the second epoch to look for differences of nebulosity and traces of radial expansion in the outer arc. Though we did not see any brightness variations as such, but interestingly, we found traces for outward motion of the outer arc inner boundary in the north-east (shown in Fig. 4.8). Also, there were residuals seen from SW ridge subtraction, but in the opposite sense. Both features could form, if the coordinate



(a)



(b)

FIGURE 4.7: The radial outer (a) and inner (b) dust arc profiles of V1331 Cyg for F606W filter image from both epochs are overplotted for comparison. The lower panels show the difference in profiles.

transformation is affected by star(s) with substantial proper motion leading to a small shift, but that has already been taken care of. This finding right away hints on radial expansion between the two epochs and thus supports our radial profiles analysis. The inward motion of the SW ridge is probably part of a more complex

kinematics.

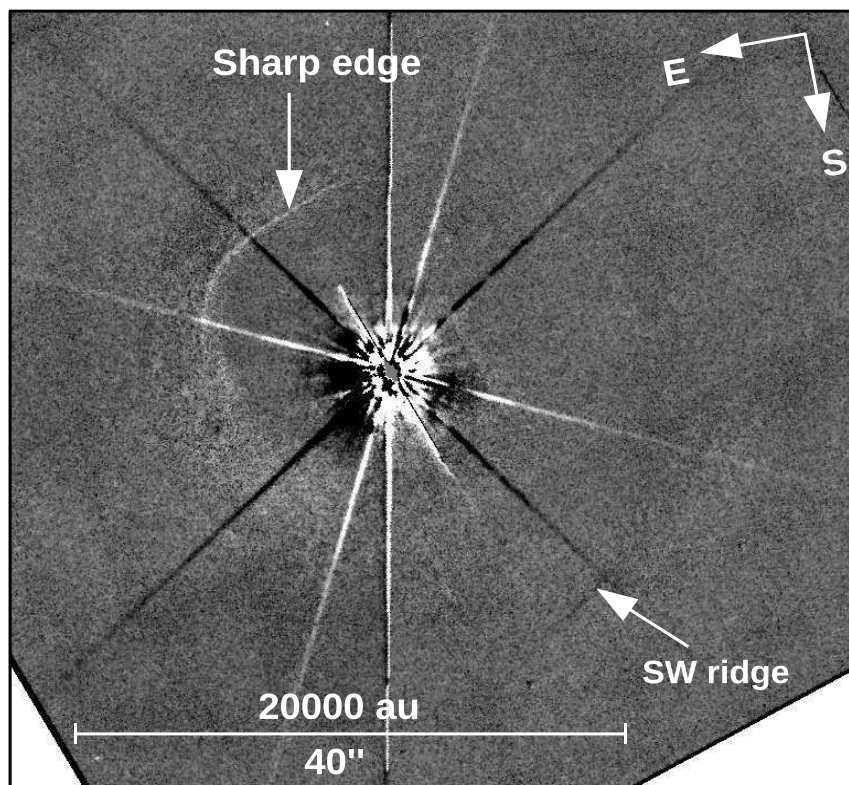


FIGURE 4.8: Difference image (inverse grey scale) of the F606W first and second epoch frames, showing signs of expansion in the NE part of the outer ring.

4.6 Particle separation hypothesis

The selective acceleration of the dust grains results from the relation between their surface cross-section ($\sim r^2$) and mass ($\sim r^3$), and the brief action of the protostellar wind. The ratio between cross-section and grain mass is inversely proportional to the grain size, such that small grains tend to accelerate faster than the big grains. If the strong protostellar wind acts only for a very short period, then it makes the smaller grains reach a higher terminal velocity than the bigger grains. This leads to a spatial separation of dust particles depending on their mass. However, over a long enough time, the grains will anyway reach the same terminal velocity irrespective of grain size.

To study the colour variations in outer dust arc, i.e. to see whether the dust grain size distribution changes across the outer arc as a result of the grain-size dependent acceleration by the brief action of the FUor wind, I used 2nd epoch WFPC2 images from three different filters : F450W, F606W, F814W. I already had the radial outer dust arc profile for F606W filter. Radial profiles for F450W and F814W filter images were obtained on the same lines as done with F606W filter.

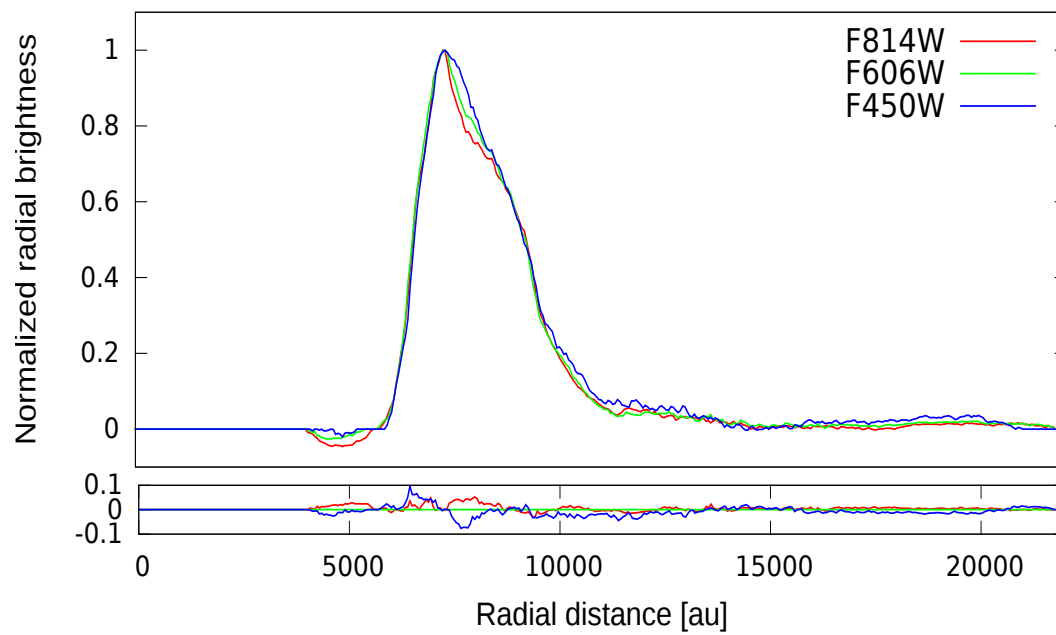
Figure 4.9 (a) shows the variation of outer arc colour between three filters. The normalized radial profiles match pretty well with each other except for the radial values from 7000 to 9000 au (refer to Fig. 4.9 (a), lower panel). No azimuthal variations in the outer arc could be predicted from these profiles, rather this range of radial values makes central part of the dust arc. It was unclear to me, whether the slight variation in normalized profiles is due to local feature concentrated in a particular region in dust arcs, or is it equally distributed effect over whole azimuthal range. To understand it better, I calculated the [F450W-F814W] difference colour image shown in Fig. 4.9 (b). Azimuthal range from north to east has more blue colour than the remaining dust arc. The colour gradually gets more red on moving towards the southwest diffraction spike, starting from east. Concerning the outer range of the profile at distances greater than 15000 au, the normalized brightness seems to be slightly bigger, the shorter the wavelength. This could be a hint that there is an enhanced fraction of smaller dust grains compared to the dust population of the core profile at these distances, possibly due to mixing with ISM dust.

Dividing the azimuthal range in two different sections as mentioned, I obtained two separate radial profiles in each filter for the outer arc. The plots showing colour variations in separate sections are shown in Fig. 4.10.

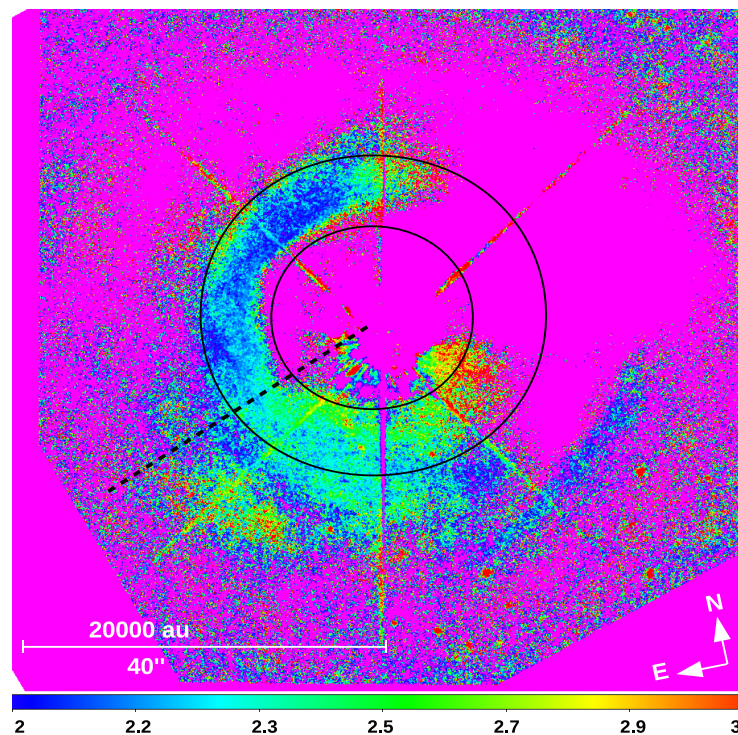
4.7 Photometry of V1331 Cyg

V1331 Cyg is saturated in long exposure WFPC2 frames of HST. I used unsaturated frames with short exposure times (within a few seconds) to calculate magnitude of central source. The results are listed in Table 4.8.

The magnitudes were calculated in VEGA photometric system using the zero points given in the WFPC2 handbook [100]. Stellar brightness is changing between

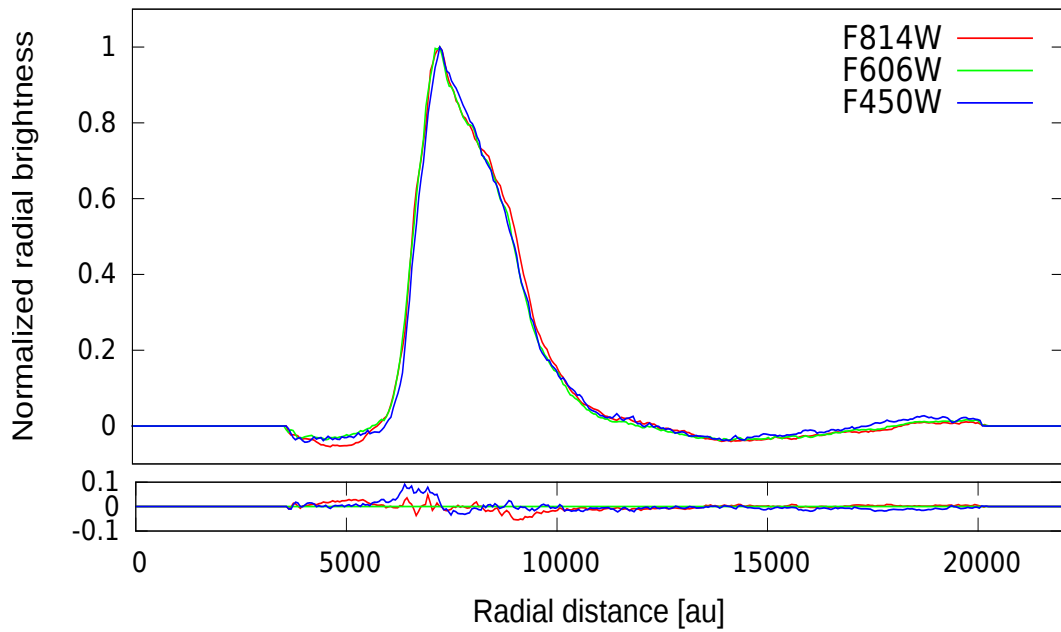


(a)

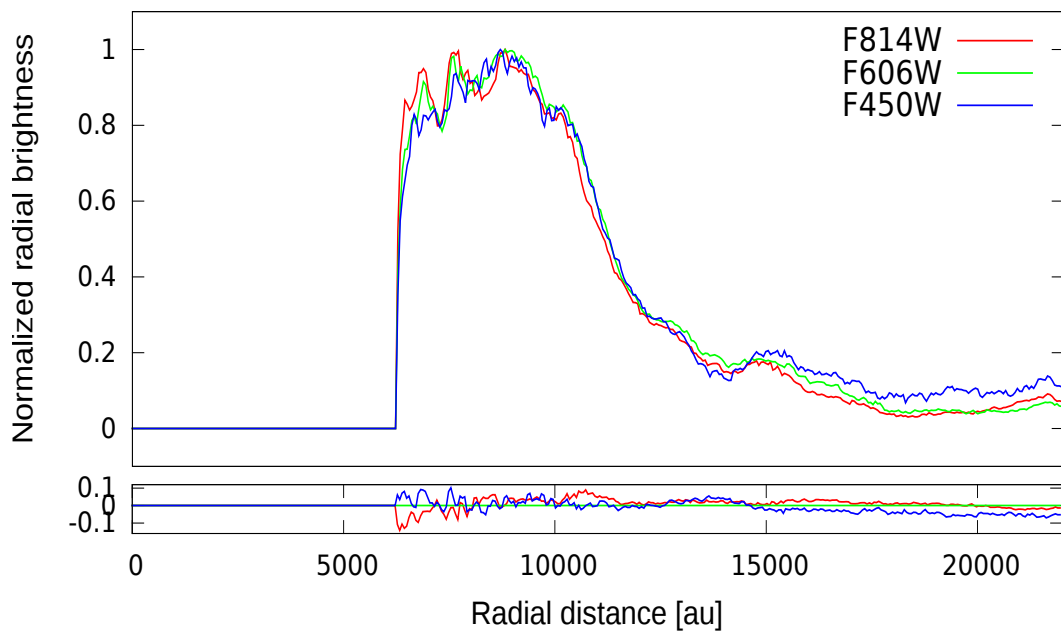


(b)

FIGURE 4.9: (a) 2nd epoch outer dust arc radial profiles obtained in all three filters. The lower panel shows the comparison of normalized profiles with respect to F606W filter. (b) The [F450W and F814W] difference colour image from 2nd epoch filters. The lower bar indicates the colour index range [mag] and the dashed line denotes partition between two parts of the outer arc. the azimuthal colour profile as well as the brightness-colour relation are based on the annular region within the two circles.



(a)



(b)

FIGURE 4.10: Radial profiles for part extending from north to the east diffraction spike (a) and from east to the SW spike (b) azimuthal ranges on outer dust arc. The lower panel shows difference in profiles.

TABLE 4.8: V1331 Cyg photometry

	Magnitude		
	F450W	F606W	F814W
1st epoch	-	11.98 ± 0.003	10.93 ± 0.01
2nd epoch	12.83 ± 0.008	11.77 ± 0.005	10.71 ± 0.006
	colour index		
	F450W-F606W	F450W-F814W	F606W-F814W
1st epoch	-	-	1.053 ± 0.01
2nd epoch	1.05 ± 0.01	2.12 ± 0.01	1.07 ± 0.007

the two epochs by approximately 0.2 mag. The second epoch magnitude values suggest that the star was brighter than first epoch at that time.

4.8 Photometry of outer dust arc

I selected three different regions located on the outer dust arc in F606W filter WF frames from both epochs. Measurement of dust arc surface brightness was done and the results are shown in Table 4.9.

TABLE 4.9: Magnitude per square arcsecond values for 3 aperture positions in outer dust arc from both epochs F606W filter image.

F606W apertures	Surface brightness	
	1st epoch	2nd epoch
1	21.77 ± 0.20	21.90 ± 0.22
2	21.55 ± 0.18	21.62 ± 0.19
3	21.41 ± 0.15	21.46 ± 0.17

The consistent brightness differences between the two epochs suggest that the outer arc got fainter in the second epoch, opposite to stellar behaviour. Although the photometric errors preclude a firm statement on variability, it seems certain that the arc did not brighten unlike the star. For a distance of about 10000 au from the star to the outer arc, the light would take approximately 60 days to travel. As V1331 Cyg is known for its photometric variability on pretty short timescales [84, 120], the difference in stellar and dust arc brightness is acceptable.

4.9 Outer dust arc reddening analysis

In order to check whether the dark cloud LDN 981 has any reddening effect on the dust arc colour, I performed photometry on second epoch frames. I calculated $[F450W-F814W]$ and $[F606W-F814W]$ values at seven different aperture positions (shown in Fig. 4.11) on the outer arc and south west wing. Results are listed in Table 4.10.

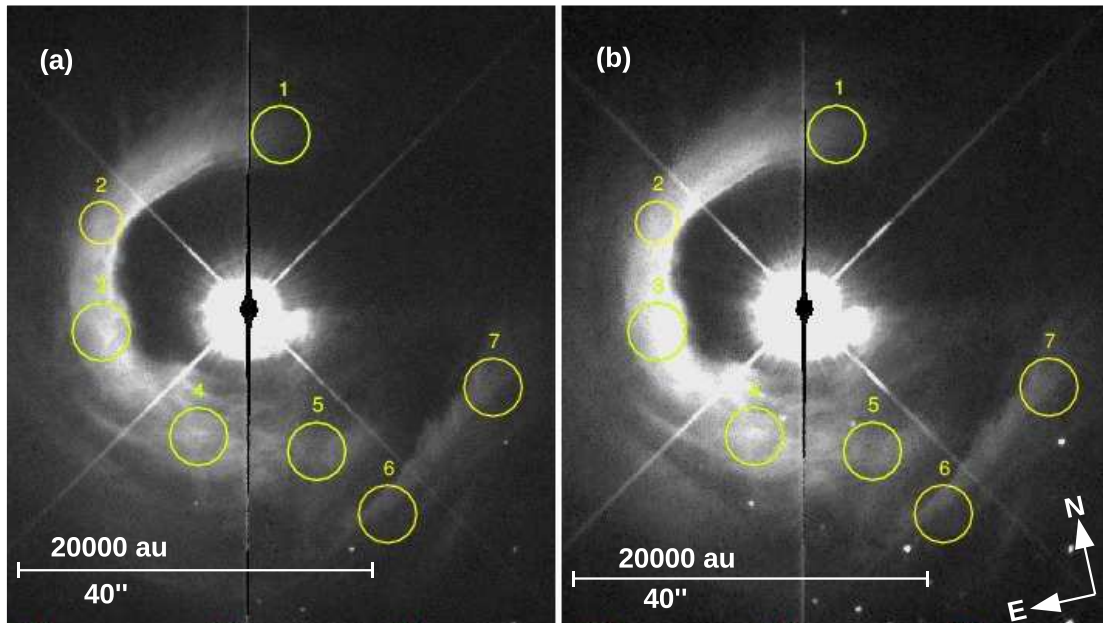


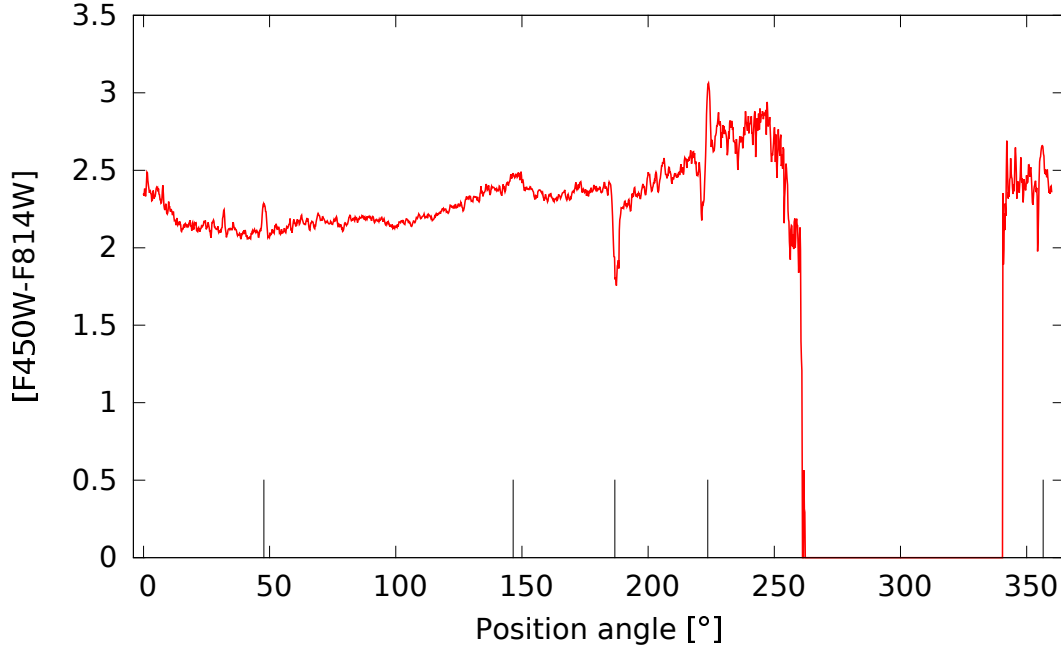
FIGURE 4.11: 2nd epoch F606W image (a) and F814W image (b) showing the apertures marked used for reddening calculation. The same apertures were used for F450W colour calculations.

For aperture 1, the colour index value of 2.53 mag suggests some reddening as compared to all other apertures. In order to investigate whether the missing ring section could result (even partially) due to extinction from the dark cloud, I calculated the azimuthal median profile based on the $[F450W-F814W]$ image (refer to Fig. 4.9 (b)). I followed the method detailed in Section 4.4.1, but instead of obtaining the radial median, I calculated azimuthal median for pixels within the annulus marked by the black circles across all position angles. The resultant plot is shown in Fig. 4.12. The black vertical lines denote peaks caused by diffraction spikes and stellar bleeding on the CCD.

TABLE 4.10: Brightness (mag.arcsec^{-2}) measured in all three filters in 2nd epoch and also the colour indices calculated from it.

Aperture	Surface brightness		
	F450W	F606W	F814W
1	29.21 ± 0.55	27.68 ± 0.18	26.68 ± 0.20
2	27.91 ± 0.45	26.60 ± 0.16	25.67 ± 0.18
3	27.66 ± 0.29	26.38 ± 0.11	25.44 ± 0.13
4	28.09 ± 0.32	26.70 ± 0.12	25.76 ± 0.14
5	28.92 ± 0.48	27.58 ± 0.18	26.67 ± 0.20
6	29.75 ± 0.75	28.31 ± 0.29	27.36 ± 0.32
7	29.36 ± 0.70	28.03 ± 0.26	27.17 ± 0.28

Aperture	colour index		
	F450W-F606W	F450W-F814W	F606W-F814W
1	1.53 ± 0.57	2.53 ± 0.58	1.00 ± 0.26
2	1.31 ± 0.47	2.24 ± 0.48	0.93 ± 0.24
3	1.28 ± 0.31	2.22 ± 0.32	0.94 ± 0.17
4	1.39 ± 0.34	2.33 ± 0.35	0.94 ± 0.18
5	1.34 ± 0.51	2.25 ± 0.52	0.91 ± 0.26
6	1.44 ± 0.80	2.39 ± 0.81	0.95 ± 0.43
7	1.33 ± 0.74	2.19 ± 0.75	0.86 ± 0.38

FIGURE 4.12: Second epoch outer dust arc azimuthal median profile for $[F450W-F814W]$ colour. Vertical bars indicate artifacts.

4.10 Outer dust arc colour-brightness relation

It is already clear from Fig. 4.9(b) and 4.12, that the colour of outer arc varies over quite some range and increases over a PA range from about 30° ... 250° . In principle, spatial grain size variations can lead to colour variation, but this is unlikely for the region under investigation, given its small extent. Assuming a unique grain size distribution, the azimuthal colour trend can then be interpreted as caused by scattering variations. Since the scattering efficiency of dust grains depends on both wavelength and scattering angle [68], for small scattering angles (in case of forward scattering), the scattered light should appear bluer as well as brighter. Since V1331 Cyg (the light source) is displaced from centre of the outer arc, thus, along the arc, the amount of incident radiation depends on the position angle. Taking into account the distance variation, the decrease in surface brightness with distance follows the trend like other reflection nebulae, i.e. approximately proportional to the inverse distance [121].

Following this approach, Dr. Stecklum carried out the analysis. The brightness value of all pixels were multiplied by their respective distance from V1331 Cyg, virtually shifting them to "unit" distance from the star. Remarkably, the re-scaled F814W image shown in Fig. 4.13 revealed the inner arcs even without PSF subtraction. The plot of re-scaled brightness vs. the colour index for each pixel considered in annular region from Fig. 4.9(b) is shown in Fig. 4.14, along with the mean and standard deviation of the colour for brightness bins of 0.1 arbitrary units. Ignoring certain outliers, the general trend that bluer pixels are brighter is obvious. This is an evidence that dust grain scattering governs the colour as well as brightness distribution of the outer arc, primarily due to a systematic change of the scattering angle.

It should be noted though, that the brightness correction based on the projected distance is a conservative case. Regions showing strong forward scattering (depicted blue) have to be in the foreground, implying that their true distance from the star will be larger. So, making proper distance correction, the arc will become even brighter than shown in Fig. 4.13, and enhance the trend seen in Fig. 4.14.

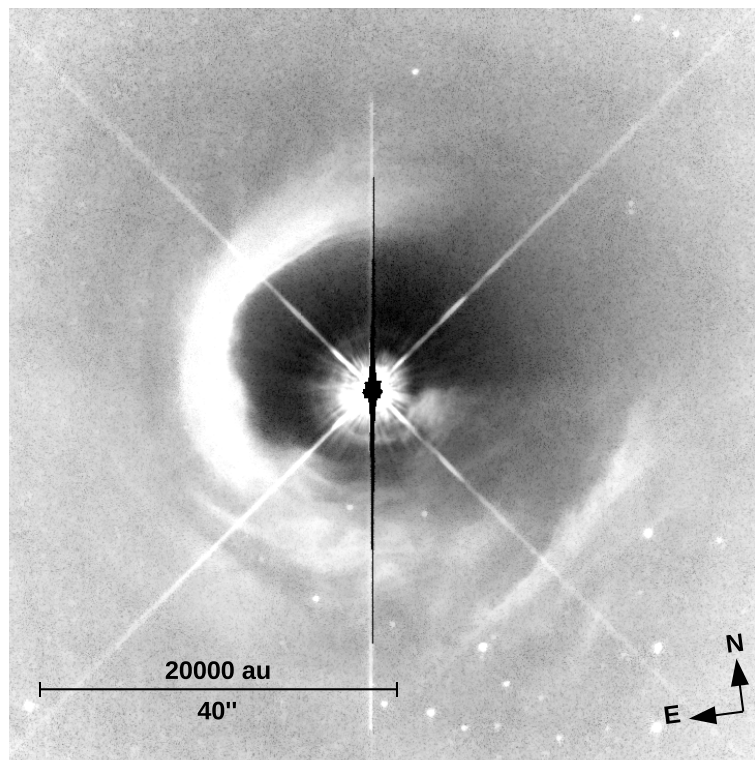


FIGURE 4.13: F814W image with radial flux weighting

4.11 UKIDSS reddening analysis

The UKIDSS JHK colour image (see Fig. 4.15), which is much more sensitive than 2MASS, suggested that there are few faint stars in the gap between the star and outer dust arc. On having a closer look, it seemed to me that the stars are slightly reddened. This could mean that there is enough dust in the gap causing this effect. To investigate the presence of dense matter possibly associated with the protostellar environment and/or the molecular cloud, I made a comparison of reddening of stars inside the gap to those in the environment of V1331 Cyg.

4.11.1 Photometry on UKIDSS data

I used JHK band images separately and performed photometry on them using SExtractor (Source Extractor) [122] while the tabular data was handled using TOPCAT (Tool for OPERations on Catalogues And Tables) [123]. The stars marked as 1, 2 and 3 in Fig. 4.15 are the stars inside the gap, and stars numbering 4 to 11 lie in a region just outside the outer dust arc.

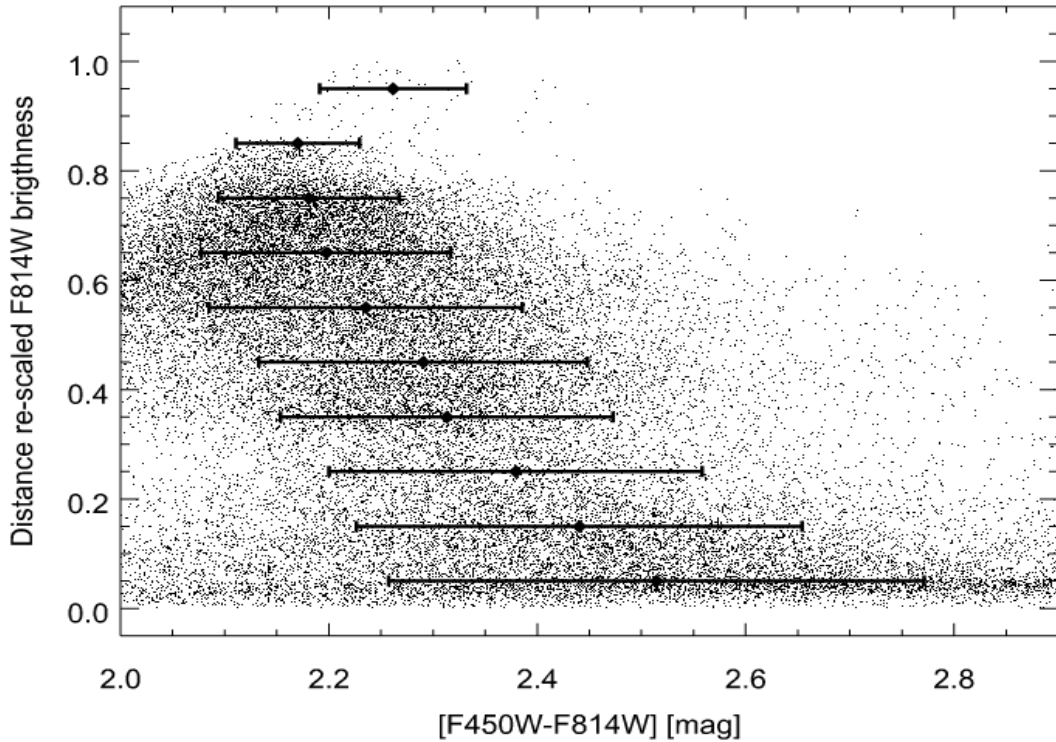


FIGURE 4.14: Re-scaled brightness vs. colour plot for pixels of the outer arc confined within the annulus shown in Fig. 4.9(b).

In order to separately detect stars 1 and 2 in SExtractor, I had to set the parameter *detection-threshold* to $3 \text{ mag arcsec}^{-2}$ in the input configuration file for K band, and the same was set to a value of $2 \text{ mag arcsec}^{-2}$ for H band. Stars 3, 10 and 11 were not detected in J band image at all. SExtractor allows using two images in a single run, where, the first image is used to detect sources for the second image, and then performs photometry on second image at the detected co-ordinates. So, I used the K band image for detection and J band image to get photometry for them in the J band. Star number 1 had large errors in magnitude due to its close positioning to V1331 Cyg, thus influencing its colour. I selected another star of similar brightness in the same field in K band image and subtracted it from V1331 Cyg to cancel its scattering halo. The new magnitudes for star 1 were re-calculated.

I plotted the $[J-H]$ vs. $[H-K]$ colours on the colour-colour plot along with the 2MASS colours (obtained from DS9, using *catalog* tool for Infrared 2MASS point sources) for comparison. The UKIDSS colours were found to be slightly blueshifted than 2MASS. To correct UKIDSS colours with respect to 2MASS, I

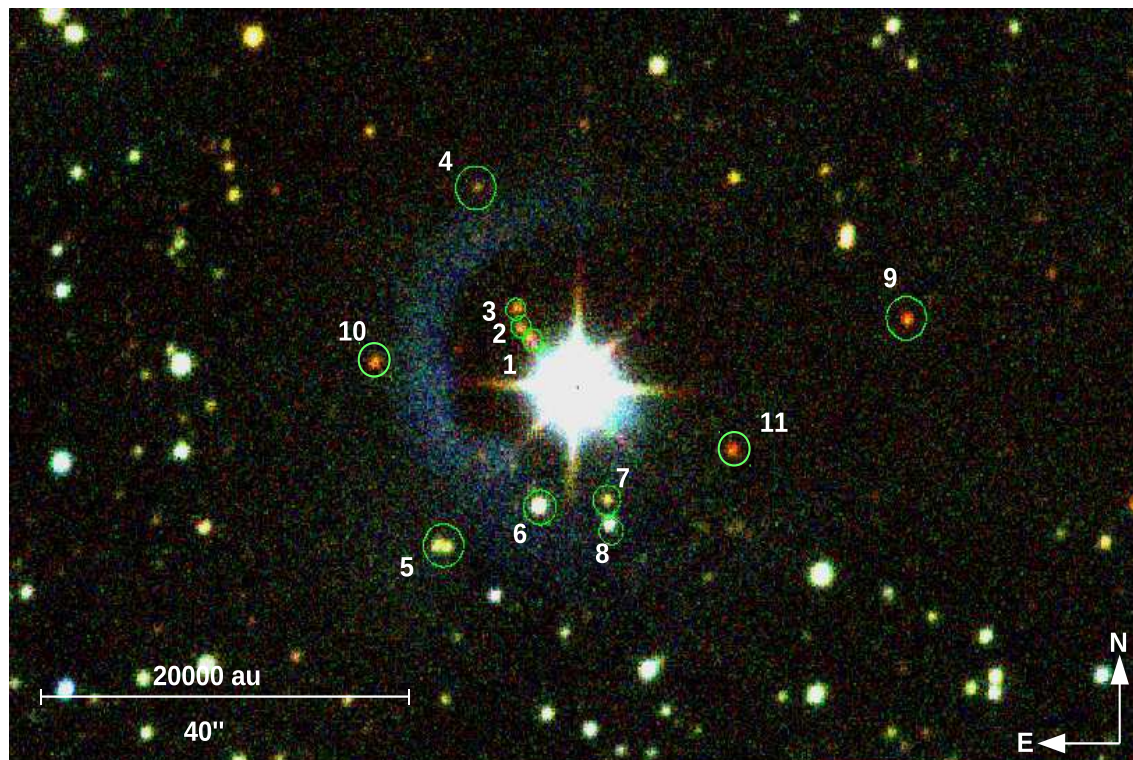


FIGURE 4.15: UKIDSS JHK band colour image showing the stars marked for reddening analysis.

plotted UKIDSS magnitudes vs. 2MASS magnitudes, which came out to be almost straightline as seen in Fig. 4.16.

I performed regression technique to get a straight line fit for all three bands. IDL routine *LADFIT* was used to come up with the following solutions (eq. 4.1, 4.2 and 4.3).

For J band,

$$J_U = -2.4939089 + 0.9997 \times J_M \quad (4.1)$$

For H band,

$$H_U = -2.3230144 + 0.9959 \times H_M \quad (4.2)$$

For K band,

$$K_U = -1.6955070 + 1.0046 \times K_M \quad (4.3)$$

where, J_U, H_U, K_U denote UKIDSS magnitudes and J_M, H_M, K_M denote 2MASS magnitudes.

The constant terms from the above equations were then added to their respective UKIDSS magnitudes as correction term.

Even after using K band image as detection frame for J band photometry, J magnitude for star no. 3, 10 and 11 could not be calculated by SExtractor. So, I measured the limiting magnitude for the same in J band. I plotted a histogram for J magnitudes, where, the stars from bright to faint were first rising in number, but the frequency declined after reaching a peak value of about 17 mag. This would ideally mean that stars fainter than 17 magnitude will not be detected in J band. To have a better estimation of the limit, I fitted a powerlaw to the rising part of histogram upto maximum frequency point. The fitted powerlaw profile also hinted on a limiting magnitude of about 17 for 50% detection, further suggesting that a star fainter than 17 mag might escape detection in the J band. Hence, the limiting magnitude for star 3 inside the gap is assumed to be 17. The final colour-colour plot is shown in Fig. 4.17. Additional data for Supergiants branch and main sequence stars was used, as a reference to overall photometry of V1331 Cyg field.

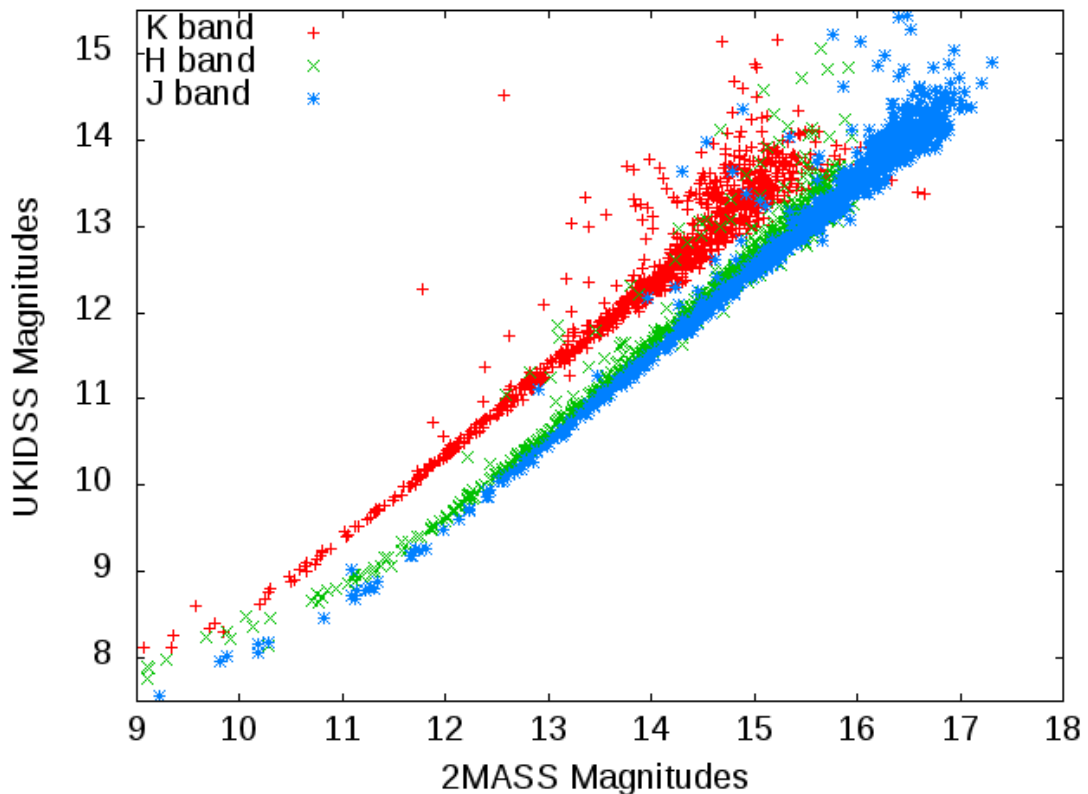


FIGURE 4.16: The J, H and K magnitudes of 2MASS and UKIDSS are plotted to get the correction term for UKIDSS colours.

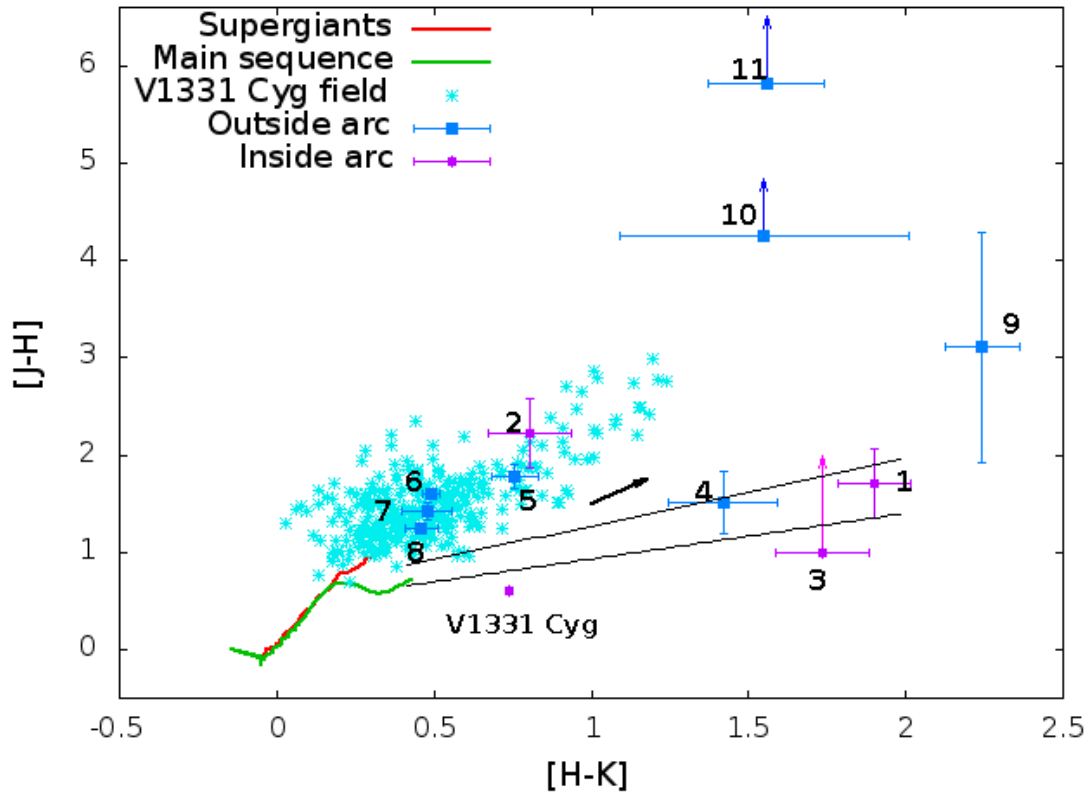


FIGURE 4.17: The colour-colour plot for UKIDSS stars surrounding V1331 Cyg along with the reddening vector for $A_V = 2.4$ mag. The two inclined lines mark the borders of dereddened classical T Tauri stars [124]. The Supergiants and main sequence data is adapted from Koornneef [125].

The reddening vector was calculated using methods detailed in Indebetouw et al. [126].

From the colour plot, star 1 appears to be a possible candidate T Tauri star. Star 2 follows the reddening path for main-sequence stars. Though extinguished by A_V of 7...10 mag, star 2 still comes in the range of adjacent field stars. Star 3 could be a more heavily reddened star or a young stellar object showing infrared excess. Same goes with star 4 and 9 as well. Stars 5 to 8 are less reddened while stars 10 and 11 are highly reddened. From this analysis, I conclude that there is no evidence for the stars in the gap to be more extinguished compared to the surrounding stars, further suggesting that there is no matter from the protostellar environment between the outer arc and V1331 Cyg, i.e. the gap is real.

In addition to reddening analysis, the UKIDSS images also had the potential to reveal as to how the appearance of scattering nebula is influenced because of

dark cloud presence. At near-infrared wavelengths, the smaller scattering cross section of dust grains leads to lower surface brightness, making it possible to study dark cloud morphology closer to the star. This analysis was conducted by Dr. Stecklum. Images were adaptively smoothed to enhance low-level surface brightness using algorithm by Pantin and Starck [127]. Fig. 4.18 reveals the "cloudshine" [128] of the filamentary dark cloud. Stretching from west to east behind V1331 Cyg, LDN 981 then turns north slightly east of the star.

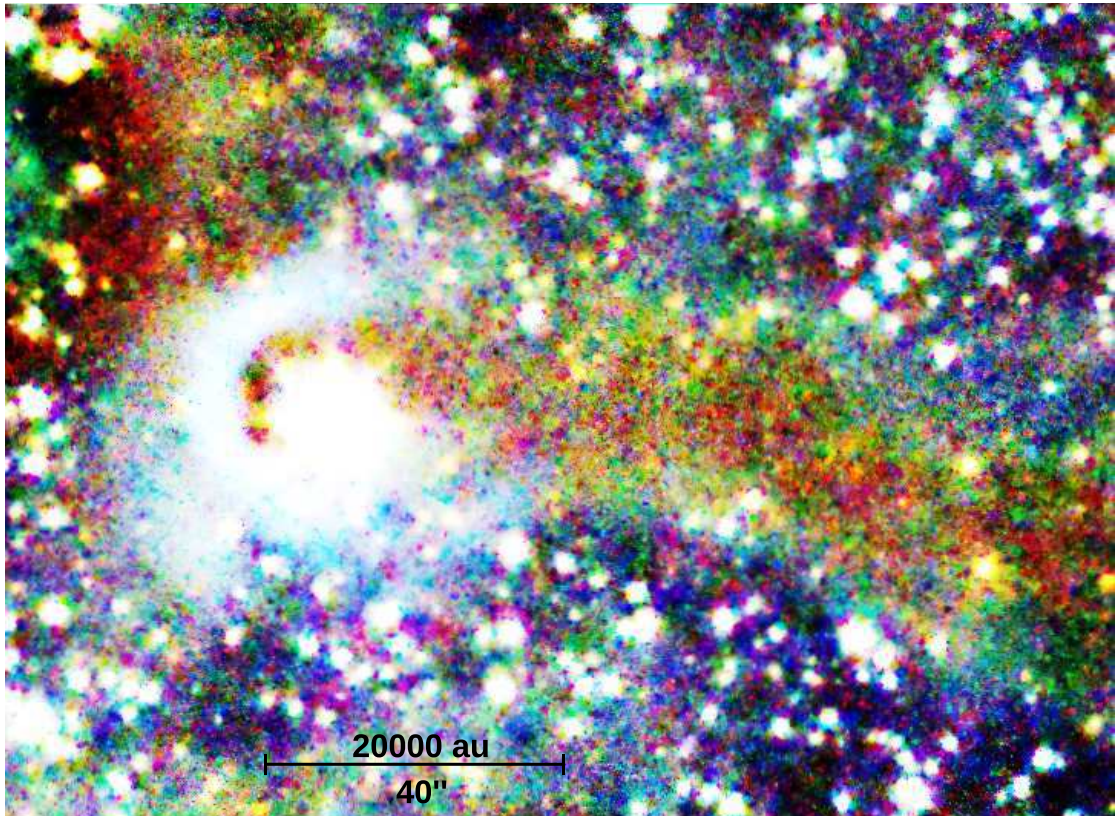


FIGURE 4.18: Histogram-equalized colour image based on adaptively smoothed JHK UKIDSS images. V1331 Cyg is in front of the bending filamentary dark cloud. The dark area at the northeast border is an image artifact.

The dark cloud morphology corresponds to what has been seen in emission at coarse resolution with SCUBA [129] as well as HERSCHEL/SPIRE [97]. Since stars 4, 9, 10 and 11 are much redder than stars 5 to 8 south of the YSO (Fig. 4.17), the cloud morphology supports the view.

4.12 HERSCHEL/PACS results

My attempt to detect extended thermal dust emission from V1331 Cyg was based on PSF subtraction. From the variety of target images and PSFs established with different data processing techniques, Dr. Stecklum produced PSF-subtracted frames and looked for the one with the smallest residuals in the least-square sense for each band. It turned out that the JSCANAM images with a pixel fraction of 0.1 applied in the Drizzling algorithm in combination with non-drizzled PSFs based on re-centered Vesta observations performed on operational day 345 yielded the smallest Chi Square values. The fact that these PSFs are suited best for the drizzled target images may be explained by a contribution from warm dust of the inner rings which slightly widens the PSF of V1331 Cyg. The PACS PSFs were scaled to match the target peak flux value. The subtraction was performed using an oversampling factor of three together with fractional pixel shifts to achieve the Chi Square minimization. The two 160 μm images obtained in parallel with the 70 and 100 μm observations were registered separately with respect to the PSF before averaging them, and performing the subtraction.

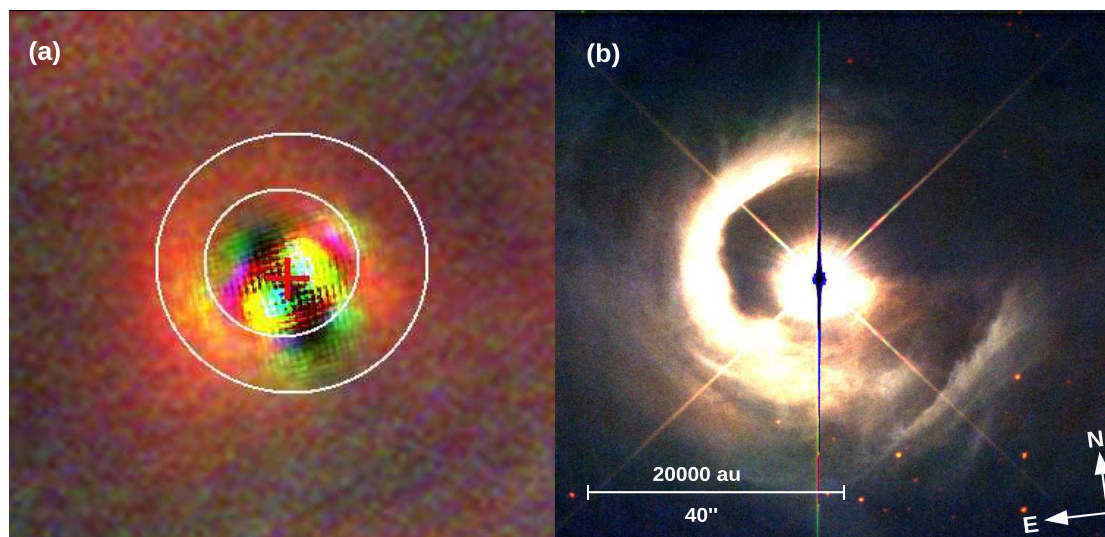


FIGURE 4.19: (a) Herschel colour composite image of the residuals after PSF subtraction, with annular region showing emission from outer arc, along with HST 2nd epoch colour image (b) for comparison.

Herschel 160, 100, and 70 micron RGB composite image based on the three PSF-subtracted frames is shown in Fig. 4.19, where the white circles mark the boundaries of the outer annular scattering nebula. Since the residuals of the 70 μm image were almost fully confined by the inner circle, it was concluded that

these were entirely due to PSF mismatch. For the 100 μm channel, however, some residual emission could be seen within the confining circles, predominantly to the SW. Thus it was concluded that it originates from the dust of the reflection nebula. This was further supported by the clear detection of residual emission in that same area at 160 μm which even stretches to larger radii. Whether this extent is primarily due to the wavelength-dependent width of the PSF or a radial temperature gradient cannot be distinguished with the present data.

In order to estimate the 160 μm flux, the residual emission was integrated within radii of 11" and 35" centered on the star, taking the local background into account. This yielded a value of 1.06 ± 0.01 Jy. The formal error from the image noise is certainly a lower bound only. The fact that the reflection nebula diminishes in the NIR (refer to Fig. 4.15) indicates that it is optically thin at wavelengths observed with PACS for sure. In case of optically thin emission, the mass can be derived using the formula given by the equation below.

$$M = \frac{4}{3}\pi N \rho_d a^3$$

where, ρ_d is the mass-density of a dust grain, a is the dust grain radius and N is the number of dust grains in the source.

With this proposition, and assumptions on the dust temperature, opacity as well as distance, a mass estimate can be derived. To this aim, the approach by Hayward et al. [130] was followed using the same dust parameters. Since the tentative detection at 100 μm cannot be used to infer a temperature, a value of 15 K caused by the heating of both V1331 Cyg and the interstellar radiation field, was adopted. This yielded a dust mass of $4.5 M_{Earth}$. The mass estimate, however, is very sensitive against temperature, and drops to $1.0 M_{Earth}$ for 20 K.

4.13 V1331 Cyg Bipolar Outflow

The young star V1331 Cyg is associated with a bipolar outflow as shown in Fig. 4.20. Earlier estimates suggested a viewing angle of 30 to 40 degrees towards the star, thus, implying an outflow extent of about 1 pc. But, with the

recent updates on viewing the star almost pole-on, I estimated the bipolar outflow length to be 10 pc or even more (the extent being more for smaller viewing angle). The appearance of the flow suggests it is slightly bended instead of being straight. This could happen due to interaction with surrounding material, which diverts the path of the outflow, resulting in a structure like we see today. Another explanation could be precession induced by binarity of the driving source. A hint on binarity could be the faint spiral-like emission feature stretching to the south from V1331 Cyg, if it was a wiggling jet as claimed by Mundt and Eisloffel [90]. TLS image however shows that the structure rather represents the photo-ionised skin of a filamentary molecular cloud. It is possible that the redshifted flow interacts with this cloud and gives rise to the southern Herbig-Haro Object (HHO).

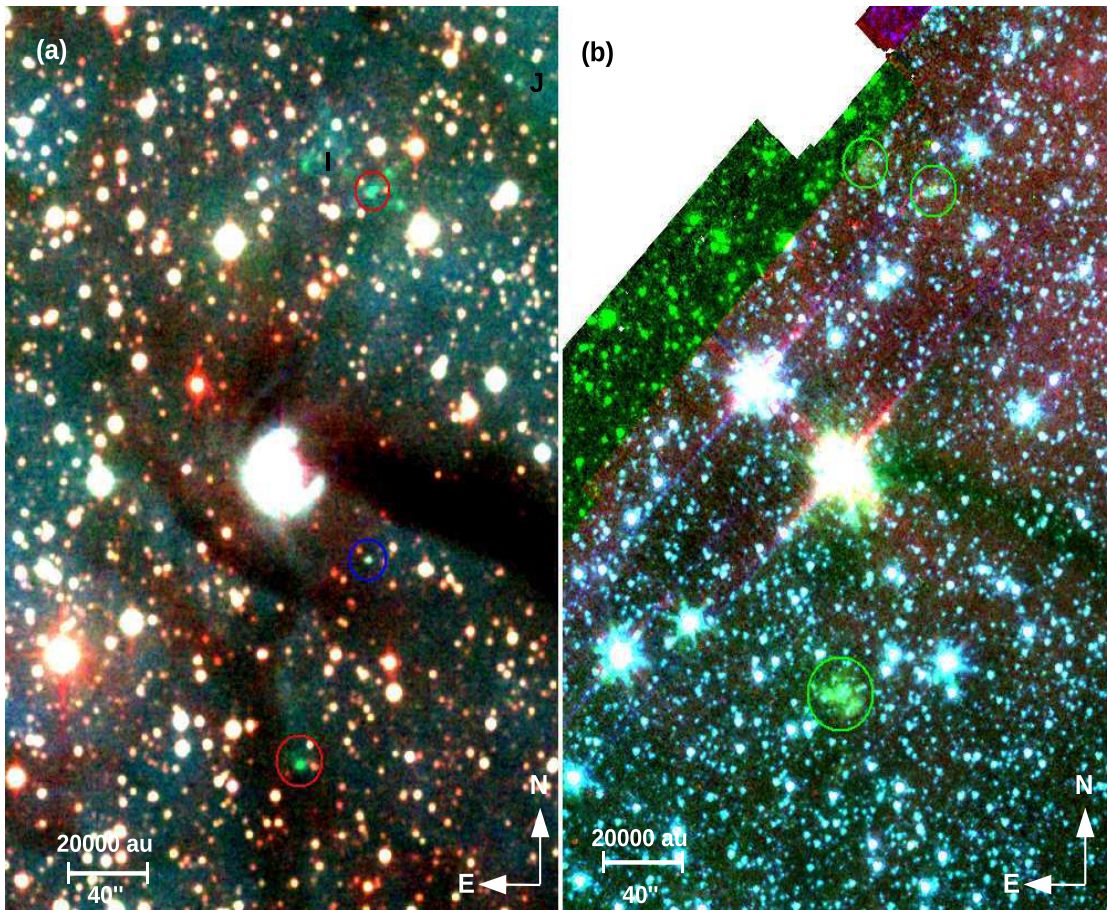


FIGURE 4.20: TLS image (a) and Spitzer-IRAC (b) showing the bipolar outflow from V1331 Cyg. The optical RGB image is composed of I, H α , and [SII] frames. The newly found HHOs I and J are labelled according to the nomenclature of Mundt and Eisloffel [90]. The two brightest HHOs for which spectra were obtained are encircled in red. The blue circle marks an emission line star without notable infrared excess. The 4.5 micron emission from shocked H₂ is marked in the IRAC image as well.

4.13.1 HHO spectroscopy

The HH objects spectra taken at TLS are shown in Fig. 4.21. Lines of $H\alpha$ (656.28 nm) and [SII] (671.7 nm and 673 nm) have been detected for both northern and southern HH objects. The northern HHO is blue shifted while the southern one is redshifted. Both the northern and southern HHO have similar peak signal to noise ratio of about 24. Radial velocity for the southern HHO is $+28 \text{ km s}^{-1}$ and for the northern HHO, its value is -50 km s^{-1} . The formal error of the velocity is about 10 km s^{-1} . The northern HHO shows [OI] and [CaII] (marginal) which is not seen in the spectrum of the southern HHO. This is clear evidence for different excitation conditions. The difference in the radial velocities of the HHOs is nothing extraordinary. Asymmetric jets have been observed frequently (for example DG Tau). Remarkably, the sense of the HH flow is opposite to that of the CO flow as claimed by McMuldroy et al. [89].

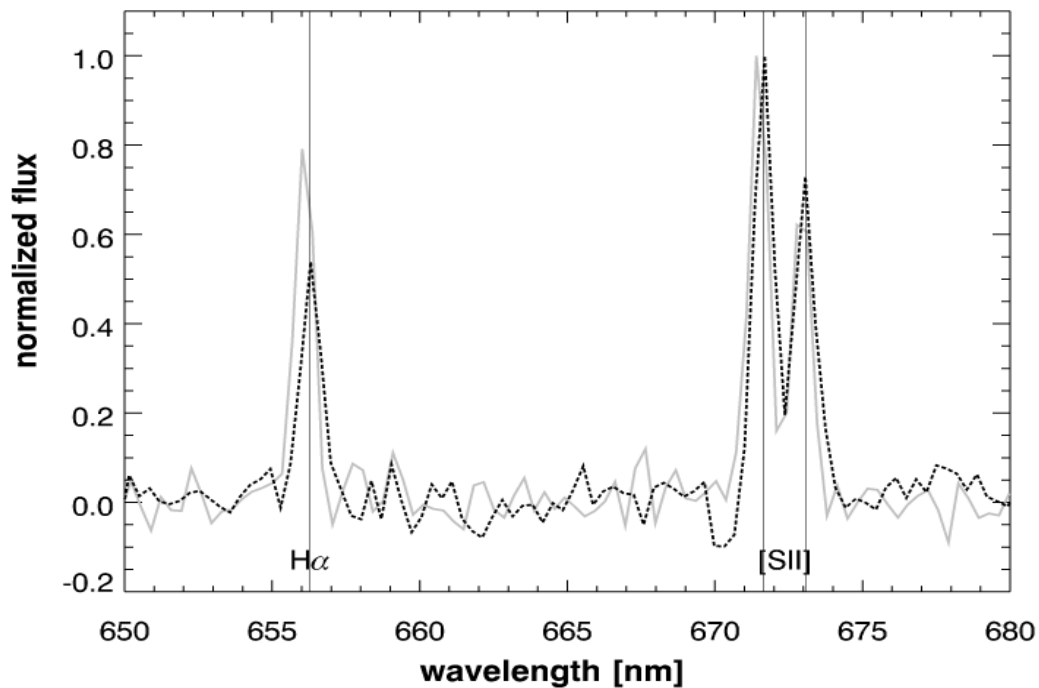


FIGURE 4.21: Northern blueshifted (grey) and southern redshifted (black) HHO spectra obtained using 2-m Tautenburg Telescope. The vertical grey lines denote the rest wavelengths of $H\alpha$ and [SII] lines.

4.14 South west ridge extension

The SW ridge at a projected distance of about 13000 au from the star, does not seem to be connected to outer dust arc. The [F450W-F814W] colour index image (see Fig. 4.9(b)) shows that it is quite blue at a uniform level, suggesting the SW ridge to be a foreground feature. The direct difference image (Fig. 4.8) shows evidence for SW ridge's motion towards V1331 Cyg, and hence it is not related to the expanding outer arc.

In HST second epoch F814W filter image (see Fig. 4.22(a)), I noticed another faint arc-like feature running from northeast to north, lying further outwards than the outer dust arc. This new found feature seems to be more elliptical in shape. I looked up for the same feature in Digital Sky Survey (DSS) close up image (refer to Fig. 4.22(b)), and it appears to be linked with the South West (SW) arc in some way. However, this cannot be justified as there is a gap between the newly found arc and the SW ridge and also the connecting turn is very sharp in angle. This new feature could as well be some interstellar material pushed away by V1331 Cyg during early stage of star formation.

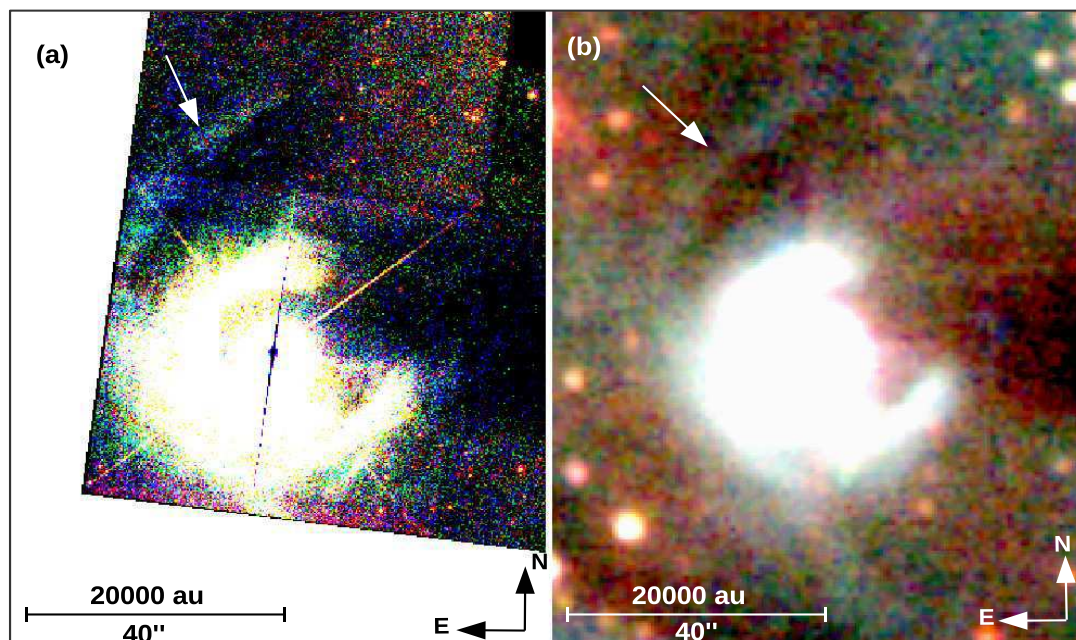


FIGURE 4.22: (a) HST second epoch colour image compared with (b) TLS image. The newly found arc like feature is marked in both images.

4.15 V1331 Cyg SED

Using the YSO online SED fitter from Robitaille et al. [131], I generated model spectral energy distribution (SED) for V1331 Cyg. The input fluxes used from Vizier photometry viewer [118] to establish the SED, are listed in Table C.1, (refer to Appendix C). The fitter takes in flux values through an online form and runs a grid of 200000 YSO model SEDs to find the best fit. Figure 4.23 shows the input SED over-plotted with the best fit produced.

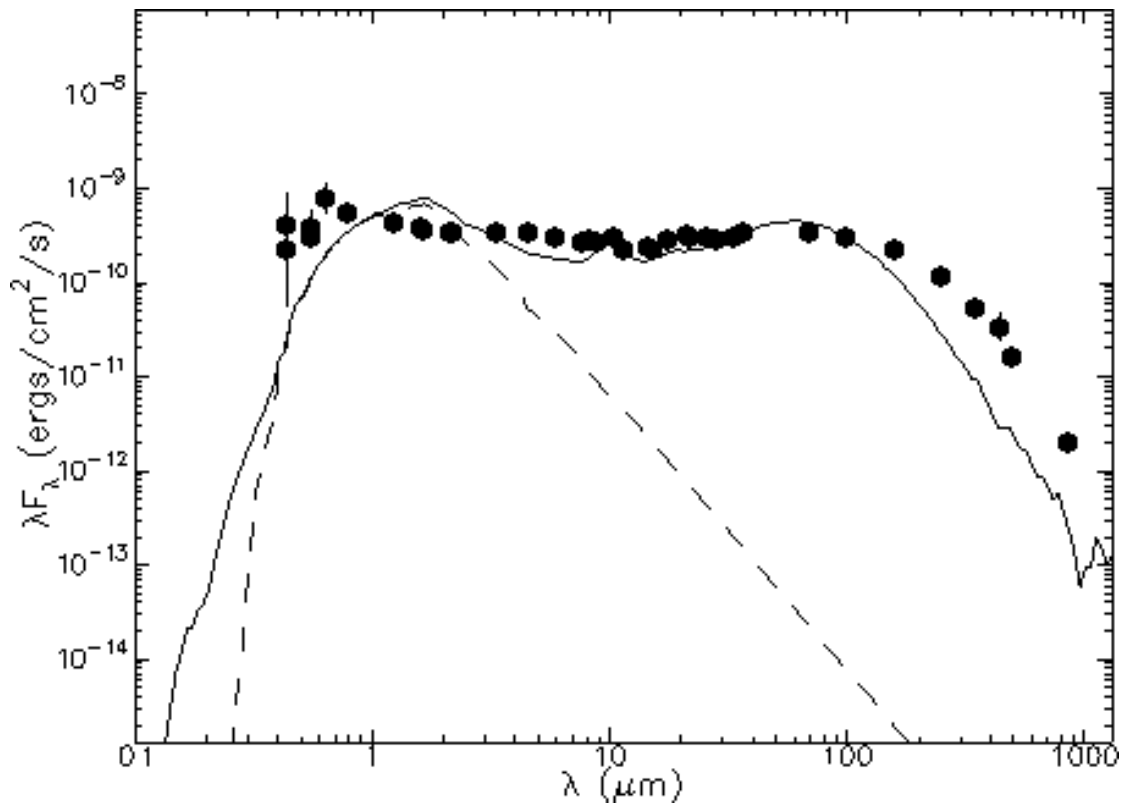


FIGURE 4.23: The filled circles show the input fluxes and the black line shows the best fit. The dashed line shows the stellar photosphere corresponding to the central source of the best fitting model, as it would look in the absence of circumstellar dust (but including interstellar extinction).

V1331 Cyg has a very flat SED, only showing the 10 micron silicate emission feature. The astrophysical quantities obtained for the best fit model at the lowest possible inclination are summarized in Table C.2. The results are compared with independent SED analysis done by Gramajo et al. [132] and Petrov et al. [99]. Results from my analysis do not agree with the other two works.

4.16 New scattering knot close to the star

First epoch short exposure F814W planetary camera image was cleaned and PSF subtracted, by Dr. Stapelfeldt. While working with him during my stay at the Goddard Space Flight Center (GSFC), I obtained the data from him and looking close to the centre of the star, I found a knot like feature (Fig. 4.24 (a) and (b)). The knot is at about $0.''4$ away from the star in the direction of the ring gap. Assuming V1331 Cyg at a distance of 550 pc from us, the knot is at a distance of around 220 au from the central source. The mini arc found by Kitamura et al. [94] seems to be attached to the newly discovered knot. The knot can also be seen in short exposure F606W frames, as the central source is not saturated.

4.16.1 Subaru-CIAO coronagraphic imaging

Additional study of the inner feature discovered, was done using archival Subaru data. Figure 4.24(c) shows PSF subtracted archival Subaru image of V1331 Cyg compared with HST-PC image.

Where on one hand, the HST-PC image PSF subtraction has left behind some residuals, on the other hand, the effective radius of the coronagraphic mask ($0.''45$) governs the angular range of the CIAO image. In the CIAO image, outside the radius of $0.''45$, three features are identified. There is excess emission at the mask edge in the NW direction with increasing radial extent to the west. Also with increasing radius, the surface brightness of this feature falls off. At eastern edge of the excess emission, about $1''$ from the star, it joins a spiral feature which stretches outward to $1.''3$ towards the south. This feature does not show striking radial surface brightness gradient. There is also a weak diffuse emission at $1.''3$ towards the southeast. Since it lies at the position angle of one of the spider pattern, it might be affected by imperfect subtraction. The CIAO spiral feature resembles that seen in HST-PC image, however, the azimuthal brightness variation seems to be weaker, perhaps due to imperfect spider subtraction. Another faint eastern emission is seen in HST. This emission is farther out in H band CIAO image as compared to HST, leaving doubt on reality of the matter.

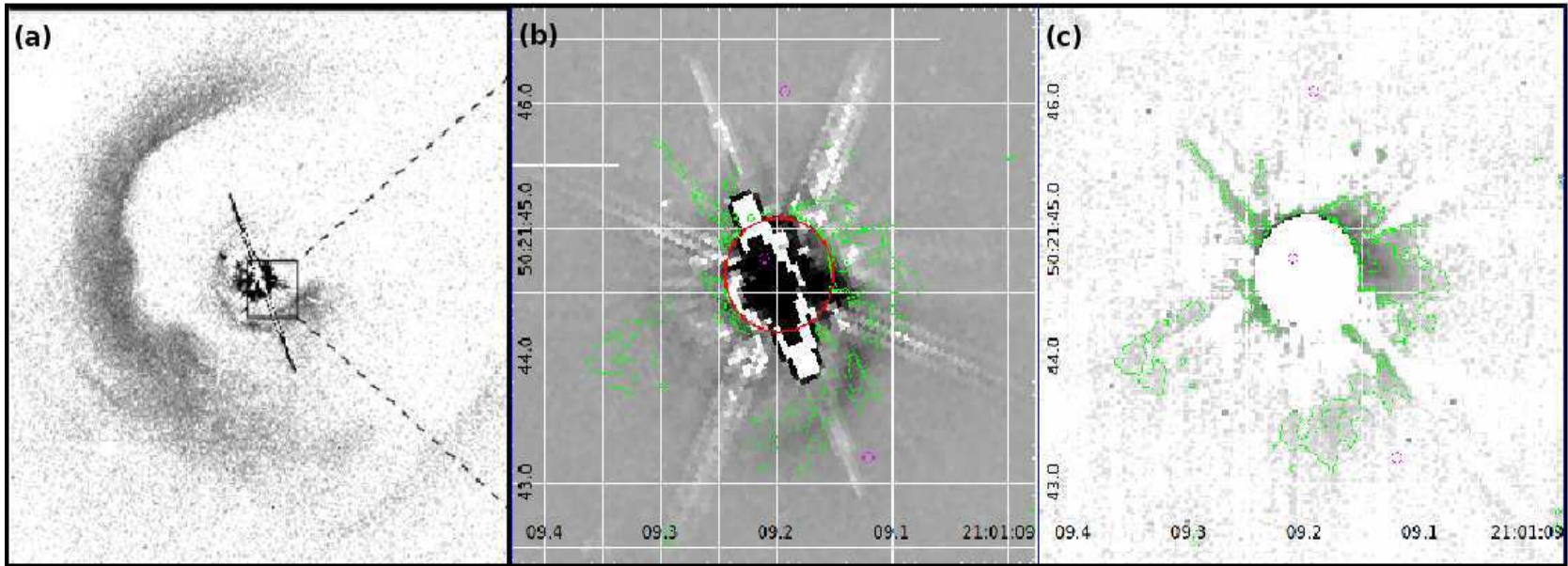


FIGURE 4.24: First epoch F814W HST-PC image of V1331 Cyg (a), magnified view showing knot (b) and Subaru image revealing scattered light (c) in the same direction.

4.16.2 Self subtracted HST knot photometry

As the PSF-subtracted HST F814W image already gave an idea on the position angle of the knot feature, I could then perform angular differential image (ADI) analysis. With this approach, the self-subtraction yields better PSF cancellation and makes it possible to study in detail, the features positioned very close to the star.

In order to understand the nature of the knot better, I performed photometry on the first epoch short exposure F606W and F814W images at the knot position. Even after PSF subtraction, the residual emission from V1331 Cyg contributes enough to affect the knot photometry calculation. To get rid of that, I rotated individual frame from both filters and subtracted the rotated images from the respective originals. The knot then stood out in brightness, almost free from residual starlight (see Fig. 4.25).

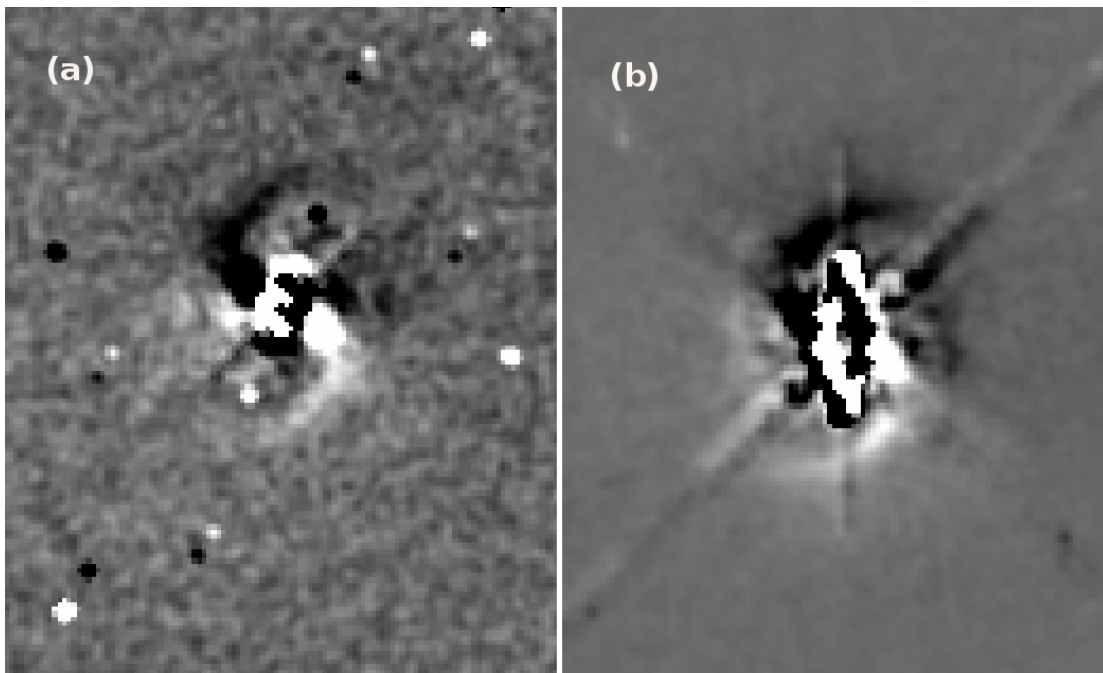


FIGURE 4.25: HST F606W (a) and F814W (b) self subtracted image, showing the prominent knot.

Applying proper extinction, I then calculated the apparent magnitudes for F606W and F814W filters as 15.45 ± 0.04 and 15.43 ± 0.01 respectively. The [F606W-F814W] colour then turns out to be ≈ 0.02 .

4.17 PdBI data

The PdBI observations were conducted over the UV coverage range as shown in Fig. 4.26. The 1 mm continuum map obtained (Fig. 4.27) shows disk emission from V1331 Cyg, which when seen at low contour levels showed slight extension to the west. This finding could be another evidence in support of the knot like feature seen in HST (refer to Fig. 4.24).

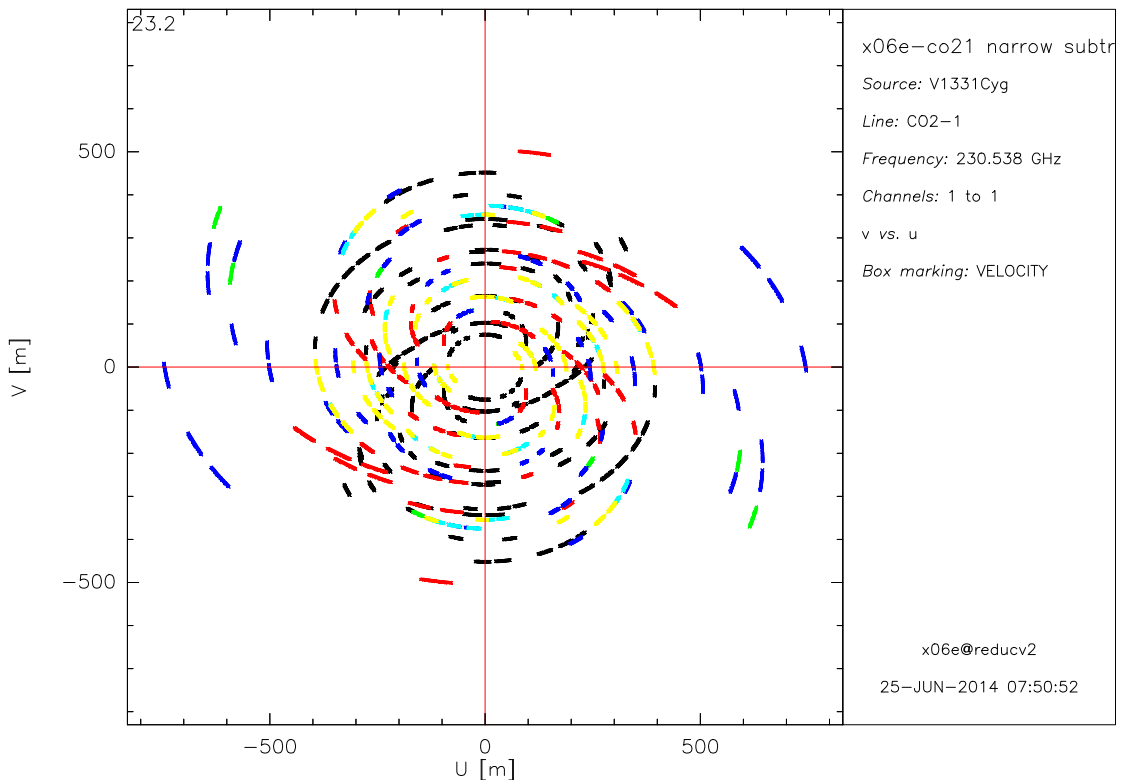


FIGURE 4.26: UV plane coverage of PdBI for observing V1331 Cyg

Also, the CO (2-1) line profile on source as obtained by the data reduction pipeline, is shown in Fig. 4.28, which mimics the P Cygni profile (refer to Appendix A) with a strong absorption feature. This seems to be an indication on the presence of dense CO gas in the line of sight to the star, which is causing such a deep absorption feature. These are just the pipeline-produced preliminary results, and the data would need further more quantitative analysis before I could make any firm conclusion based on it.

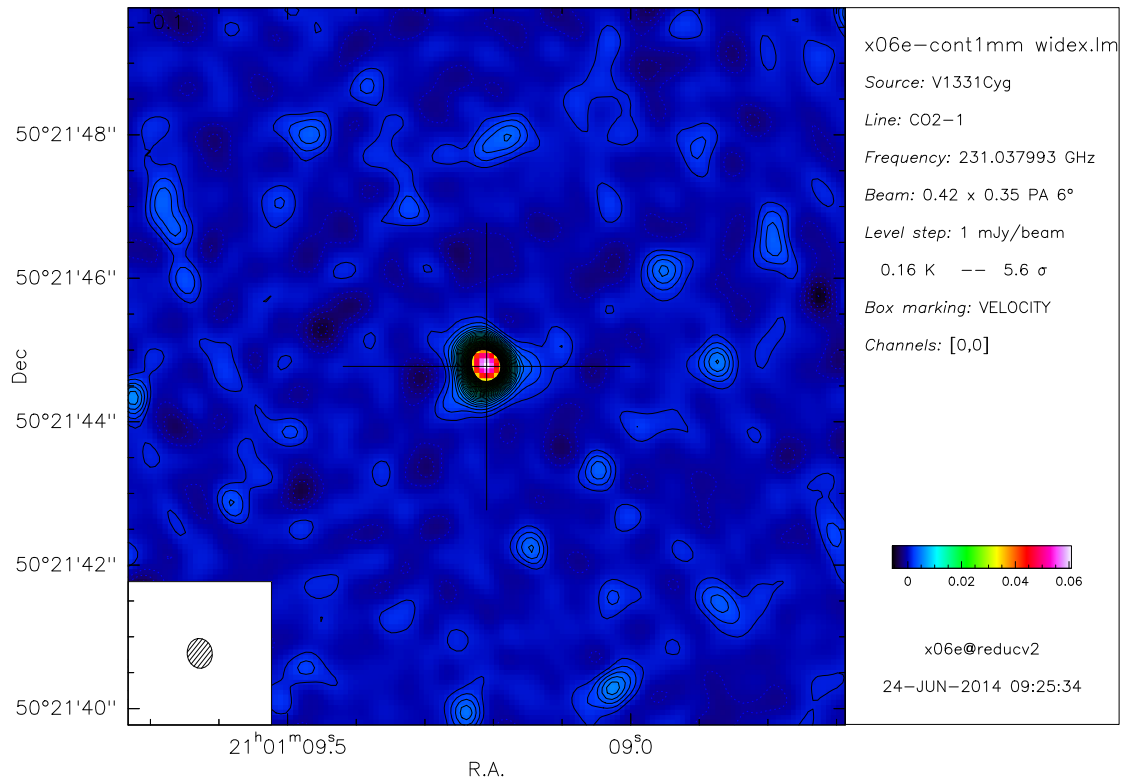


FIGURE 4.27: 1 mm continuum map for V1331 Cyg obtained with PdBI

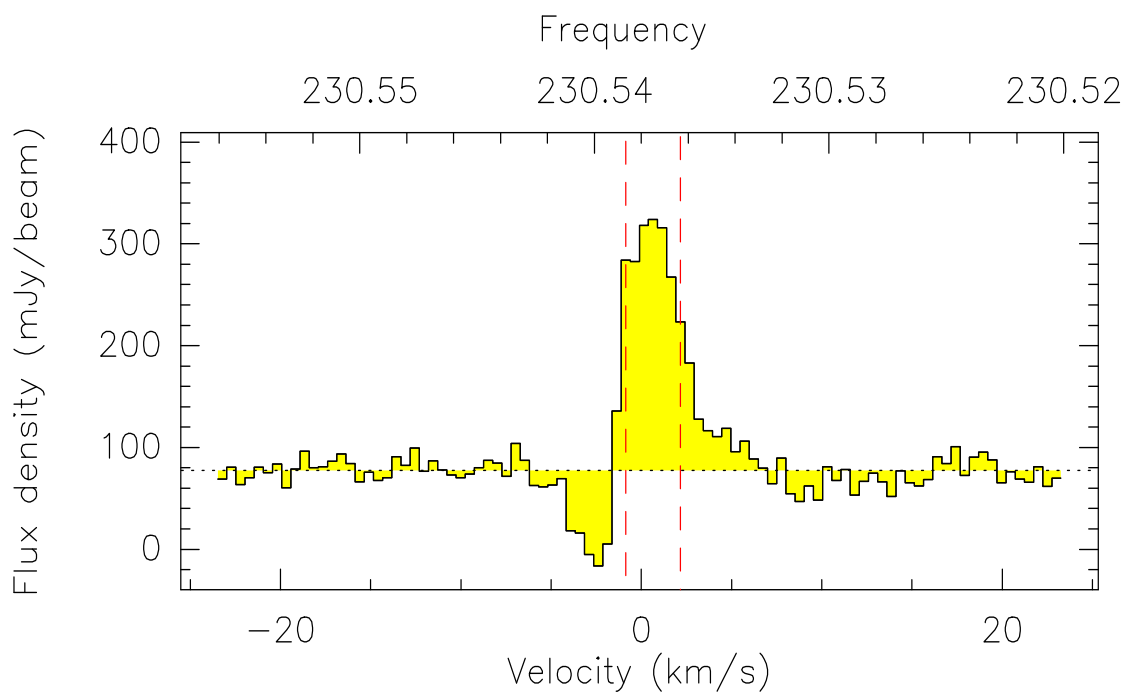


FIGURE 4.28: CO (2-1) line profile for V1331 Cyg taken from PdBI

4.18 SMA observations

The SMA data analysis was carried out by Dr. Stecklum. In order to compare SMA data with the Owens Valley Radio Observatory (OVRO) maps (refer to McMuldroy et al. [89]), the CO (2-1) emission channel map was made, by choosing SMA velocity closest to the OVRO value. The SMA continuum map is shown in Fig. 4.29. A contour spacing of 0.12 Jy/beam (corresponding to approx. 3 sigma) was applied. Compared to the OVRO maps, SMA map do not seem to show any ring like structure.

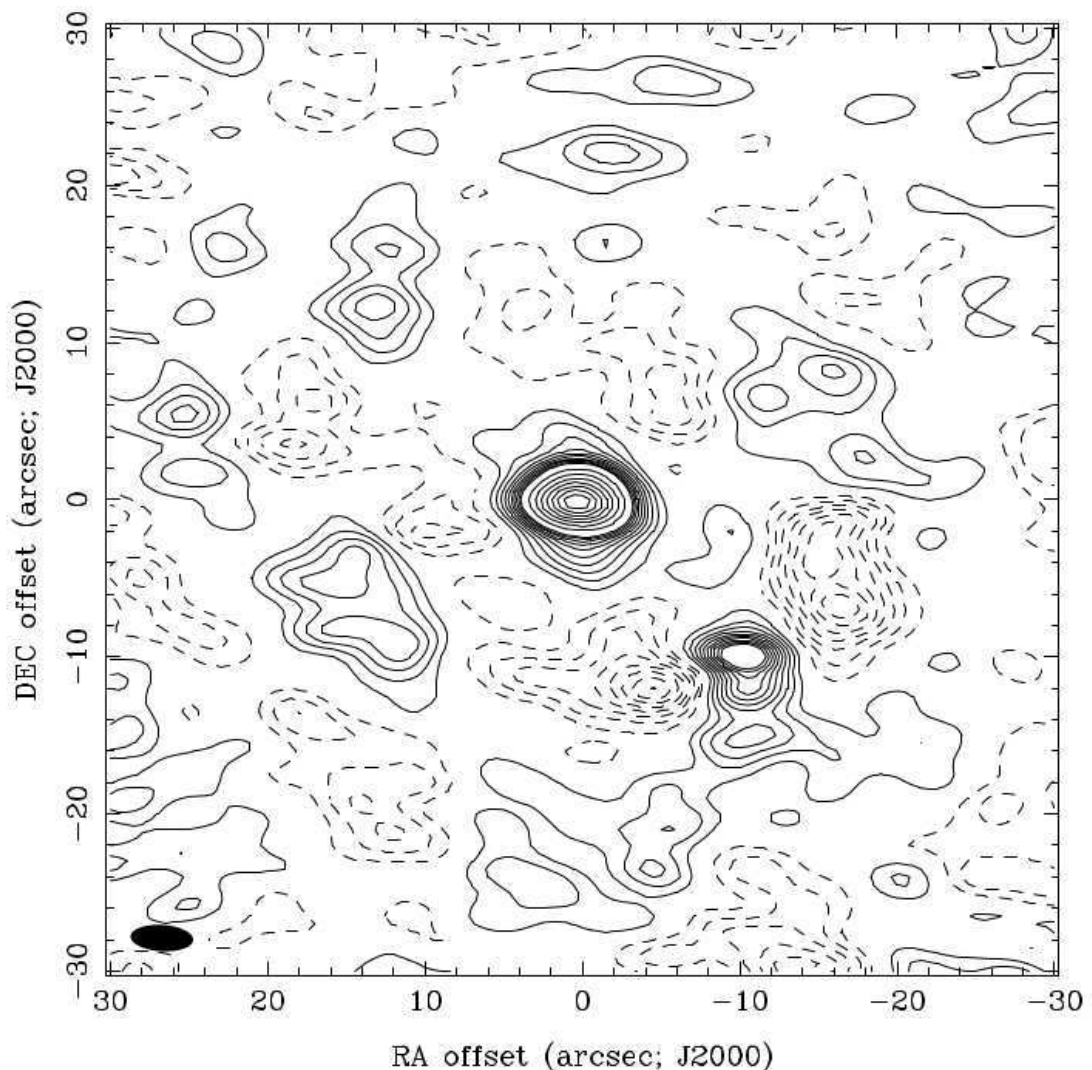


FIGURE 4.29: SMA integrated CO (2-1) continuum map. RA, DEC, VRAD = 21:01:09.207, +50:21:44.76, $-1.40000\text{E}+01$ km s⁻¹ at pixel (257.00, 257.00, 1.00). Spatial region: 197,197 to 317,317. Contour image: v1331cyg.co21.mom0 (V1331CYG) Min/max = -4.024/24.74 Contours x 0.5 JY/BEAM. KM/S. Contours: -50, -45, -40, -35, -30, -25, -20, -15, -10, -9, -8, -7, -6, -5, -4, -3, -2, -1, 1, 2, 3, 4, 5, 6, 7, 8, 9, 10, 15, 20, 25, 30, 35, 40, 45, 50

The only real looking source apart from the star itself, is the southwest ridge at the negative velocities. The difference between SMA and OVRO maps is probably due to different spatial frequencies sampled by the different interferometers and the distributed large scale structure.

Chapter 5

Results and Discussion

In the following, I draw conclusions based on the aforementioned results with particular emphasis on the radial expansion and particle separation hypotheses of the dust arcs. The possible physical processes going on and the mechanisms involved, in the stellar surroundings are discussed. The immediate neighbourhood of the star is described as well regarding its connection with the dark cloud and the bipolar outflow.

5.1 Origin and radial expansion of outer and inner arc

The dust arcs, both outer and inner, are found to be expanding. The outer one has a radial expansion velocity of $\approx 14.8 \pm 3.6 \text{ km s}^{-1}$, whereas, with more discrepancies involved, the inner arc is expanding with velocity between 0.8 km s^{-1} and 3.4 km s^{-1} . The calculation for inner arc is very uncertain because of its proximity to the central source, inducing more noise. Nevertheless, since a measurable expansion in both arcs has been traced, there has to be a mechanism driving it. In the following, I propose two possibilities, which could lead to the current expansion behaviour of the arcs.

5.1.1 Possibility one: Ambient cloud material

The young star V1331 Cyg evolved from within the dark cloud. As it is already known that during the process of star formation, the central source swipes up the infalling envelope mass and simultaneously, strong protostellar wind pushes away the surrounding cloud material. Similarly, in the case of V1331 Cyg, the central source created a pile-up of ambient cloud material at some distance and cleaned the surroundings. In the process, the dust arcs got the shape as we see today. Since the star is seen almost pole-on, the circular appearance of the possible remains of the blueshifted outflow cavity projected onto the sphere further support the explanation. The reason why similar circular structures are not seen among YSOs often is because the probability of seeing the YSO almost exactly pole-on is very low.

5.1.2 Possibility two: FUor outburst remnants

As already mentioned in the literature many times before, V1331 Cyg could actually be a FUor star that has undergone an eruption in the past. The ejected out material is now sitting in the stellar surroundings in a circular fashion. The arcs seen today are result of the material blown away during the outburst and moving away (expanding) from the star since then. During a FUor outburst, the mass accretion rate from the disk onto the star increases by orders of magnitude, disturbing the outflow collimation degree in the process (refer to Romanova et al. [133] for details). For a given magnetic field during the outburst phase, the collimation degree gets worse i.e. the outflow opening angle widens with increasing mass accretion rate. If the outflow jet is well collimated with small opening angle, the ejected out material will move further away from the source than if the outflow has a wider opening angle. In the latter case, the material will be located much closer to the star as is seen in the case of V1331 Cyg.

McMuldroch et al. [89] had modelled the dense CO gas as an inclined torus around V1331 Cyg, expanding with an overall velocity of $22 \pm 4 \text{ km s}^{-1}$, implying an implantation time of ≈ 4000 years at the current expansion rate. When I trace back the expansion velocity for the outer arc for an average distance of 9000 au, then the simple calculation suggests that the outer arc came into existence $\approx 2900_{-600}^{+900}$ years ago. Keeping the error margin in mind, outer arc implantation

time seems to be consistent with the estimates made by McMuldroch et al. [89]. Repeating the same calculation for an average distance of 3300 au for inner arc, the trace back time corresponds to $\approx 10000 \pm 5000$ years. The first impression suggests that the outer and inner arc trace back times are contradicting, since the outer arc though came into existence later, but overtook the inner arc in terms of expansion. However, this might be a result of assuming a linear expansion velocity which might not be the case, i.e. what if the velocity increases as the density decreases outward. Further analysis could be done to relate the tangential velocity derived from the dust arc expansion to the overall velocity of the CO ring, yielding the torus inclination. However, I would not do that because the velocities were derived for different distances from the star.

5.2 Reason behind outer arc brightness and colour behaviour

The outer dust arc around V1331 Cyg shows variations in brightness and colour as seen by the analysis done in Sections 4.6 & 4.10. Here again, I suggest two possibilities, both of which can explain the outer arc behaviour.

5.2.1 Spiral shaped outer arc

When considered over the azimuthal range, outer arc shows variations in both brightness and colour. If the arc were a full annulus, having an inclination (tilt) with respect to the plane of the sky, then depending upon the tilt angle, the scattered light as seen in the dust arc would have had varying distribution. Furthermore, if the dust arc is assumed to have an inclination $\theta \geq 30^\circ$, then one side of the arc facing the observer would brighten due to enhanced forward scattering, whereas, the side facing away would appear dimmer. Considering that only one grain size distribution exists, the colour and brightness behaviour across the azimuthal range hints at systematic changes in scattering angle throughout the arc. The analysis of re-scaled arc brightness from F814W image and [F814W-F450W] colour indeed supports the view. With this fact in mind, a better approximation to the outer arc structure could be that it has a three dimensional spiral shape instead. The north-eastern part of the arc is farther away in the foreground, bearing

blue colour resulting from a larger scattering angle. The arc spirals towards south over east, getting closer to the star and gets slightly redder since the scattering angle decreases. The southwest part of the outer arc does not have well defined inner boundary. This is the part of spiral going inwards, being a possible remnant of past inflow and causing the colour variation. Interestingly, at the top of this region (west of the star), inner knot like feature has been detected. Similar large scale in flowing spiral structures associated with protostars were recently detected with ALMA by Tokuda et al. [134].

5.2.2 Elliptical shaped torus

There is another possibility as well. Since the mutual location of the circumstellar disk of V1331 Cyg and the scattering grains is unknown, it is not ruled out that the dust resides in an elliptical torus which is offset and oblique with respect to the circumstellar disk plane. The azimuthal variation of the shadow size follows the same principle as for the dark cloud consideration. This configuration is supported by the model for the CO ring of McMurdock et al. [89] which is inclined by 30° to the plane of the sky. The ring which confines the outer arc is blueshifted to the east and the redshifted to the west of V1331 Cyg. If the dust is moving in the same fashion as the CO gas, it will be in the foreground of the star in the east while in the background to the west. The implied large range of the scattering angle might explain the overall brightness and colour variations. However, some regions remain problematic, e.g. the arc section to the north where there is a very steep colour decrease (see Figs. 4.9 (b), 4.12).

In summary, the circumstellar structure can be modelled in two ways. The CO torus is certainly favoured because the ejection times match, whereas, the other model suggests that the primordial inflow structure was possibly pushed away in the late YSO stage. In the latter case, the ejection times matching is by chance.

Complementary high-resolution imaging polarimetry will help to disentangle the 3D structure of the environment of V1331 Cyg by utilizing the dependence between polarisation degree and scattering angle as described in Fischer et al. [135].

5.3 Southwest ridge and possible elliptical arc extension

The southwest ridge located at a projected distance of ≈ 13000 au away from the star is not connected to the outer dust arc. As seen in Fig. 4.9 (b), the SW ridge appears to be quite blue at a uniform level. This hints that unrelated to the expanding outer arc, SW ridge sits in the foreground. Furthermore, the direct difference image (refer to Fig. 4.8) suggested that the ridge is moving towards V1331 Cyg.

The elliptical extension, as mentioned in Section 4.14 does not seem to have any bonding with the SW ridge. It rather is an independent structure probably formed during early collapse stages.

5.4 Missing ring section

The outer dust arc at a distance of ≈ 9000 au *and* if considered to be circular has some part of it not seen in the northwest direction (refer to Fig. 4.11). It was earlier suggested that a part of the outer arc is hidden behind LDN 981, as the dark cloud may sit in the foreground [92]. My recent study on the same (refer to Sections 4.9 & 4.11) will uncover the reasons possibly causing the missing ring section.

5.4.1 Role of dark cloud

With the proposition that the outer arc is a full circle indeed, the question arises what causes the missing section. It is tempting to assume that the dark cloud blocks the light. Since there is a gradient of the column density within the dark cloud toward its border, the width of the obscured section will depend on wavelength, simply because the dark cloud "looks slimmer" in the red than in the blue. This would cause a reddening at the edge zones of the missing section. Indeed, this has been found by the photometry of region 1 (see Fig. 4.11) as well as in the azimuthal profile (see Fig. 4.12) at position angles of $\approx 250^\circ$ *and* $\approx 340^\circ$. On the other hand, the extinction analysis of the UKIDSS images showed that the cloud

runs behind the star. Both findings can only be kept without contradiction if the dark cloud is in the foreground of V1331 Cyg in the west and runs behind the YSO towards east. But then, in order to obscure the stellar environment, it has to come close to the star. This, however, implies that the dark cloud would scatter stellar light as well, and appear in reflection. The deep TLS image (see Fig. 4.20) shows some scattering in the I band which could originate from the stellar illumination of the dark cloud. Yet, its weak surface brightness indicates that the LDN 981 cannot be very close to the star.

5.4.2 Inner knot discovered

Another viable explanation is shadowing. As mentioned earlier, if the dust has an elliptical torus shape, which is offset and oblique with respect to the circumstellar disk plane, then the disk could cast a shadow onto the torus which appears as missing section. Shadowing might also occur due to height variations in the circumstellar disk when the scattering dust locally exceeds the normal extent. For YSOs seen close to edge-on this causes photometric changes known as UX Ori variability, e.g. Herbst et al. [136]. Indeed, my analysis of the first epoch planetary camera frames indicate the presence of a feature (Fig. 4.24 (b)) very close to the star at the right position angle which is connected to the inner bright arc found by Kitamura et al. [94]. It might be a scale height enhancement in the outer circumstellar disk which stretches over some azimuthal range. However, its orbital time scale is way too large to observe changes in PA of the shadow over the epoch difference of HST observations. Moreover, shadowing will also lead to a lower dust temperature and, thus, reduced thermal dust emission, which is along the lines of the PACS observations. Given the observational evidence, I consider shadowing as a likely explanation for the missing arc section.

The PdBI continuum map (Fig. 4.27) of the thermal dust emission also hints on presence of a prominent feature at the knot position. Although the hint is marginal but it nevertheless supports the view of the knot being a real feature. The knot photometry does not indicate on the presence a stellar companion, the colour value rather suggests that the knot results from dust scattering.

5.5 Bipolar outflow and HH objects

The bipolar outflow from V1331 Cyg has been known in literature since the work of Levreault [86]. Another detailed study conducted by Mundt and Eislöffel [90] considered the possibility that the HHOs to the north-west (D, E, and F in their nomenclature) could be part of another flow since they depart from a straight flow geometry. In my study, I found a nearby flow from an embedded YSO on Spitzer-IRAC images which, however, is not crossing that of V1331 Cyg. The detection of an even more western HHO (J) (see Fig. 4.20 (a)) confirms that all the patchy northern HHOs belong to the blueshifted flow. The updated extent of the bipolar outflow due to pole-on inclination could be 10 parsec or even more. In general, the outflow sizes have been found in the range from less than 0.1 pc to about 5 pc [18]. In comparison to those, V1331 Cyg could have given rise to one of the most extended bipolar outflows.

The speckled morphology of the shock-excited emission in optical lines as well as molecular hydrogen does not resemble bow shocks at all. According to the models of Gustafsson et al. [137], it suggests a near to head-on view onto the outflow, in agreement with existing evidence for the face-on view of the star.

5.6 V1331 Cyg SED

The synthetic SED generated using online radiative transfer fitter was just a very basic model or the starting point to make better fits than now. In the present fit (see Fig. 4.23) from the Robitaille's grid [131], all 22 physical parameters (see Appendix Table C.2) for a YSO model are considered free and the fit is generated by simultaneously varying all of those. However, it is well known that SED fits are prone to ambiguity, the disagreement with other independent studies e.g. [99] for V1331 Cyg makes it possible to compare those values to provide a range of uncertainty. So for further SED analysis, the parameter space can be decided by shrinking the range of acceptable values for various parameters based on the Robitaille's grid fitting results compared with results from Petrov et al. [99].

The development of a sophisticated radiative transfer model for V1331 Cyg was beyond the scope of my PhD work. But, a more reliable SED fitting method would be to put constraints on most of the parameters and vary only the minimum

required to obtain a better fit. This approach can be followed using MC3D code [138, 139], where there is a flexibility to choose a few free parameters and fix the rest. The fitted SED and output parameters for the model obtained using MC3D would be more acceptable.

Chapter 6

Conclusions and future work suggestions

6.1 Conclusions

HST-WFPC2 images proper motion analysis for the target YSO V1331 Cyg, with an epoch difference of almost ten years yielded an average expansion velocity of $\approx 14.8 \pm 3.6 \text{ km s}^{-1}$ for the outer arc and between 0.8 and 3.4 km s^{-1} for the inner dust arc. The trace back time for the outer arc turns out to be consistent with CO torus implantation time, supporting the view that V1331 Cyg did undergo an outburst a few thousand years ago.

The overall brightness and colour variation analysis for the outer arc indicates that it results from azimuthal variation in scattering angle. Possible dust configuration could be a tilted misaligned torus that is confined by the CO ring of McMudroch et al. [89] or a spiral that could be an accretion flow relic which tightens and winds down to the outer circumstellar disk. While I could not confirm the particle separation hypothesis based on the colour analysis of outer dust arc, evidence for a larger fraction of smaller ISM grains at distances exceeding 15000 au was found. The SW ridge has a different (very uniformly blue) colour profile altogether. Sitting in the foreground, it is moving toward the central YSO. Unrelated to it, the newly found elliptical arc is possibly surrounding circumstellar material pushed away and shaped during early stages of star formation.

Dark cloud plays no role in causing the missing ring section. The absence of light from that part in the northwest is caused by shadowing from the knot like feature very closely placed to the star. This knot is certainly not a binary stellar companion as it is caused by starlight scattered from the dust. Since the star is seen almost pole-on, the length of HH flow could be as large as 10 pc or even more. My attempt to model the SED of V1331 Cyg yielded results which are not consistent with previous works. Thus, the SED alone does not allow to unambiguously characterise the YSO and its circumstellar dust distribution, but independent measurements, e.g. of stellar quantities and/or the spatial extent of the emission, are required as well.

6.2 Outlook to the future

The variable young star V1331 Cyg holds immense riddles to be solved still. Using high resolution NOEMA and SMA data, future prospects would be to constrain the mass and kinematics of the disk features of V1331 Cyg and to reveal the circumstances of possible planet or brown dwarf formation hosted by V1331 Cyg.

MC3D continuum radiative transfer code would be used to look into the SED model fitting for V1331 Cyg and thereby getting better understanding of the star. In addition, the code results would be used to simulate the immediate surroundings of the star in terms of grain size distribution, light scattering and circumstellar disk structure.

Appendix A

Additional content

A.1 P Cygni profile

The stellar spectrum provides information on the star in the first place, normally by absorption lines arising in the photosphere and emission lines in case of activity. Foreground matter imprints by absorption lines as well. It also tells whether the outflow is in the form of an expanding shell of gas or it takes the form of a powerful stellar wind.

P Cygni profile was named after the prototype **P Cygni** also known as 34 Cygni, which is a highly luminous and variable Be star at about 7,000 light-years away from us. Figure [A.1](#) shows the classic P Cygni line profile. It consists of strong emission lines accompanied by less intense absorption lines, displaced to the blue side of the emission lines. As seen in the figure, blueshifted absorption is produced by material moving away from the star and towards us, whereas, the emission contribution comes from parts of the expanding shell. The brightness bursts are thought to be due to the star throwing off shells of gas.

A P Cygni profile in which the emission lines lie on the blue side of the absorption component is called as **inverse P Cygni profile**. It is usually interpreted as signature of an infall of matter.

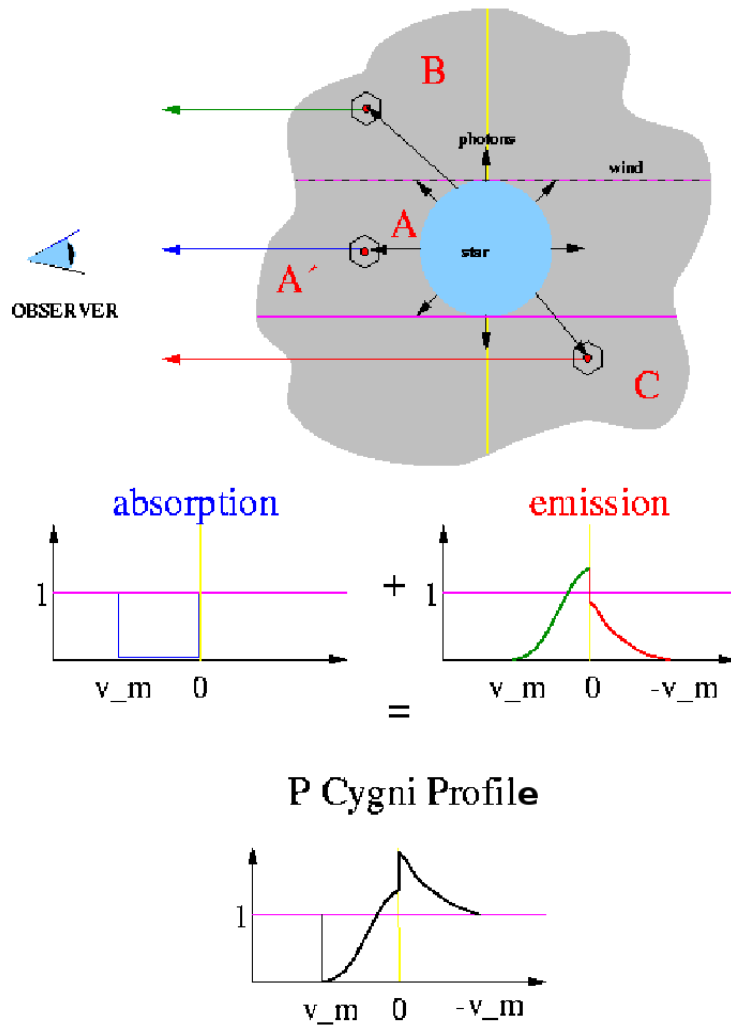


FIGURE A.1: Sketch showing the formation of P Cygni profile. Image adapted from R.P. Kudritzki.

Appendix B

IDL scripts

B.1 WF3 Camera background correction script

```
-----  
file='606.fits'  
ima=readfits('cc'+file,h)  
sub=ima[0:767,0:747] ; lower left quadrant (almost)  
idx=where(sub eq 0) ; keep zero (NAN) pixel  
a=median(ima[768:768+20,0:747],dimen=1)  
b=median(ima[767-20:767,0:747],dimen=1)  
plot,a-b  
diff=a-b  
; make it smooth  
hhh=robust_poly_fit(findgen(748),diff,4,sdiff)  
oplot,sdiff,col=196  
; use tweaking factor according to best visual appearance  
sub=temporary(sub)+replicate(1,768)#sdiff*0.75  
; restore zeroes  
sub[idx]=0  
; replace quadrant  
ima[0:767,0:747]=sub  
writefits,'cc1'+file,ima,h  
end  
-----
```

B.2 Script to calculate transformation parameters using SVD algorithm

```
;-----  
; read data  
read_asc, 'v1331xy.txt', ncol=4, hhh  
; treat them as double precision images  
xy1=double(reform(hhh[0:1,*]))  
xy2=double(reform(hhh[2:3,*]))  
; number of unknown parameters  
np=4  
; start parameters  
coef=[-100.,250.,0.5,1.]  
; required relative accuracy  
accuracy = 1e-6  
; define arrays  
s=size(xy1)  
sizx=s[1]  
sizy=s[2]  
; partial derivatives  
pder=fltarr(sizx,sizy,np)  
xar=findgen(sizx)#replicate(1.,sizy) ; array of x values  
yar=replicate(1.,sizx)#findgen(sizy) ; same for y  
; right-hand side vector  
r=dblarr(np)  
; coefficient matrix  
act=r#r  
; start Chisq, required to get loop going  
chisq=1d11  
; iteration counter  
count = 0  
; initialize model coordinates  
xy=xy1  
; main loop  
repeat begin  
chi_old = chisq
```

```

; fitting function
xy[0,*]=coef[3]*((xy1[0,*]-coef[0])*cos(coef[2])-(xy1[1,*]-coef[1])*&
sin(coef[2]))
xy[1,*]=coef[3]*((xy1[0,*]-coef[0])*sin(coef[2])+(xy1[1,*]-coef[1])*&
cos(coef[2]))
; difference
dxy=xy2-xy
; normalized Chisq
chisq=total(dxy*dxy)/float(sizx)/float(sizy)
print,chisq
; compute the partial derivatives
pder[0,*,0]=-coef[3]*cos(coef[2])
pder[1,*,0]=-coef[3]*sin(coef[2])
pder[0,*,1]=coef[3]*sin(coef[2])
pder[1,*,1]=-coef[3]*cos(coef[2])
pder[0,*,2]=coef[3]*((xy1[0,*]-coef[0])*(-sin(coef[2]))-(xy1[1,*]-coef[1])*&
cos(coef[2]))
pder[1,*,2]=coef[3]*((xy1[0,*]-coef[0])*cos(coef[2])+(xy1[1,*]-coef[1])*&
(-sin(coef[2])))
pder[*,*,3]=xy/coef[3]
; setup right-hand side vector and coefficient matrix
for k=0,np-1 do begin
r[k]=total((dxy)* pder[*,*,k])
for l=0,np-1 do begin
act[l,k]=double(total(pder[*,*,k]*pder[*,*,l]))
endfor
endfor
; SVD decomposition
svdc,act,w,u,v,/double
; check condition
idx=where(w lt 1e-6,wcount)
; eliminate SV if bad
if wcount NE 0 then w[idx]=0
; solve for coefficient differential
; IDL intrinsic
; dcoef=svsol(u,w,v,r,/double)

```

```
; straight way of getting the solution from the decomposition
ww=dblarr(np,np)
ww[[findgen(np)],[findgen(np)]]=1/w
dcoef=v ## ww## transpose(u) ## r
; and add
coef=coef+dcoef*0.5
; increase counter
count = count + 1
; check if precision or iteration limit reached
endrep until abs(chisq - chi_old)/abs(chisq) lt accuracy or count ge 60
if count ge 60 then $
message,'No convergence after 60 iterations - result is inconclusive!'/inform
; compute the errors
; errcoef=svsol(u,w,v,replicate(double(1.),np))
ww[[findgen(np)],[findgen(np)]]=1/w
errcoef=v ## ww ## transpose(u) ## replicate(double(1.),np)
errcoef=sqrt(abs(chisq*errcoef))
; print the results
print,format='("X-shift +/- error :",f9.4," ",f8.4)',coef[0],errcoef[0]
print,format='("Y-shift +/- error :",f9.4," ",f8.4)',coef[1],errcoef[1]
print,format='("Rotation [rad] +/- error:",f9.5," ",f8.5)',coef[2],errcoef[2]
print,format='("Stretch factor +/- error:",f9.5," ",f8.5)',coef[3],errcoef[3]
; done
end
;-----
```


B.3 Script to remap second epoch image to match first epoch

```
-----  
image=readfits('2ndf606w.fits',h) ; read image  
; - - determine array size and center of the array  
imsize=size(image)  
nx=imsize[1]  
ny=imsize[2]  
xmax=800  
; - - All distance units are in pixel units.  
if(keyword_set(missing)) then begin  
fmiss=missing  
endif else begin  
fmiss=0.  
endelse  
; - - get sizes and ranges of radius (r) and angle (theta) arrays  
nr=double(xmax)  
x1=dindgen(nr)#replicate(1,800)  
y1=transpose(x1)  
if(imsize[0] ne 2) then begin  
print,"fxy not a 2D array"  
return  
endif  
; - - it's up to the user to make sure that the origin  
; is within your original- - cartesian mesh!  
x2=1.000031*((x1+135.7042)*cos(0.51735)-(y1-235.3908)*sin(0.51735))  
y2=1.000031*((x1+135.7042)*sin(0.51735)+(y1-235.3908)*cos(0.51735))  
remapped_image=interpolate(image,x2,y2,missing=0)  
; Since this is astronomical data, output it to fits,  
; and have a look with IDL  
Writefits,'remap_2nd.FITS',remapped_image  
end  
-----
```

B.4 Script to calculate expansion in dust arcs between two epochs

```

;-----
; read dust arcs
read_asc,'1st606.txt',hhh
read_asc,'2nd606.txt',ggg
; oversampling factor
nsamp=100
; test case: fractional shift
tshift=1./10
; number of iterations
nit=500
o=double(reform(ggg[1,0:*)>0))
; cut outer part
o[60:n_elements(o)-1]=0
;o=o/total(o)
ro=rebin(o,nsamp*n_elements(o))
; create fake "image"
roo=[[ro],[ro]]
r=double(reform(hhh[1,0:*)>0))
; cut outer part
r[60:n_elements(r)-1]=0
;r=r/total(r)
rr=rebin(r,nsamp*n_elements(r))
rrr=[[rr],[rr]]
; point spread profile
p=rrr/total(rrr)
window,xsize=800,ysize=600
psf_ft=0&doo=0 ; 2nd profile
for i=0,nit-1 do begin&max_likelihood,roo,p,doo,ft_psf=psf_ft&
end&plot,doo[*,0]/max(doo),col=128,xrange=nsamp*[165,175],yrange=[0,1.1]
; 1st profile self
drrr=0
for i=0,nit-1 do begin&max_likelihood,rrr,p,drrr,ft_psf=psf_ft&end&
oplot,drrr[*,0]/max(drrr)

```

```
; this is the reference index
dum=max(drrr[:,0],idx)
refidx=idx
; 1st profile shifted
drrs=0
for i=0,nit-1 do begin&max_likelihood,fshift(rrr,[nsamp*tshift,0],/nocubic)&
,p,drrs,ft_psf=psf_ft&end&oplot,drrs[:,0]/max(drrs),col=196
print,"Second epoch dust profile deconvolved : ",max(droo[:,0],idx),idx
print,"First epoch dust profile deconvolved : ",max(drrr[:,0],idx),idx
print,"First epoch SHIFTED dust deconvolved : ",max(drrs[:,0],idx),idx
;stop
; Monte-Carlo part, check if shift is due to small profile
; deviations. Create smooth 2nd epoch profile
; by convolving solution with point spread profile
syn=convolve(p,droo)
plot,syn[:,0]
oplot,roo[:,0],col=128
; residuals
oplot,roo[:,0]-syn[:,0],col=196
; residuals
res=roo[:,0]-syn[:,0]
; omit values which are close to zero
idx=where(abs(res) ge 5e-6)
; std. deviation
stdd=stddev(res[idx])
; here the Monte-Carlo loop starts
; number of iterations
nmc=10000
; store shifts
smc=fltarr(nmc)
print,"Differences in shift due to noise to the original shift"
for j=0,nmc-1 do begin
; draw the noise - this is not strict yet!
;white (flat) noise seems to be more
;appropriate than Gaussian, therefore the tweak factor of 3.5!
noise=(randomu(seed,n_elements(idx))-.5)*stdd*3.5
```

```
; plot,noise
; add noise and do analysis
roo=syn
roo[idx,*]=roo[idx,*]+[[noise],[noise]]
droo=0
for i=0,nit-1 do max_likelihood,roo,p,droo,ft_psf=psf_ft
dummy=max(droo[*],0),mcidx
smc[j]=mcidx-refidx
print,smc[j]
end
print,mean(smc),stddev(smc)
end
;-----
```

Appendix C

V1331 Cyg SED

TABLE C.1: Listing of all the flux values used to generate the SED fit for V1331 Cyg. a=The TYCHO Input Catalogue - Cross-matching the Guide Star Catalog with the HIPPARCOS INCA Data Base [140]; b=The Naval Observatory Merged Astrometric Dataset (NOMAD) [141]; c=TASS Mark IV Photometric Survey of the Northern Sky [142]; d=WISE All-Sky Data Release (Cutri+ 2012) [143]; e=The first INTEGRAL-OMC catalogue of optically variable sources [120]; f=Long-Term Evolution of FU Ori-Type Stars at Infrared Wavelengths [144]; g=An Analysis of the Environments of FU Orionis Objects with Herschel [97]; h=Photometry done by Dr. Stecklum on UKIDSS JHK images; j=Spitzer-IRS spectrum from Program ID:20363, AORKEY:14549760, measured by CASIS webtool; k=The SCUBA Legacy Catalogues: Submillimeter-Continuum Objects Detected by SCUBA [145]; l= Millimeter interferometric observations of FU Orionis-type objects in Cygnus [96]; m=Guide Star Catalog II [<http://tdc-www.harvard.edu/catalogs/gsc2.html>]

Filter	$\lambda(\mu\text{m})$	Flux(Jy)	References
Bessel B	0.44	0.03 ± 0.01	m
Bessel B	0.44	0.06 ± 0.03	a
Bessel V	0.55	0.06 ± 0.04	e
Bessel V	0.55	0.07 ± 0.04	a
Bessel V	0.55	0.06 ± 0.03	c
Bessel R	0.63	0.16 ± 0.11	b
Bessel I	0.90	0.12 ± 0.10	c
2MASS J	1.2	0.18 ± 0.02	b

Continued on next page

Table C.1 – continued from previous page

Filter	$\lambda(\mu\text{m})$	Flux (Jy)	References
UKIDSS J	1.2	0.18 ± 0.02	h
2MASS H	1.6	0.19 ± 0.01	b
UKIDSS H	1.6	0.22 ± 0.02	h
2MASS K	2.1	0.25 ± 0.02	b
UKIDSS K	2.15	0.26 ± 0.02	h
WISE	3.4	0.36 ± 0.01	d
WISE	4.6	0.53 ± 0.02	d
Spitzer-IRS	5.97	0.59 ± 0.01	j
Spitzer-IRS	7.65	0.68 ± 0.01	j
MSX A	8.3	0.78 ± 0.03	f
Spitzer-IRS	9	0.81 ± 0.03	j
Spitzer-IRS	10.48	1.05 ± 0.02	j
WISE	12	0.74 ± 0.01	d
MSX D	14.7	1.2 ± 0.09	f
Spitzer-IRS	14.83	1.11 ± 0.01	j
Spitzer-IRS	18	1.72 ± 0.06	j
MSX E	21.3	2.23 ± 0.16	f
WISE	22	2.15 ± 0.02	d
Spitzer-IRS	25.58	2.52 ± 0.08	j
Spitzer-IRS	28.04	2.64 ± 0.01	j
Spitzer-IRS	33.26	3.38 ± 0.10	j
Spitzer-IRS	37.69	4.21 ± 0.12	j
PACS	70	7.77 ± 0.03	g
PACS	100	10.14 ± 0.07	g
PACS	160	11.72 ± 0.19	g
SPIRE	250	9.9 ± 1.1	g
SPIRE	350	6.4 ± 1.0	g
SCUBA	450	5.22 ± 1.74	k
SPIRE	500	2.7 ± 0.6	g
SCUBA	850	0.59 ± 0.03	k
PdBI	2700	0.012 ± 0.002	l

TABLE C.2: The table lists the stellar parameters constrained by our best fit SED model compared with the Gramajo et al. [132] results.

Stellar parameter	Our model value	Gramajo's model	Petrov fit
Stellar age (yr)	$1.22e + 5$		$9.961e + 05$
Stellar mass (M_{\odot})	1.65	0.8	3.171
Stellar radius (R_{\odot})	9.05	2.0	5.268
Stellar temperature (K)	4292	5770	5069
Envelope accretion rate ($M_{\odot}.\text{yr}^{-1}$)	$4.64e - 6$	$0.8e - 06$	$1.830e - 08$
Envelope outer radius (AU)	$1.43e + 4$	8000	3049
Envelope cavity angle (degrees)	34.0	50	32.17
Envelope inner radius (R_{sub})	1.00		7.774
Disk mass (M_{\odot})	$4.04e - 2$	0.02	$8.038e - 02$
Disk outer radius (AU)	$6.48e + 1$	100	83.8
Disk inner radius (R_{sub})	1.00		7.774
Disk inner radius (AU)	$3.64e - 1$	$1.76e - 03$	2.2
Disk scaleheight factor	0.852		$9.698e - 01$
Disk flaring power	1.175		1.161
Disk accretion alpha	$5.97e - 2$		$2.300e - 03$
Envelope cavity density (cgs)	$6.66e - 21$	$1.5e - 20$	$2.017e - 21$
Ambient density (cgs)	$6.35e - 22$	$4.2e - 22$	$1.583e - 21$
Disk accretion rate ($M_{\odot}.\text{yr}^{-1}$)	$1.07e - 6$	$0.1e - 06$	$6.068e - 08$
A_v [circumstellar] (mag)	0.342		$2.209e - 02$
Total luminosity (L_{\odot})	30.2		17.37
Disk scaleheight at 100 AU	8.38		5.965
Envelope mass (M_{\odot})	0.370	0.120	$3.441e - 04$

Bibliography

- [1] J. M. Scalo. The stellar initial mass function. *Fundamentals of Cosmic Physics*, 11:1–278, May 1986.
- [2] R. B. Larson. The physics of star formation. *Reports on Progress in Physics*, 66:1651–1697, October 2003. doi: 10.1088/0034-4885/66/10/R03.
- [3] J. Bally, J. Morse, and B. Reipurth. The Birth of Stars: Herbig-Haro Jets, Accretion and Proto-Planetary Disks. In P. Benvenuti, F. D. Macchetto, and E. J. Schreier, editors, *Science with the Hubble Space Telescope - II*, page 491, 1996.
- [4] C. Hayashi. Evolution of Protostars. *Annual Review of Astronomy & Astrophysics*, 4:171, 1966. doi: 10.1146/annurev.aa.04.090166.001131.
- [5] J. H. Jeans. The Stability of a Spherical Nebula. *Royal Society of London Philosophical Transactions Series A*, 199:1–53, 1902. doi: 10.1098/rsta.1902.0012.
- [6] L. Spitzer. *Physical processes in the interstellar medium*. 1978.
- [7] S. Basu and T. C. Mouschovias. Magnetic braking, ambipolar diffusion, and the formation of cloud cores and protostars. 1: Axisymmetric solutions. *The Astrophysical Journal*, 432:720–741, September 1994. doi: 10.1086/174611.
- [8] M. N. Machida, K. Tomisaka, and T. Matsumoto. First MHD simulation of collapse and fragmentation of magnetized molecular cloud cores. *Monthly Notices of the Royal Astronomical Society*, 348:L1–L5, February 2004. doi: 10.1111/j.1365-2966.2004.07402.x.
- [9] R. B. Larson. Angular momentum and the formation of stars and black holes. *Reports on Progress in Physics*, 73(1):014901, January 2010. doi: 10.1088/0034-4885/73/1/014901.

-
- [10] S. Basu and T. C. Mouschovias. Magnetic Braking, Ambipolar Diffusion, and the Formation of Cloud Cores and Protostars. III. Effect of the Initial Mass-to-Flux Ratio. *The Astrophysical Journal*, 453:271, November 1995. doi: 10.1086/176387.
- [11] S. Basu and T. C. Mouschovias. Magnetic Braking, Ambipolar Diffusion, and the Formation of Cloud Cores and Protostars. II. A Parameter Study. *The Astrophysical Journal*, 452:386, October 1995. doi: 10.1086/176310.
- [12] N. Ohashi, M. Hayashi, P. T. P. Ho, M. Momose, M. Tamura, N. Hirano, and A. I. Sargent. Rotation in the Protostellar Envelopes around IRAS 04169+2702 and IRAS 04365+2535: The Size Scale for Dynamical Collapse. *The Astrophysical Journal*, 488:317–329, October 1997.
- [13] N. Ohashi. Interferometric Imagings of Protostellar and Pre-Protostellar Envelopes. In T. Nakamoto, editor, *Star Formation 1999*, pages 129–135, December 1999.
- [14] S. Terebey, F. H. Shu, and P. Cassen. The collapse of the cores of slowly rotating isothermal clouds. *The Astrophysical Journal*, 286:529–551, November 1984. doi: 10.1086/162628.
- [15] C. J. Lada. Star formation - From OB associations to protostars. In M. Peimbert and J. Jugaku, editors, *Star Forming Regions*, volume 115 of *IAU Symposium*, pages 1–17, 1987.
- [16] S. Terebey, C. J. Chandler, and P. Andre. The contribution of disks and envelopes to the millimeter continuum emission from very young low-mass stars. *The Astrophysical Journal*, 414:759–772, September 1993. doi: 10.1086/173121.
- [17] P. Andre, D. Ward-Thompson, and M. Barsony. Submillimeter continuum observations of Rho Ophiuchi A - The candidate protostar VLA 1623 and prestellar clumps. *The Astrophysical Journal*, 406:122–141, March 1993. doi: 10.1086/172425.
- [18] R. Bachiller. Bipolar Molecular Outflows from Young Stars and Protostars. *Annual Review of Astronomy & Astrophysics*, 34:111–154, 1996. doi: 10.1146/annurev.astro.34.1.111.

- [19] C. J. Lada. Star Formation in the Galaxy: An Observational Overview. *Progress of Theoretical Physics Supplement*, 158:1–23, 2005. doi: 10.1143/PTPS.158.1.
- [20] S. W. Stahler and F. Palla. *The Formation of Stars*. Wiley-VCH, 2005.
- [21] A. H. Joy. T Tauri Variable Stars. *The Astrophysical Journal*, 102:168, September 1945. doi: 10.1086/144749.
- [22] V. A. Ambartsumian. Stellar evolution and astrophysics. *Ac. Sci. Armenian SSR, Yerevan*, 1947.
- [23] W. Herbst and R. M. Levrault. TiO photometry of six T Tauri stars. *The Astronomical Journal*, 100:1951–1956, December 1990. doi: 10.1086/115650.
- [24] D. Kilkenny, D. C. B. Whittet, J. K. Davies, A. Evans, M. F. Bode, E. I. Robson, and R. M. Banfield. Optical and infrared photometry of southern early-type shell stars and pre-main-sequence variables. *South African Astronomical Observatory Circular*, 9:55–86, 1985.
- [25] G. H. Herbig. The properties and problems of T Tauri stars and related objects. *Advances in Astronomy and Astrophysics*, 1:47–103, 1962.
- [26] G. H. Herbig. The Spectrum of the Nebulosity Surrounding T Tauri. *The Astrophysical Journal*, 111:11, January 1950. doi: 10.1086/145232.
- [27] T. Nakajima and D. A. Golimowski. Coronagraphic imaging of pre-main-sequence stars: Remnant envelopes of star formation seen in reflection. *The Astronomical Journal*, 109:1181–1198, March 1995. doi: 10.1086/117351.
- [28] K. R. Stapelfeldt, C. J. Burrows, J. E. Krist, A. M. Watson, G. E. Ballester, J. T. Clarke, D. Crisp, R. W. Evans, J. S. Gallagher, III, R. E. Griffiths, J. J. Hester, J. G. Hoessel, J. A. Holtzman, J. R. Mould, P. A. Scowen, J. T. Trauger, and J. A. Westphal. Hubble Space Telescope Imaging of the Circumstellar Nebulosity of T Tauri. *The Astrophysical Journal*, 508:736–743, December 1998. doi: 10.1086/306422.
- [29] W. Herbst, J. F. Booth, P. F. Chugainov, G. V. Zajtseva, W. Barksdale, E. Covino, L. Terranegra, A. Vittone, and F. Vrba. The rotation period and inclination angle of T Tauri. *The Astrophysical Journal, Letters*, 310:L71–L75, November 1986. doi: 10.1086/184784.

- [30] G. Duchêne and A. Kraus. Stellar Multiplicity. *Annual Review of Astronomy & Astrophysics*, 51:269–310, August 2013. doi: 10.1146/annurev-astro-081710-102602.
- [31] P. Ghosh and F. K. Lamb. Accretion by rotating magnetic neutron stars. II - Radial and vertical structure of the transition zone in disk accretion. *The Astrophysical Journal*, 232:259–276, August 1979. doi: 10.1086/157285.
- [32] L. Hartmann. *Accretion Processes in Star Formation*. Cambridge University Press, June 1998.
- [33] J. B. Pollack, D. Hollenbach, S. Beckwith, D. P. Simonelli, T. Roush, and W. Fong. Composition and radiative properties of grains in molecular clouds and accretion disks. *The Astrophysical Journal*, 421:615–639, February 1994. doi: 10.1086/173677.
- [34] C. P. Dullemond, D. Hollenbach, I. Kamp, and P. D’Alessio. Models of the Structure and Evolution of Protoplanetary Disks. *Protostars and Planets V*, pages 555–572, 2007.
- [35] D. Lynden-Bell and J. E. Pringle. The evolution of viscous discs and the origin of the nebular variables. *Monthly Notices of the Royal Astronomical Society*, 168:603–637, September 1974.
- [36] R. L. Snell, R. B. Loren, and R. L. Plambeck. Observations of CO in L1551 - Evidence for stellar wind driven shocks. *The Astrophysical Journal, Letters*, 239:L17–L22, July 1980. doi: 10.1086/183283.
- [37] C. J. Lada. Cold outflows, energetic winds, and enigmatic jets around young stellar objects. *Annual Review of Astronomy & Astrophysics*, 23:267–317, 1985. doi: 10.1146/annurev.aa.23.090185.001411.
- [38] J. Kwan and N. Scoville. The nature of the broad molecular line emission at the Kleinmann-Low nebula. *The Astrophysical Journal, Letters*, 210:L39–L43, November 1976. doi: 10.1086/182298.
- [39] B. Zuckerman, T. B. H. Kuiper, and E. N. Rodriguez Kuiper. High-velocity gas in the Orion infrared nebula. *The Astrophysical Journal, Letters*, 209:L137–L142, November 1976. doi: 10.1086/182284.
- [40] G. H. Herbig. The Spectra of Two Nebulous Objects Near NGC 1999. *The Astrophysical Journal*, 113:697–699, May 1951. doi: 10.1086/145440.

- [41] G. Haro. Herbig's Nebulous Objects Near NGC 1999. *The Astrophysical Journal*, 115:572, May 1952. doi: 10.1086/145576.
- [42] G. Haro. H α Emission Stars and Peculiar Objects in the Orion Nebula. *The Astrophysical Journal*, 117:73, January 1953. doi: 10.1086/145669.
- [43] J. P. Ostriker and C. F. McKee. Astrophysical blastwaves. *Reviews of Modern Physics*, 60:1–68, 1988. doi: 10.1103/RevModPhys.60.1.
- [44] R. A. Chevalier and J. C. Raymond. Optical emission from a fast shock wave - The remnants of Tycho's supernova and SN 1006. *The Astrophysical Journal, Letters*, 225:L27–L30, October 1978. doi: 10.1086/182785.
- [45] S. Heathcote, J. A. Morse, P. Hartigan, B. Reipurth, R. D. Schwartz, J. Bally, and J. M. Stone. Hubble Space Telescope Observations of the HH 47 Jet: Narrowband Images. *The Astronomical Journal*, 112:1141, September 1996. doi: 10.1086/118085.
- [46] L. Hartmann and S. J. Kenyon. The FU Orionis Phenomenon. *Annual Review of Astronomy & Astrophysics*, 34:207–240, 1996. doi: 10.1146/annurev.astro.34.1.207.
- [47] A. A. Wachmann. Spektral-Durchmusterung von Milchstrassenfeldern. In *Spektral-Durchmusterung von Milchstrassenfeldern. Teil 1 , 1 (1939)*, page 0, 1939.
- [48] A. Wachmann. Das bisherige Verhalten von FU Orionis. Mit 7 Textabbildungen. *Zeitschrift für Astrophysik*, 35:74, 1954.
- [49] G. H. Herbig. On the interpretation of FU orionis. *Vistas in Astronomy*, 8: 109–125, 1966. doi: 10.1016/0083-6656(66)90025-0.
- [50] G. H. Herbig. Eruptive phenomena in early stellar evolution. *The Astrophysical Journal*, 217:693–715, November 1977. doi: 10.1086/155615.
- [51] K. M. Strom and S. E. Strom. The discovery of two FU Orionis objects in L1641. *The Astrophysical Journal, Letters*, 412:L63–L66, August 1993. doi: 10.1086/186941.
- [52] B. Reipurth and C. Aspin. Infrared Spectroscopy of Herbig-Haro Energy Sources. *The Astronomical Journal*, 114:2700, December 1997. doi: 10.1086/118680.

- [53] J. H. Elias. A study of the IC 5146 dark cloud complex. *The Astrophysical Journal*, 223:859–861, August 1978. doi: 10.1086/156319.
- [54] B. Reipurth, C. Aspin, T. Beck, C. Brogan, M. S. Connelley, and G. H. Herbig. V733 Cep (Persson’s Star): A New FU Orionis Object in Cepheus. *The Astronomical Journal*, 133:1000–1011, March 2007. doi: 10.1086/510617.
- [55] J. A. Graham and J. A. Frogel. An FU Orionis star associated with Herbig-Haro object 57. *The Astrophysical Journal*, 289:331–341, February 1985. doi: 10.1086/162893.
- [56] T. A. Movsessian, T. Khanzadyan, C. Aspin, T. Y. Magakian, T. Beck, A. Moiseev, M. D. Smith, and E. H. Nikogossian. An outbursting protostar of the fu orionis type in the cygnus ob7 molecular cloud. *Astronomy & Astrophysics*, 455:1001–1008, September 2006.
- [57] B. Reipurth and C. Aspin. IRAS 05436-0007 and the Emergence of MCNeil’s Nebula. *The Astrophysical Journal, Letters*, 606:L119–L122, May 2004. doi: 10.1086/421393.
- [58] U. Bastian and R. Mundt. FU Orionis star winds. *Astronomy & Astrophysics*, 144:57–63, March 1985.
- [59] K. Croswell, L. Hartmann, and E. H. Avrett. Mass loss from FU Orionis objects. *The Astrophysical Journal*, 312:227–242, January 1987. doi: 10.1086/164865.
- [60] N. Calvet, L. Hartmann, and S. J. Kenyon. Mass loss from pre-main-sequence accretion disks. I - The accelerating wind of FU Orionis. *The Astrophysical Journal*, 402:623–634, January 1993. doi: 10.1086/172164.
- [61] S. Edwards, T. Ray, and R. Mundt. Energetic mass outflows from young stars. In E. H. Levy and J. I. Lunine, editors, *Protostars and Planets III*, pages 567–602, 1993.
- [62] P. Hartigan, S. Edwards, and L. Ghandour. Disk Accretion and Mass Loss from Young Stars. *The Astrophysical Journal*, 452:736, October 1995. doi: 10.1086/176344.
- [63] L. Mayer, T. Quinn, J. Wadsley, and J. Stadel. Formation of Giant Planets by Fragmentation of Protoplanetary Disks. *Science*, 298:1756–1759, November 2002. doi: 10.1126/science.1077635.

- [64] J. B. Pollack, O. Hubickyj, P. Bodenheimer, J. J. Lissauer, M. Podolak, and Y. Greenzweig. Formation of the Giant Planets by Concurrent Accretion of Solids and Gas. *ICAR, ELSEVIER*, 124:62–85, November 1996. doi: 10.1006/icar.1996.0190.
- [65] H. Beust, A.-M. Lagrange, I. A. Crawford, C. Goudard, J. Spyromilio, and A. Vidal-Madjar. The beta Pictoris circumstellar disk. XXV. The Ca Ii absorption lines and the Falling Evaporating Bodies model revisited using UHRF observations. *Astronomy & Astrophysics*, 338:1015–1030, October 1998.
- [66] A. V. Krivov. Debris disks: seeing dust, thinking of planetesimals and planets. *Research in Astronomy and Astrophysics*, 10:383–414, May 2010. doi: 10.1088/1674-4527/10/5/001.
- [67] M. C. Wyatt. Evolution of Debris Disks. *Annual Review of Astronomy & Astrophysics*, 46:339–383, September 2008. doi: 10.1146/annurev.astro.45.051806.110525.
- [68] B. T. Draine. Scattering by Interstellar Dust Grains. I. Optical and Ultraviolet. *The Astrophysical Journal*, 598:1017–1025, December 2003. doi: 10.1086/379118.
- [69] E. Krügel. *An introduction to the physics of interstellar dust*. 2008.
- [70] R. D. Mountain. Spectral Distribution of Scattered Light in a Simple Fluid. *Reviews of Modern Physics*, 38:205–214, January 1966. doi: 10.1103/RevModPhys.38.205.
- [71] W. L. Peticolas. Inelastic Light Scattering and the Raman Effect. *Annual Review of Physical Chemistry*, 23:93–116, October 1972. doi: 10.1146/annurev.pc.23.100172.000521.
- [72] R. J. Trumpler. Absorption of Light in the Galactic System. *Publications of the Astronomical Society of the Pacific*, 42:214, August 1930. doi: 10.1086/124039.
- [73] K. Serkowski. Interstellar Polarization (review). In J. M. Greenberg and H. C. van de Hulst, editors, *Interstellar Dust and Related Topics*, volume 52 of *IAU Symposium*, page 145, 1973.

- [74] R. H. Hildebrand, J. L. Dotson, C. D. Dowell, D. A. Schleuning, and J. E. Vaillancourt. The Far-Infrared Polarization Spectrum: First Results and Analysis. *The Astrophysical Journal*, 516:834–842, May 1999. doi: 10.1086/307142.
- [75] M. Wenger, F. Ochsenbein, D. Egret, P. Dubois, F. Bonnarel, S. Borde, F. Genova, G. Jasniewicz, S. Laloë, S. Lesteven, and R. Monier. The SIMBAD astronomical database. The CDS reference database for astronomical objects. *Astronomy & Astrophysics, Supplement*, 143:9–22, April 2000. doi: 10.1051/aas:2000332.
- [76] G. González and G. González. Stars with H α emission in Galactic Longitudes 59° to 90° (Spanish Title: Estrellas con H α en emision en las longitudes galacticas de 59° a 90°). *Boletin de los Observatorios Tonantzintla y Tacubaya*, 2:16–26, December 1956.
- [77] L. V. Kuhi. Mass Loss from T Tauri Stars. *The Astrophysical Journal*, 140:1409, November 1964. doi: 10.1086/148047.
- [78] E. E. Mendoza V. Infrared Photometry of T Tauri Stars and Related Objects. *The Astrophysical Journal*, 143:1010, March 1966. doi: 10.1086/148584.
- [79] E. E. Mendoza V. Infrared Excesses in T Tauri Stars and Related Objects. *The Astrophysical Journal*, 151:977, March 1968. doi: 10.1086/149497.
- [80] G. V. Zaitseva. On the variation of brightness LkHA 120. *Astronomicheskij Tsirkulyar*, 475:7–8, 1968.
- [81] G. Welin. Possible properties of pre-outburst FU Orionis stars. *Astronomy & Astrophysics*, 49:145–148, May 1976.
- [82] M. V. Penston and P. M. Keavey. The spectrum of the T Tauri star LK H-alpha 120. *Monthly Notices of the Royal Astronomical Society*, 180:407–413, August 1977.
- [83] C. Chavarria. A study of the peculiar T Tauri star V 1331 Cygni. *Astronomy & Astrophysics*, 101:105–117, August 1981.
- [84] E. A. Kolotilov. Photoelectric UBV Photometry of the Peculiar T-Tauri Star V1331-CYGNI. *Soviet Astronomy Letters*, 9:289–291, June 1983.

- [85] R. Schulte-Ladbeck. Linear polarization variations of six T Tauri stars. *Astronomy & Astrophysics*, 120:203–214, April 1983.
- [86] R. M. Levreault. Molecular outflows and mass loss in the pre-main-sequence stars. *The Astrophysical Journal*, 330:897–910, July 1988. doi: 10.1086/166520.
- [87] V. Shevchenko, S. D. Yakubov, V. V. Ambaryan, and A. T. Garibdzhanyan. A Compact Star-Forming Region Associated with V1331-CYGNI. *Soviet Astronomy*, 35:135, April 1991.
- [88] X.-W. Cao and J.-L. Zhang. The Raman spectrum of the T Tauri star LkH α 120. *Chinese Astronomy & Astrophysics*, 16:315–318, September 1992. doi: 10.1016/0275-1062(92)90072-J.
- [89] S. McMudroch, A. I. Sargent, and G. A. Blake. The circumstellar environment of the FU Orionis pre-outburst candidate V1331 Cygni. *The Astronomical Journal*, 106:2477–2485, December 1993. doi: 10.1086/116815.
- [90] R. Mundt and J. Eislöffel. T Tauri Stars Associated with Herbig-Haro Objects and Jets. *The Astronomical Journal*, 116:860–867, August 1998. doi: 10.1086/300461.
- [91] A. S. Hojaev. A study of the young star V1331 Cyg in a compact star forming region. *New Astronomy Reviews*, 43:431–435, 1999. doi: 10.1016/S1387-6473(99)00030-5.
- [92] S. P. Quanz, D. Apai, and T. Henning. Dust Rings and Filaments around the Isolated Young Star V1331 Cygni. *The Astrophysical Journal*, 656:287–292, February 2007. doi: 10.1086/510376.
- [93] J. R. Najita, G. W. Doppmann, J. S. Carr, J. R. Graham, and J. A. Eisner. High-Resolution K-Band Spectroscopy of MWC 480 and V1331 Cyg. *The Astrophysical Journal*, 691:738–748, January 2009. doi: 10.1088/0004-637X/691/1/738.
- [94] M. Kitamura, T. Yamada, M. Tamura, and T. Kudo. Direct Imaging of the Pre-outburst FU Ori Candidate V1331 Cyg. In T. Usuda, M. Tamura, and M. Ishii, editors, *American Institute of Physics Conference Series*, volume 1158 of *American Institute of Physics Conference Series*, pages 135–136, August 2009. doi: 10.1063/1.3215819.

- [95] G. W. Doppmann, J. R. Najita, J. S. Carr, and J. R. Graham. Warm H₂O and OH Disk Emission in V1331 Cyg. *The Astrophysical Journal*, 738:112, September 2011. doi: 10.1088/0004-637X/738/1/112.
- [96] Á. Kóspál. Millimeter interferometric observations of FU Orionis-type objects in Cygnus. *Astronomy & Astrophysics*, 535:A125, November 2011. doi: 10.1051/0004-6361/201117966.
- [97] J. D. Green, N. J. Evans, II, Á. Kóspál, G. Herczeg, S. P. Quanz, T. Henning, T. A. van Kempen, J.-E. Lee, M. M. Dunham, G. Meeus, J. Bouwman, J.-h. Chen, M. Güdel, S. L. Skinner, A. Liebhart, and M. Merello. An Analysis of the Environments of FU Orionis Objects with Herschel. *The Astrophysical Journal*, 772:117, August 2013. doi: 10.1088/0004-637X/772/2/117.
- [98] P. P. Petrov and E. V. Babina. The photospheric spectrum of the pre-FUor V1331 CYG: Is it a star or a disk? *Bulletin Crimean Astrophysical Observatory*, 110:1–8, June 2014. doi: 10.3103/S0190271714010203.
- [99] P. P. Petrov, R. Kurosawa, M. M. Romanova, J. F. Gameiro, M. Fernandez, E. V. Babina, and S. A. Artemenko. Facing the wind of the pre-FUor V1331 Cyg. *Monthly Notices of the Royal Astronomical Society*, 442:3643–3652, August 2014. doi: 10.1093/mnras/stu1131.
- [100] I. Heyer and J. Biretta. Wide field and planetary camera 2 instrument handbook for cycle 14. *Version 9.0, Baltimore: STScI*, pages 1–21, 2004.
- [101] A. Lawrence, S. J. Warren, O. Almaini, A. C. Edge, N. C. Hambly, R. F. Jameson, P. Lucas, M. Casali, A. Adamson, S. Dye, J. P. Emerson, S. Foucaud, P. Hewett, P. Hirst, S. T. Hodgkin, M. J. Irwin, N. Lodieu, R. G. McMahon, C. Simpson, I. Smail, D. Mortlock, and M. Folger. The UKIRT Infrared Deep Sky Survey (UKIDSS). *Monthly Notices of the Royal Astronomical Society*, 379:1599–1617, August 2007. doi: 10.1111/j.1365-2966.2007.12040.x.
- [102] M. Casali, A. Adamson, C. Alves de Oliveira, O. Almaini, K. Burch, T. Chuter, J. Elliot, M. Folger, S. Foucaud, N. Hambly, M. Hastie, D. Henry, P. Hirst, M. Irwin, D. Ives, A. Lawrence, K. Laidlaw, D. Lee, J. Lewis, D. Lunney, S. McLay, D. Montgomery, A. Pickup, M. Read, N. Rees, I. Robson, K. Sekiguchi, A. Vick, S. Warren, and B. Woodward. The UKIRT

- wide-field camera. *Astronomy & Astrophysics*, 467:777–784, May 2007. doi: 10.1051/0004-6361:20066514.
- [103] P. C. Hewett, S. J. Warren, S. K. Leggett, and S. T. Hodgkin. The UKIRT Infrared Deep Sky Survey ZY JHK photometric system: passbands and synthetic colours. *Monthly Notices of the Royal Astronomical Society*, 367: 454–468, April 2006. doi: 10.1111/j.1365-2966.2005.09969.x.
- [104] S. T. Hodgkin, M. J. Irwin, P. C. Hewett, and S. J. Warren. The UKIRT wide field camera ZYJHK photometric system: calibration from 2MASS. *Monthly Notices of the Royal Astronomical Society*, 394:675–692, April 2009. doi: 10.1111/j.1365-2966.2008.14387.x.
- [105] N. C. Hambly, R. S. Collins, N. J. G. Cross, R. G. Mann, M. A. Read, E. T. W. Sutorius, I. Bond, J. Bryant, J. P. Emerson, A. Lawrence, L. Rimoldini, J. M. Stewart, P. M. Williams, A. Adamson, P. Hirst, S. Dye, and S. J. Warren. The WFCAM Science Archive. *Monthly Notices of the Royal Astronomical Society*, 384:637–662, February 2008. doi: 10.1111/j.1365-2966.2007.12700.x.
- [106] D. Lang, D. W. Hogg, K. Mierle, M. Blanton, and S. Roweis. Astrometry.net: Blind Astrometric Calibration of Arbitrary Astronomical Images. *The Astronomical Journal*, 139:1782–1800, May 2010. doi: 10.1088/0004-6256/139/5/1782.
- [107] G. G. Fazio, J. L. Hora, L. E. Allen, M. L. N. Ashby, P. Barmby, L. K. Deutsch, J.-S. Huang, S. Kleiner, M. Marengo, S. T. Megeath, G. J. Melnick, M. A. Pahre, B. M. Patten, J. Polizotti, H. A. Smith, R. S. Taylor, Z. Wang, S. P. Willner, W. F. Hoffmann, J. L. Pipher, W. J. Forrest, C. W. McMurty, C. R. McCreight, M. E. McKelvey, R. E. McMurray, D. G. Koch, S. H. Moseley, R. G. Arendt, J. E. Mentzell, C. T. Marx, P. Losch, P. Mayman, W. Eichhorn, D. Krebs, M. Jhabvala, D. Y. Gezari, D. J. Fixsen, J. Flores, K. Shakoorzadeh, R. Jungo, C. Hakun, L. Workman, G. Karpati, R. Kichak, R. Whitley, S. Mann, E. V. Tollestrup, P. Eisenhardt, D. Stern, V. Gorjian, B. Bhattacharya, S. Carey, B. O. Nelson, W. J. Glaccum, M. Lacy, P. J. Lowrance, S. Laine, W. T. Reach, J. A. Stauffer, J. A. Surace, G. Wilson, E. L. Wright, A. Hoffman, G. Domingo, and M. Cohen. The Infrared Array Camera (IRAC) for the Spitzer Space Telescope. *The Astrophysical Journal, Supplement*, 154:10–17, September 2004. doi: 10.1086/422843.

- [108] K. Murakawa, H. Suto, M. Tamura, N. Kaifu, H. Takami, N. Takato, S. Oya, Y. Hayano, W. Gaessler, and Y. Kamata. CIAO: Coronagraphic Imager with Adaptive Optics on the Subaru Telescope. *Publications of the Astronomical Society of Japan*, 56:509–519, June 2004. doi: 10.1093/pasj/56.3.509.
- [109] H. Baba, N. Yasuda, S.-I. Ichikawa, M. Yagi, N. Iwamoto, T. Takata, T. Horaguchi, M. Taga, M. Watanabe, T. Ozawa, and M. Hamabe. Development of the Subaru-Mitaka-Okayama-Kiso Archive System. In D. A. Bohlender, D. Durand, and T. H. Handley, editors, *Astronomical Data Analysis Software and Systems XI*, volume 281 of *Astronomical Society of the Pacific Conference Series*, page 298, 2002.
- [110] G. L. Pilbratt, J. R. Riedinger, T. Passvogel, G. Crone, D. Doyle, U. Gageur, A. M. Heras, C. Jewell, L. Metcalfe, S. Ott, and M. Schmidt. Herschel Space Observatory. An ESA facility for far-infrared and submillimetre astronomy. *Astronomy & Astrophysics*, 518:L1, July 2010. doi: 10.1051/0004-6361/201014759.
- [111] A. Poglitsch, C. Waelkens, N. Geis, H. Feuchtgruber, B. Vandenbussche, L. Rodriguez, O. Krause, E. Renotte, C. van Hoof, P. Saraceno, J. Cepa, F. Kerschbaum, P. Agnèsè, B. Ali, B. Altieri, P. Andreani, J.-L. Augueres, Z. Balog, L. Barl, O. H. Bauer, N. Belbachir, M. Benedettini, N. Billot, O. Boulade, H. Bischof, J. Blommaert, E. Callut, C. Cara, R. Cerulli, D. Cesarsky, A. Contursi, Y. Creten, W. De Meester, V. Doublier, E. Doumayrou, L. Duband, K. Exter, R. Genzel, J.-M. Gillis, U. Grözinger, T. Henning, J. Herreros, R. Huygen, M. Inguscio, G. Jakob, C. Jamar, C. Jean, J. de Jong, R. Katterloher, C. Kiss, U. Klaas, D. Lemke, D. Lutz, S. Madden, B. Marquet, J. Martignac, A. Mazy, P. Merken, F. Montfort, L. Morbidelli, T. Müller, M. Nielbock, K. Okumura, R. Orfei, R. Ottensamer, S. Pezzuto, P. Popesso, J. Putzeys, S. Regibo, V. Reveret, P. Royer, M. Sauvage, J. Schreiber, J. Stegmaier, D. Schmitt, J. Schubert, E. Sturm, M. Thiel, G. Tofani, R. Vavrek, M. Wetzstein, E. Wieprecht, and E. Wiezorrek. The Photodetector Array Camera and Spectrometer (PACS) on the Herschel Space Observatory. *Astronomy & Astrophysics*, 518:L2, July 2010. doi: 10.1051/0004-6361/201014535.
- [112] M. Sánchez-Portal, A. Marston, B. Altieri, H. Aussel, H. Feuchtgruber, U. Klaas, H. Linz, D. Lutz, B. Merín, T. Müller, M. Nielbock, M. Oort,

- G. Pilbratt, M. Schmidt, C. Stephenson, and M. Tuttlebee. The pointing system of the Herschel space observatory. Description, Calibration, Performance and improvements. *Experimental Astronomy*, 37:453–479, July 2014. doi: 10.1007/s10686-014-9396-z.
- [113] A. S. Fruchter and R. N. Hook. Drizzle: A Method for the Linear Reconstruction of Undersampled Images. *The Publications of the Astronomical Society of the Pacific*, 114:144–152, February 2002. doi: 10.1086/338393.
- [114] J. M. Winters and R. Neri. An introduction to the iram plateau de bure interferometer. *Institut de Radio Astronomie Millimetrique*, 4.2, June 2011.
- [115] P. T. P. Ho, J. M. Moran, and K. Y. Lo. The Submillimeter Array. *The Astrophysical Journal, Letters*, 616:L1–L6, November 2004. doi: 10.1086/423245.
- [116] Lisa A Wells and David J Bell. Cleaning images of bad pixels and cosmic rays using iraf. *IRAF document*, 1994.
- [117] J. E. Krist, R. N. Hook, and F. Stoehr. 20 years of Hubble Space Telescope optical modeling using Tiny Tim. In *Society of Photo-Optical Instrumentation Engineers (SPIE) Conference Series*, volume 8127 of *Society of Photo-Optical Instrumentation Engineers (SPIE) Conference Series*, page 0, October 2011. doi: 10.1117/12.892762.
- [118] F. Ochsenbein, P. Bauer, and J. Marcout. The VizieR database of astronomical catalogues. *Astronomy & Astrophysics, Supplement*, 143:23–32, April 2000. doi: 10.1051/aas:2000169.
- [119] M. J. D. Powell. An efficient method for finding the minimum of a function of several variables without calculating derivatives. *The Computer Journal*, 7(2):155–162, 1964. doi: 10.1093/comjnl/7.2.155. URL <http://comjnl.oxfordjournals.org/content/7/2/155.abstract>.
- [120] J. Alfonso-Garzón, A. Domingo, J. M. Mas-Hesse, and A. Giménez. The first INTEGRAL-OMC catalogue of optically variable sources. *Astronomy & Astrophysics*, 548:A79, December 2012. doi: 10.1051/0004-6361/201220095.
- [121] M. J. Cottrell and A. N. Witt. The surface brightness of reflection nebulae - NGC 1432 and the 17 Tauri nebulosity. *The Astronomical Journal*, 88: 418–426, March 1983. doi: 10.1086/113326.

- [122] E. Bertin and S. Arnouts. SExtractor: Software for source extraction. *Astronomy & Astrophysics, Supplement*, 117:393–404, June 1996.
- [123] M. B. Taylor. TOPCAT & STIL: Starlink Table/VOTable Processing Software. In P. Shopbell, M. Britton, and R. Ebert, editors, *Astronomical Data Analysis Software and Systems XIV*, volume 347 of *Astronomical Society of the Pacific Conference Series*, page 29, December 2005.
- [124] M. R. Meyer, N. Calvet, and L. A. Hillenbrand. Intrinsic Near-Infrared Excesses of T Tauri Stars: Understanding the Classical T Tauri Star Locus. *The Astronomical Journal*, 114:288–300, July 1997. doi: 10.1086/118474.
- [125] J. Koornneef. Near-infrared photometry. II - Intrinsic colours and the absolute calibration from one to five micron. *Astronomy & Astrophysics*, 128: 84–93, November 1983.
- [126] R. Indebetouw, J. S. Mathis, B. L. Babler, M. R. Meade, C. Watson, B. A. Whitney, M. J. Wolff, M. G. Wolfire, M. Cohen, T. M. Bania, R. A. Benjamin, D. P. Clemens, J. M. Dickey, J. M. Jackson, H. A. Kobulnicky, A. P. Marston, E. P. Mercer, J. R. Stauffer, S. R. Stolovy, and E. Churchwell. The Wavelength Dependence of Interstellar Extinction from 1.25 to 8.0 μm Using GLIMPSE Data. *The Astrophysical Journal*, 619:931–938, February 2005. doi: 10.1086/426679.
- [127] E. Pantin and J.-L. Starck. Deconvolution of astronomical images using the multiscale maximum entropy method. *Astronomy & Astrophysics, Supplement*, 118:575–585, September 1996.
- [128] J. B. Foster and A. A. Goodman. Cloudshine: New Light on Dark Clouds. *The Astrophysical Journal, Letters*, 636:L105–L108, January 2006. doi: 10.1086/500131.
- [129] G. Sandell and D. A. Weintraub. On the Similarity of FU Orionis Stars to Class I Protostars: Evidence from the Submillimeter. *The Astrophysical Journal, Supplement*, 134:115–132, May 2001. doi: 10.1086/320360.
- [130] T. L. Hayward, J. R. Houck, and J. W. Miles. Thermal infrared imaging of subarcsecond structure in the trapezium nebula. *The Astrophysical Journal*, 433:157–163, September 1994. doi: 10.1086/174632.

- [131] T. P. Robitaille, B. A. Whitney, R. Indebetouw, and K. Wood. Interpreting Spectral Energy Distributions from Young Stellar Objects. II. Fitting Observed SEDs Using a Large Grid of Precomputed Models. *The Astrophysical Journal, Supplement*, 169:328–352, April 2007. doi: 10.1086/512039.
- [132] L. V. Gramajo, J. A. Rodón, and M. Gómez. SED analysis of class I and class II FU Orionis stars. *ArXiv e-prints*, February 2014.
- [133] M. M. Romanova, G. V. Ustyugova, A. V. Koldoba, and R. V. E. Lovelace. Launching of conical winds and axial jets from the disc-magnetosphere boundary: axisymmetric and 3D simulations. *Monthly Notices of the Royal Astronomical Society*, 399:1802–1828, November 2009. doi: 10.1111/j.1365-2966.2009.15413.x.
- [134] K. Tokuda, T. Onishi, K. Saigo, A. Kawamura, Y. Fukui, T. Matsumoto, S.-i. Inutsuka, M. N. Machida, K. Tomida, and K. Tachihara. ALMA Observations of a High-density Core in Taurus: Dynamical Gas Interaction at the Possible Site of a Multiple Star Formation. *The Astrophysical Journal, Letters*, 789:L4, July 2014. doi: 10.1088/2041-8205/789/1/L4.
- [135] O. Fischer, T. Henning, and H. W. Yorke. Simulation of polarization maps. 1: Protostellar envelopes. *Astronomy & Astrophysics*, 284:187–209, April 1994.
- [136] W. Herbst, D. K. Herbst, E. J. Grossman, and D. Weinstein. Catalogue of UBVRI photometry of T Tauri stars and analysis of the causes of their variability. *The Astronomical Journal*, 108:1906–1923, November 1994. doi: 10.1086/117204.
- [137] M. Gustafsson, T. Ravkilde, L. E. Kristensen, S. Cabrit, D. Field, and G. Pineau Des Forêts. 3D model of bow shocks. *Astronomy & Astrophysics*, 513:A5, April 2010. doi: 10.1051/0004-6361/200912977.
- [138] S. Wolf. MC3D-3D continuum radiative transfer, Version 2. *Computer Physics Communications*, 150:99–115, February 2003. doi: 10.1016/S0010-4655(02)00675-6.
- [139] S. Wolf, T. Henning, and B. Stecklum. Multidimensional self-consistent radiative transfer simulations based on the Monte-Carlo method. *Astronomy & Astrophysics*, 349:839–850, September 1999.

- [140] D. Egret, P. Didelon, B. J. McLean, J. L. Russell, and C. Turon. The TYCHO Input Catalogue - Cross-matching the Guide Star Catalog with the HIPPARCOS INCA Data Base. *Astronomy & Astrophysics*, 258:217–222, May 1992.
- [141] N. Zacharias, D. G. Monet, S. E. Levine, S. E. Urban, R. Gaume, and G. L. Wycoff. The Naval Observatory Merged Astrometric Dataset (NOMAD). In *American Astronomical Society Meeting Abstracts*, volume 36 of *Bulletin of the American Astronomical Society*, page 1418, December 2004.
- [142] T. F. Droege, M. W. Richmond, M. P. Sallman, and R. P. Creager. TASS Mark IV Photometric Survey of the Northern Sky. *Publications of the Astronomical Society of the Pacific*, 118:1666–1678, December 2006. doi: 10.1086/510197.
- [143] R. M. Cutri and et al. VizieR Online Data Catalog: WISE All-Sky Data Release (Cutri+ 2012). *VizieR Online Data Catalog*, 2311:0, 2012.
- [144] Á. Kóspál, P. Ábrahám, M. Kun, S. Csizmadia, and E. Verdugo. Long-Term Evolution of FU Ori-Type Stars at Infrared Wavelengths. *Astrophysics & Space Science*, 292:547–551, August 2004. doi: 10.1023/B:ASTR.0000045061.12172.a7.
- [145] J. Di Francesco, D. Johnstone, H. Kirk, T. MacKenzie, and E. Ledwosinska. The SCUBA Legacy Catalogues: Submillimeter-Continuum Objects Detected by SCUBA. *The Astrophysical Journal, Supplement*, 175:277–295, March 2008. doi: 10.1086/523645.

Curriculum Vitae

Name: Arpita Choudhary

Date of birth: 02 -10 -1986

Nationality: Indian

Email address: arpita@tls-tautenburg.de, arp.astro@gmail.com

Phone: +49-36427-863-64, +49-17626-2942-15

Year 2011 - 2015: PhD student at Friedrich Schiller University, Jena
& Thüringer Landessternwarte Tautenburg, Germany

Year 2012: Master thesis at
Friedrich Schiller University, Jena, Germany
in Black hole acoustic horizon geometry

Year 2010 - 2011: Post MSc research project at
Harish Chandra Research Institute, Allahabad, India
in Black hole Astrophysics

Year 2008 - 2010: Master of Science with 78% marks from
University of Lucknow, India
in Physics

Year 2005 - 2008: Bachelor of Science with 71% marks from
University of Lucknow, India
in Astronomy, Physics and Maths

Year 2005: Intermediate with 87% marks from
Navayuga Radiance Senior Secondary School
Lucknow, India

Year 2003: High school with 86% marks from
Navayuga Radiance Senior Secondary School
Lucknow, India

Year 1989 to 2003: Primary school education from
Navayuga Radiance Senior Secondary School
Lucknow, India

Jena, 21 September 2015

List of publications and talks

Publications

- V1331 Cyg- An outburst of results, by **Choudhary, Arpita**; Stecklum, Bringfried; Stapelfeldt, Karl; Linz, Hendrik (to be submitted).
- V1331 Cyg- An outburst of results, by **Choudhary, Arpita**; Stecklum, Bringfried; Stapelfeldt, Karl in Protostars and Planets VI, Heidelberg, July 15-20, 2013. Poster #2B063.
- The role of axisymmetric flow configuration in the estimation of the analogue surface gravity and related Hawking like temperature, by Bilić, Neven; **Choudhary, Arpita**; Das, Tapas K.; Nag, Sankhasubhra in Classical and Quantum Gravity, Volume 31, Issue 3, article id. 035002 (2014), February, 2014.

Talks

- V1331 Cyg, Hubble observations and more at IMSC, India in July, 2015.
- An update on V1331 Cyg proper motion analysis of dust arcs and other data at NASA GSFC, USA in August, 2014.
- Overview of V1331 Cyg Hubble data analysis and more at Thüringer Landessternwarte Tautenburg, Germany in October, 2013.